Microscale engineering of active systems

Microscale engineering of active systems: exploiting dynamicity to induce motility

PROEFSCHRIFT

ter verkrijging van de graad van doctor aan de Technische Universiteit Eindhoven, op gezag van de rector magnificus prof.dr.ir. F.P.T. Baaijens, voor een commissie aangewezen door het College voor Promoties, in het openbaar te verdedigen op vrijdag 1 april 2022 om 11:00 uur

door

Shidong Song

geboren te Jilin, China

Dit proefschrift is goedgekeurd door de promotoren en de samenstelling van de promotiecommissie is als volgt:

voorzitter:	prof. dr. R.P. Sijbesma
1e promotor:	prof. dr. ir. J.C.M. van Hest
copromotor(en):	dr. L.K.E.A. Abdelmohsen
leden:	prof. dr. E.W. Meijer
	prof. dr. ir. T.F.A. de Greef
	dr. D.J. Kraft (Universiteit Leiden)
Adviseur:	dr. J. Meijer
	prof. dr. S. Sanchez Ordónez (Institute for Bioengineering of Catalonia)

Het onderzoek of ontwerp dat in dit proefschrift wordt beschreven is uitgevoerd in overeenstemming met de TU/e Gedragscode Wetenschapsbeoefening.

Dedicated to my family

Microscale engineering of active systems: exploiting dynamicity to induce motility

Shidong Song

This research was funded by the ERC Advanced Grant (Artisym 694120).

A catalogue record is available from the Eindhoven University of Technology Library.

ISBN: 978-90-386-5485-0

Cover design: Shidong Song

Printed by ADC Nederland

Contents

CHAPTER 1

Motility strategies of cell-mimicking soft compartments

Abstract

Cells, sophisticated membrane-bound units that contain the fundamental molecules of life, provide 'a precious library' for inspiration and motivation for scientists from various disciplines. This inspiration has been the basis of the emerging field of artificial cell research. Herein, scientists both try to provide fundamental answers how life evolved and to create systems with life-like features. Great endeavours have been made towards the engineering of artificial counterparts that integrate structural or functional cellular elements. The first step from prebiotic soup to a living cell has been proposed to be compartmentalization as it is vital to provide a clear distinction between the inner cellular environment and the outside world. Furthermore, living systems are generally out-of-equilibrium and equipped with dissipative biological processes that require constant supplies of energy and building blocks. Natural cells fulfil such request by metabolism, a set of life-sustaining chemical reactions. The integration of chemical reactions which generate energy in the artificial cell platform paves the way to more advanced and complex functionalities, such as responsiveness to environmental cues and motility. In this chapter, we highlight recent developments toward mimicry of cellular motility utilizing soft compartments. We will subsequently discuss compartmentalization, biological reactions for energy production and, in the end, motility.

This chapter is adapted from the publication: Wang, L.*; Song, S.*; van Hest, J.; Abdelmohsen, L. K. E. A.; Huang, X.; Sánchez, S., Biomimicry of Cellular Motility and Communication Based on Synthetic Soft-Architectures. *Small* **2020,** *16* (27), 1907680.

*These authors contributed equally.

1.1 Introduction

Natural cells are considered as the basis of biological complexity. As such, they have long been the inspiration for scientists to create systems that mimic life. The field of synthetic biology tries to gain insights about prebiotic forms of early life, especially towards understanding the structure, function and their evolutionary process.[1] Although it is impossible to know how exactly life emerged, creating synthetic cells with life-like features is a first step in the direction to understand the prerequisites that would have enabled complex molecular systems to evolve into a living entity. For this purpose, a bottom-up approach that aims to construct a fully functional synthetic cell from abiotic building blocks has been adopted. A wide range of representative synthetic cell models have been created based on this bottom-up approach, ranging from liposomes,[2] polymersomes,[3] proteinosomes[4], caposomes,[5] to coacervates.[6] Such compartmentalized systems provide a shielded inner milieu to allow efficient and undisturbed biochemical reactions to take place that could provide resources for adaptive life-like behaviours. Motility can be considered as a basic form of adaptivity, as living organisms migrate in response to environmental cues or energy sources. Though microscale swimmers have been designed theoretically and realized experimentally, motility mimicry in a synthetic cell system has only been reported recently. In this chapter, we summarize and discuss the recent advances in cellular mimicry, following the main outline of cellular evolution, from basic compartmentalization, biological reactions for energy production, to adaptive motility behaviour. We have limited ourselves to soft organic systems, and structures like bimetallic swimmers, which have been extensively reviewed,[7-16] are therefore beyond the scope of this introduction.

1.2 Biomimetic Soft Systems

Inspired by nature, researchers aim to create complex, multi-functional systems that are able to show life-like behaviours. Indeed, research towards protocellular systems is gaining increased attention. One significant feature in natural systems is compartmentalization, which is an essential element of all living systems – it allows complex reactions to occur with high efficiency whilst providing stabilizing and spatially ordered micro- and/or nano environments for diverse (complex) enzymatic networks. Membrane-bound biological systems (*e.g.*, mitochondria, endosomes or the nucleus) are examples of this compartmentalization strategy. The membranes confine, for example,

functional enzymes and genetic information, whilst facilitating and controlling molecular transport between different organelles. Engineering synthetic replicas of these biological systems has attracted the attention of many research groups across the globe. The demonstration of life-like behaviours (such as growth, division, metabolism and motility) based on artificial compartments whilst mimicking intricate structural features of biological systems is still a challenging task. In general, biological compartments are soft, allow selective exchange of small molecules, able to undertake various reactions without unwanted cross-talks. Soft synthetic compartments (artificial cell candidates) are mainly built from liposomes, proteinosomes, coacervates, polymersomes and capsosomes, as shown in **Figure 1-2**. Their capabilities to display various properties is dictated by the chemical structure of their components and/or their formation process, which enables control over size, shape, response to pH and temperature, amphiphilicity, and biofunctionalization. Detailed fabrication strategies have been extensively reviewed elsewhere and will not be discussed here.[2-3, 17-22]

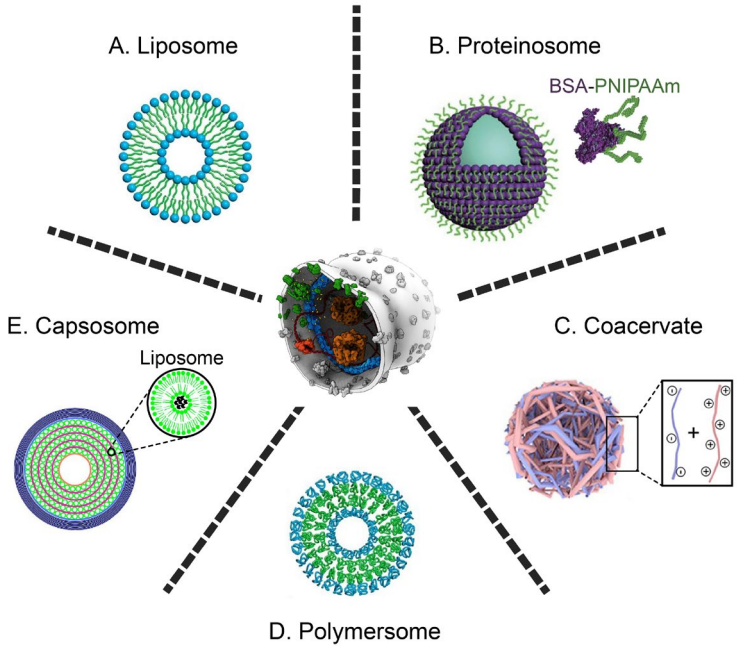

Figure 1-1 | Systematic overview of biomimetic scaffolds. Center image shows an artistic impression of a synthetic cell (Credit: Graham Johnson / BaSyC consortium); **A-E** show potential constructs as cell-mimetics – which are soft, semi-permeable and compartmentalized systems. Adapted with permissions.[23-26] Copyright 2010, ACS. Copyright 2013, Nature. Copyright 2019, Portland press. Copyright 2014, United States National Academy of Sciences.

Tunable permeability of soft compartments, which enables in- and efflux of substrates and products, is a vital property when mimicking a living cell and has been realized in different artificial cell platforms. Exemplary of this are the polymersomes self-assembled from PEGylated polycationic and PEGylated polyanionic polymers (PICsomes) with loosely packed membrane, which permits free diffusion of small molecules.[27] For liposomes or polymersomes that are not inherently permeable, they can be engineered to be permanently permeable through the insertion of membrane proteins (such as OmpF, α-hemolysin or melittin) or DNA nanopores.[28-30] For example, Noireaux et al. utilized giant liposomes as a platform for cell-free protein synthesis. They successfully reconstituted α-hemolysin into the lipid membrane without disruption, which allowed externally added nutrients (amino acids, nucleotides) to enter liposomes and efficiently prolonged *in vitro* transcription and translation mediated protein expression.[31] Another widely used approach is the on-demand control of permeability, which was achieved through the design of membranes that comprise stimulus-responsive moieties. Such permeability can be switched either on or off upon triggers such as pH,[32] temperature,[33] redox[34] or light.[35] Built from naturally occurring proteins, a new class of soft vesicles, proteinosomes[23, 36] have been shown to possess tunable permeability through a "self-sacrificing" strategy. The permeability of the membrane was tuned by first assembling the proteinosomes from different proteins, which was followed by subsequent removal of one or more protein species from the membrane by tris(2-carboxyethyl)phosphine (TCEP) mediated disulfide cleavage and protease degradation.[37] By the combination of these methods, proteinosomes were made permeable toward macromolecules with molecular weight up to 70 kDa.

There are also soft compartments that are inherently membrane-free. A membrane-less coacervate was reported by Oparin as a prebiotic protocell model and a basic metabolic unit resembling those formed on the early Earth before the formation of membranes.[38] Membrane generation is a complex process and the exchange of compounds between a membrane-delimited compartment and external environment requires complicated enzymes and proteins that did not exist in prebiotic time.[39]

The main class of membraneless compartments in artificial cell research is based on complex coacervates. These structures are assembled from oppositely charged synthetic polyelectrolytes or biomacromolecules (polysaccharides, polypeptides and nucleotides) have been widely studied and investigated as mimics of the crowded intracellular environment, providing a useful platform for the modelling cellular behaviour *in vitro*.

Coacervates formed from small nucleotides and polycationic species have been investigated as a novel protocell model. The properties and behaviour of the nucleotide-based coacervates are unique as the viscoelastic, crowded phase can readily sequester a host of molecular and macromolecular components dependent upon their charge and hydrophobicity. The efficacy of the crowded internal environment of coacervates has been utilized to activate a complex multi-enzyme system (minimal polyketide synthase) with up to 20-fold rate increase – due to enrichment of enzymes and stabilization of enzyme complexes arising from the interactions with the crowded environment.[40] Membrane-free coacervates assembled from peptide/ nucleotide and polymer/nucleotide are able to endure dynamic environmental changes (e.g. pH and temperature) and selectively sequester and concentrate molecules.[41-42] Polymer/nucleotide coacervates which were assembled from (poly(diallyldimethylammonium) chloride (PDDA) and adenosine triphosphate (ATP)) displayed the sequestration ability toward a wide range of objects, including nanoparticles and proteins.[41] Recently, Kumar et al. reported the encapsulation of an organelle chloroplast in a polymer/polysaccharide coacervate (**Figure 1-2A**). Such a complex was able to display light-induced electron transfer, which is an important first step in photosynthesis, representing an excellent example of a synthetic cell with a functional organelle.[43]

The coacervates' membrane-less nature renders them a rudimentary form of protocells, which lacks a strong resemblance to eukaryotic cells.[1, 44] Such coacervate systems are sensitive to ionic strength and easily dissociated at sufficiently high salt concentration. To overcome this limitation, our group reported semipermeable membrane-stabilized coacervates.[45] They were assembled from oppositely charged amylose derivatives, and stabilized by the addition of a terpolymer, comprised of a hydrophilic poly(ethylene glycol) segment, a hydrophobic poly(caprolactone-gradient-trimethylene carbonate) domain and a negatively charged poly(glutamic acid) block, which interacted with the net positively charged coacervate phase (**Figure 1-2C**). This protocell system was used to mimic cellular compartmentalization, emulating the cellular logic of eukaryotic organisms.[26] This was accomplished by the spontaneous sequestration of proto-organelles, in this case, semi-permeable polymersomes, generating a unique biomimetic platform reminiscent of the spatial organization in eukaryotic cells. The importance of the presence of these proto-organelles was shown via the spatial ordering of incompatible enzymes to prevent catalytic cross-talks and proteolytic deactivation. Additionally, the

robust nature of this hierarchical system was highlighted in a co-culture experiment where the stability of such sub-compartmentalized protocell was maintained in the same medium as living cells. The robustness and versatility make this coacervate protocell a very promising candidate for biochemical functionalization and therefore an obvious choice as platform for the development of cellular motility mimics.

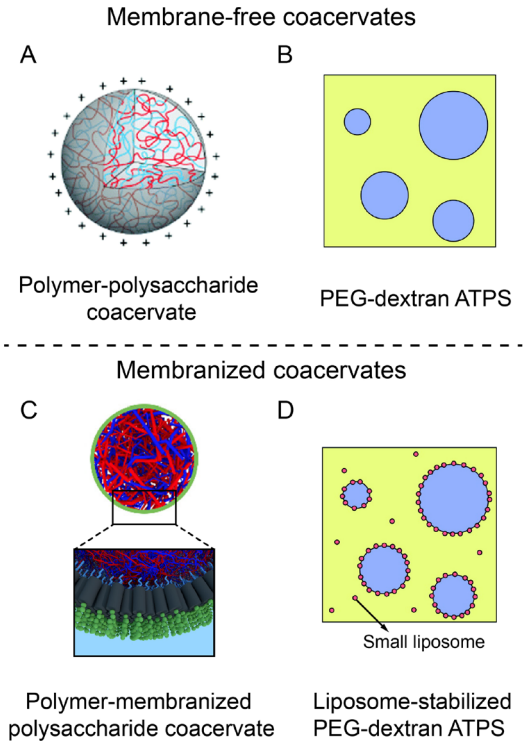

Figure 1-2 | Schematic illustration of membrane-free and membranized coacervates. **A.** Polymer/polysaccharide coacervate micro-droplets comprised of positively charged poly(diallyldimethylammonium chloride) (PDDA) and negatively charged carboxymethyl-dextran (CMDX); **B.** Aqueous two-phase system (ATPS) with dextran-rich phase dispersed in a continuous PEG-rich phase; **C.** Hierarchical structure of a triblock polymer-membranized coacervate with oppositely charged amylose biopolymers in the coacervate core; **D.** Small liposome-stabilized ATPS coacervates. Adapted with permissions.[43, 45-46] Copyright, ACS. Copyright, RSC.

Another category of coacervates are aqueous two-phase systems (ATPS), which have also been adapted to mimic cells.[47] The most common type of ATPS comprises two water-soluble polymers, such as poly(ethylene glycol) (PEG) and dextran (**Figure 1-2B**). When the concentrations of both PEG and dextran are sufficiently high, macrophase separation

occurs.[46] The partitioning of compounds between the two phases endows the formed system with the ability of spatial separation and enrichment of molecules. Due to the difference in hydrophobicity in the PEG and dextran-rich phases, functional proteins accumulate in the dextran-rich phase and denatured proteins in the PEG-rich phase (as the exposed hydrophobic areas in denatured proteins match the more hydrophobic PEG). Moreover, the partitioning process is dependent on the size of the solutes. Similar to complex coacervate systems, the stability of ATPS coacervates can be drastically increased after membrane formation, using for example polymers or lipids (**Figure 1-2D**).[48]

1.3 Soft Compartments as Artificial Life-like Biochemical Reactors

Metabolism is a key biochemical activity, responsible for harnessing external sources of energy (fuel) and converting them into another form of energy essential to the cell's survival. Via metabolic processes cells are able to physically respond to chemical triggers, which can lead to, for example, motility or changes of the cells' shape (deformation). This section will describe different approaches how synthetic soft compartments are endowed with biochemical processes. We classify biochemical reactors reported so far into two categories, namely systems that enable kinetic enhancement or modulation of the biochemical process.

The kinetic enhancement of enzymatic reactions

Cellular machineries allow reactions to proceed with unsurpassed efficiency and specificity. Biological catalysts, enzymes, ensure a low activation energy barrier whilst enabling efficient conversion of substrates. Cells deploy various mechanisms to ensure such efficiency, such as substrate channeling and metabolon formation. The spatial organization of enzymes leads to a number of benefits for the overall process: i) lag times are reduced by consecutive conversion of intermediate products; ii) kinetics and thermodynamics of enzymatic processes are regulated by optimizing substrate-enzyme binding processes. Translating this information towards enzymatic kinetic enhancement in cell-like soft systems is an emerging topic, which has been demonstrated by several groups. Mann's group showed enhanced ATP-dependent enzymatic reactions in a membrane-less nucleotide/peptide coacervate.[49] ATP was utilized as a building block for their coacervate protocell model. The ATP-rich coacervate phase permitted efficient ATP-catalysed enzymatic reactions in such a confined and crowded environment. Indeed, hexokinase (HK), an enzyme that requires ATP for its function, displayed two times faster

kinetics when it was sequestered in the coacervate phase. Besides HK sequestration, which led to high local enzyme concentration, also the hydrophobic modulation of HK via the interaction between hydrophobic motifs of HK and the hydrophobic droplet interior resulted in the enhanced kinetics.[50]

Similarly, Keating's group showed an enhancement of ribozymes' rate of catalysis when they were encapsulated in an aqueous two-phase (ATPS) membrane-less coacervate system,[51] comprised of poly(ethylene glycol) (PEG) and dextran. As the polar character of the ribozyme more closely resembled that of dextran, the catalyst was sequestered into the dextran-rich phase.[46] The partitioning of ribozymes was found to be dependent on the length of the ribozyme RNA strand that was used, allowing control over selective uptake and/or exclusion. The enrichment of ribozymes in the coacervate phase led to a 70-fold kinetic enhancement. This was mainly attributed to enrichment (at least a 100-fold concentration in the RNA-enriched dextran-rich phase). Due to the limited stability of such ATPS coacervate systems, the same group developed a system which was stabilized using nanoscale liposomes (d~130 nm), forming a Pickering type emulsion with a dextran-rich phase dispersed in continuous PEG-rich phase.[48] The additional layer of liposomes at the emulsion interface provided extra stability whilst allowing the in-/out- transport of RNA and DNA across the liposomal layer. Additionally, the ribozyme cleavage reaction enhancement was maintained at the same level after liposomal stabilization. These features make the liposome stabilized coacervate a good candidate for a protocellular reactor.

Another example of utilizing liposomes as subcompartments in protocell models are the capsosomes. The spatial organization of liposomes in such protocells facilitates biochemical processes without destructive cross-talk. As an example, Hosta-Rigau et al. carried out an enzyme cascade comprising uricase and horseradish peroxidase (HRP) enzymes, with both enzymes loaded separately in two populations of liposomes before they were assembled into capsosomes as liposomal subcompartments. Capsosomes are constructed via a layer-by-layer approach in which the liposomes are layered in between polymers with opposite charge (see **Figure 1-1E**). Subcompartmentalized enzymes showed enzymatic turnover and steadily increased conversion over time.[5] Additionally, a third reaction involving ascorbate oxidase (AO) was performed parallel in liposomal subcompartments to the aforementioned uricase-HRP enzyme cascade. The ability to perform multiple enzyme reactions in the subcompartments of a concentric system is

reminiscent of organisms with enzymatic reactions performing in the middle space of their double membranes (*e.g.* mitochondria).

Similarly, a coacervate protocell with hierarchal subcompartmentalization (polymersome-in-coacervate protocell) has been demonstrated by our group.[26] Polymersomes, pre-loaded with glucose oxidase (GOx) and/or HRP, as proto-organelle were encapsulated in the interior of coacervate protocells. Two different spatial layouts of enzymes were obtained – GOx and HRP were separately encapsulated in polymersomes, or GOx and HRP were co-encapsulated in one population of polymersomes. As expected, the kinetic enhancement employing co-encapsulation surpassed separate encapsulation, since GOx and HRP remained in proximity in one polymersome in the case of co-encapsulation, and the intermediate substrate hydrogen peroxide did not need to diffuse across polymeric membranes to be converted (**Figure 1-3A**). Moreover, the cascade was still performed successfully in the case of separate encapsulation, illustrating the transmembrane and cross-interior transport of intermediates from one polymersome to the other, which endowed such protocells with the ability of inter-organelle communication. Multiple enzymes were also incorporated in a polymersome system with spatial control.[52] Three enzymes, *Candida antarctica* lipase B (CALB), glucose oxidase (GOx) and horseradish peroxidase (HRP) were each located in different domains. GOx was encapsulated in the aqueous lumen of the polymersome, HRP was placed in the polymersomal membrane and CALB was added to the external milieu. A cascade reaction was smoothly performed upon the addition of substrate to the external solution.

Modulation of enzyme activity

Enzyme activity is modulated by various factors, including enzyme conformation and structure, dynamics and substrate / active site accessibility. Modulating enzyme activity is critical to regulating enzymatic networks in biology. Attempting to replicate such behaviour in the lab, several methods have been developed, such as spatial organization of enzymes, responsive substrate entry upon tunable membrane permeability and incorporation of positive and negative feedback routes.[53-54] One example of the role of spatial organization in modulating the rate of enzymatic reactions has been presented by Huang et al.[55] They incorporated a functional enzymatic cascade comprising three enzymes; glucose amylase (GA), GOx and HRP, in proteinosomes.[55] These three enzymes were conjugated to PNIPAAm to form amphiphilic protein-polymer nanoconjugates, as the building blocks of the membrane of the proteinosomes. Using starch as a substrate, a

significant variation of activity was observed upon translocation of intermediate products glucose and hydrogen peroxide around the proteinosomes (**Figure 1-3B**). When either GOx or HRP was moved from the membrane into the aqueous lumen of the proteinosomes, the reaction rate remained constant. The semi-permeability of the membrane played a key role – substrates for both GOx and HRP are small enough to diffuse over the proteinosome membrane, therefore relocation of either enzyme had no impact on the overall cascade reaction rate. As expected, however, the reaction rate was reduced by *ca.* 90% when GA was translocated to the lumen. This was attributed to the diffusion-limited uptake of the GA substrate, starch, which cannot diffuse across the proteinosome membrane. Moreover, proteinosomes were shown to have a membrane thermo-responsive behaviour, as PNIPAAm possesses a lower critical solution temperature (LCST) at 33°C, which was used to modulate peroxide myoglobin activity upon encapsulation in proteinosomes.[23] The reaction rate increased with elevated temperature until 33°C, after which a drastic drop of the reaction rate was observed. By increasing or decreasing the temperature, a high degree of control over the permeability of the proteinosome membrane toward substrate was achieved, and as such a switch of activity of encapsulated peroxidase myoglobin; this feature could also be employed in controlled release of chemicals, for example in protocellular communication.

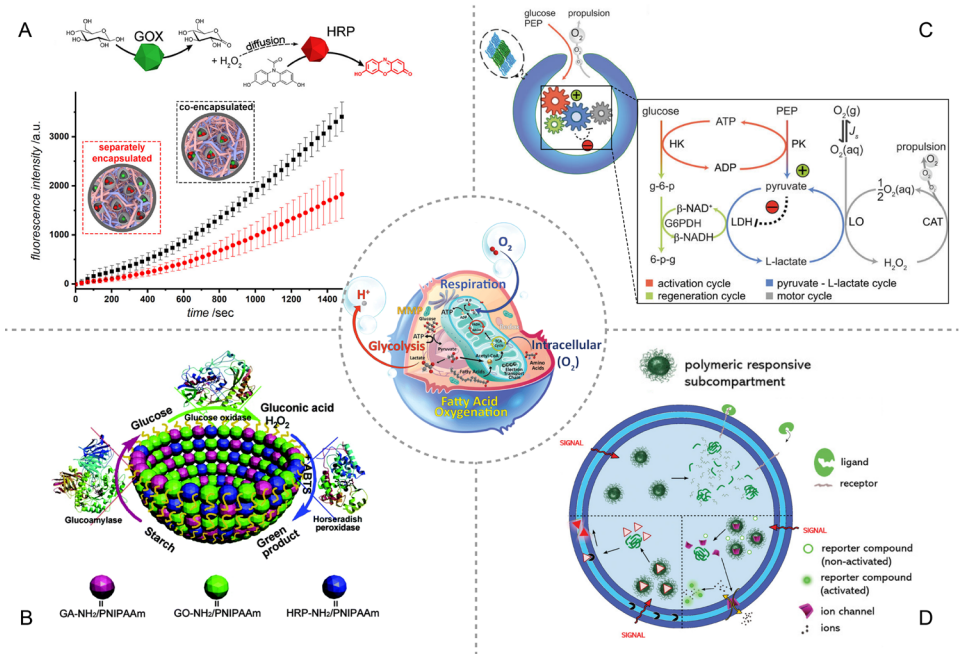

Figure 1-3 | Schematic representation of soft compartments as artificial life-like biochemical reactors. **A.** A two-step enzymatic reaction in a multicompartmentalized polymersome-in-coacervate system; **B.** A proteinosome membrane-mediated three-stage cascade reaction in water; **C.** A compartmentalized metabolic network confined in a stomatocyte; **D.** A modular multicompartment system composed of reduction sensitive subcompartments for triggered enzymatic activity and ion channel recruitment, encapsulated within polymeric giant unilamellar vesicles. Adapted with permissions.[26, 34, 52, 55-56]

A metabolic pathway comprising a network of 6 enzymes with regulatory feedback was sequestered inside the aqueous cavity of bowl-shaped polymer vesicles, or stomatocytes.[56] This enzymatic network was operated far from equilibrium and able to convert chemical fuel (glucose) into kinetic energy as output (**Figure 1-3C**). The metabolic network, starting with an ATP-mediated reaction cycle containing hexokinase (HK) and pyruvate kinase (PK), used ATP as an internal regulator to modulate the reaction rate of a second circle comprising a self-inhibitory enzyme at high substrate concentration. Furthermore, the output of this compartmentalized out-of-equilibrium network was sustained even at very low concentration of fuel (< 5mM), which was due to the built-in modulation regulatory machinery. Similarly, metabolic mimicry has been performed in a multi-compartmentalized polymersome-in-polymer capsule.[33] Utilizing an enzyme cascade comprising GOx and myoglobin, Voit and Appelhans et al. demonstrated biomimetic metabolism through communication between sub-compartmentalized polymersomes. Moreover, the authors showed the ability to control this behaviour by using external stimuli such as pH and temperature. To do so, polymersomes (as artificial organelles) were made from poly(ethylene glycol)-*b*-poly(2-(diethylamino)ethyl methacrylate)-stat-2-hydroxy-4-(methacryloyloxy) benzophenone (PEG-PDEAEMA-stat-BMA) and polymer capsules were made from poly(N-isopropyl acrylamide)-*b*-poly(methacrylic acid)-(3,4-dimethyl maleic imidobutyl methacrylate) (PNIPAAm-*b*-PMAA-DMIBM), which contained a pH-responsive PDEAEMA segment and a temperature-responsive block PNIPAAm respectively. These two segments enabled enhanced permeability at acidic (pH < 6.9) and low temperature (T < 32 ˚C) conditions, which allowed the system to control substrate access to encapsulated enzymes and therefore activity modulation with the dual responsiveness of the membrane (**Figure 1-3D**). It is worth mentioning that the spatial positioning of enzymes, by increasing or decreasing the diffusiometric barriers, played a role in controlling enzymatic activity. The close proximity of two kinds of enzymes was shown to benefit cascade activity. This kind of behaviour is indeed expected and, in the future, can be utilized towards various applications requiring control over enzyme activity.

The aforementioned representative examples provide insights in designing artificial cell models with enzymatic reactions; the output of these processes can be used for a wide range of applications, from the production of target molecules to chemical signalling and motility. Moreover, the ability to modulate output via (multi-)compartmentalization and various types of tunable permeability enables improved control over these cell mimetic systems. This is a significant step towards mimicry of more complex life-like features.

1.4 Motility Mimicry

Nature offers numerous types of motile behaviour of microscopic life, such as cells or bacteria, which move through liquids by different motion styles, including swimming, gliding, twitching or floating.[57-58] Many of them follow a tactic rule, *i.e.* they sense gradients and then move towards or away from the gradient, which enables cells to adapt to their favourable environments. Inspired by these natural swimmers, cell-like structures have been constructed with motility and self-propulsion. From a fundamental point of view, both natural and synthetic compartments need to overcome thermal fluctuations and low Reynolds numbers (viscous forces) to achieve self-propulsion. However, the absence of inertia and dominance of viscous forces at micro- and nano- length scales (leading to low Reynolds numbers) make it impossible to employ conventional swimming mechanisms, and no net displacement is achieved by for example flapping two (micro)arms in a time-reversal manner.[59-60] Additionally, Brownian motion due to thermal fluctuations makes it challenging for swimmers to generate constant and directed motion and maintain their orientations.[61] To this end, synthetic swimmers are generally designed to comprise out-of-equilibrium machineries that can convert energy from their surroundings to mechanical energy to overcome such obstacles. From a practical point of view, to generate and control propulsion lie at the core of various potential microscale technologies. Moreover, a better control over motility could help to reproduce cellular functionalities such as communication and sensing.[16]

Many investigations have been carried out on inorganic active matter systems, for example, Janus motors comprised of bimetallic materials or organic/inorganic hybrid materials (i.e. polymers and metallic coating).[62-68] However, these structures are far away from the regular components of which cells are composed of, and the design and construction of self-propelled cell-like compartments in fact still remain challenging. Only recently there have been the first examples of soft compartments capable of autonomous

motion.[69-72] This section will focus on the recent developments on self-propelled synthetic soft compartments that are akin to motile cell models.

In most cases, self-propulsion can be used interchangeably with autonomous motion, which is characterized by the independent moving trajectory of each motile compartment.[73] These motors generally convert source energy to mechanical propulsion locally. For example, chemically driven swimmers are normally considered autonomous and self-propulsive, whereas motors driven by externally applied fields (i.e. magnetic or electric field)[74-75] are commonly non-autonomous. These externally driven motors normally move along electric or magnetic field lines, while autonomous motors move as if they have their own destination. However, there are exceptions of externally driven motors that are autonomous in nature. A notable example is Janus particles half-coated with a light-absorbing gold layer that were able to generate a local thermal gradient, leading to autonomous motion under an externally applied light field.[76] Although externally driven motion allows functions such as navigation and highly accurate manipulation,[77-78] autonomous motion is at the core of mimicking cellular motility and more complex behaviours (i.e., swarming and quorum sensing).

Among several theoretically proposed propulsion mechanisms to drive autonomous motion, two of them have attracted growing attention – phoretic motion and the Marangoni effect. Phoretic motion relies on the interaction between a motile particle and its surrounding field, such as a chemical concentration gradient or temperature gradient, while the Marangoni effect is based on surface tension gradients of the active droplet, leading to fluid flow and therefore propulsion.[79-85]

Phoretic motion

It is important to note that phoretic motion is a force-free and torque-free propulsion mechanism; the local gradient that the active particle interacts with could be externally imposed (named phoresis) or be a result of symmetry breaking of the active particle itself (named self-phoresis).[86-88] Such symmetry breaking could be achieved in the form of asymmetric particle composition, shape or surface reactions. One famous example of symmetry breaking in particle composition are Janus swimmers with one half decorated with catalysts and the other half being inert. Such swimmers only generate product molecules on one side and therefore produce an asymmetric chemical field gradient. This asymmetry in product molecule field induces an osmotic imbalance and leads to autonomous motion.[16, 88] Based on different field gradients, common phoretic self-

propulsion mechanisms can be categorized into several classes: (i) Self-electrophoresis: the active particle responds to a self-generated electric field gradient; (ii) Self-diffusiophoresis: the active particle responds to inhomogeneous distribution of solute molecules (a self-generated chemical field gradient); (iii) Self-thermophoresis: the active particle responds to a temperature gradient.

Experimentally, the phoretic mechanism can be used solely or in tandem with other mechanisms to propel soft artificial compartments. Our group reported autonomous motion of soft nanosized polymersomes assembled from PEG-*b*-PS block copolymers.[70, 89] Such polymersomes were folded inward to form bowl-shaped particles, or "stomatocytes" via an osmotically induced shape transformation process (**Figure 1-4A**). Polymersomes can be shape-transformed into stomatocytes via several approaches – all of which involve the introduction of an osmotic imbalance over the membrane, leading to an outflow of solvent from the polymersome lumen and thus, volume reduction and consequent shape transformation. Such stomatocytes possess dual compartments and are able to encapsulate enzymes in their cavity. Furthermore, due to their unique asymmetric shape, they can be engineered into motile particles. By encapsulation of catalase (CAT), which decomposes hydrogen peroxide into water and oxygen, and an enzymatic cascade couple CAT-GOx, of which the latter decomposes glucose into hydrogen peroxide in the nanocavity of stomatocytes, these particles achieved autonomous motion (up to 176 body lengths /s) in the presence of respective fuel.[70] The propulsion mechanism was proposed to be fuel concentration dependent, suggesting self-diffusiophoresis at low concentration and bubble propulsion at high concentration of hydrogen peroxide.[70] Further control over the propulsion speed of stomatocytes was achieved by grafting thermosensitive polymer brushes poly(N-isopropylacrylamide) (PNIPAAm) on the surface of stomatocytes.[90] Increasing temperature above the lower critical solution temperature (LCST) of PNIPAAm led to collapse of the polymer and therefore closing of the neck of the stomatocytes and no entrance for fuel.

To fulfil the requirement of self-propulsion, asymmetry in polymersome shape can be alternatively achieved through membrane topology. Battaglia et al. reported that an asymmetric polymersome, assembled from two different kinds of copolymers with encapsulated CAT and/or GOx in the lumen, was capable of chemotaxis and biological barrier crossing.[91] The two copolymers forming the polymersomal membrane phase separated into two individual domains (**Figure 1-4B**). One domain was comprised of poly(ethylene oxide)-poly(butylene oxide)(PEO-PBO) with the PBO segment highly

permeable toward enzyme substrate and product (glucose and hydrogen peroxide). As such, a product molecule gradient was preferably generated at the PEO-PBO side, leading to diffusiophoretic behaviour and eventually self-propulsion. Moreover, chemotactic behaviour of such asymmetric polymersomes has been displayed toward high glucose concentration, where an alternation of propulsion and reorientation has been observed during chemotaxis.[91]

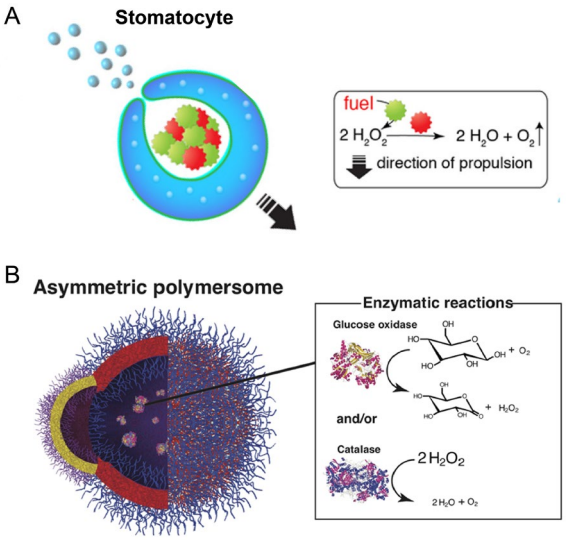

Figure 1-4 | **A.** Schematic representation of a stomatocyte assembled from PEG-PS propelled by an enzyme cascade reaction of glucose oxidase and catalase. **B.** Schematic representation of an asymmetric chemotactic polymersome using a combination of PEO-PBO mixed with either poly[(2-methacryloyl) ethyl phosphorylcholine]–poly[2-(diisopropylamino)ethyl methacrylate] (PMPC-PDPA) or poly[oligo(ethylene glycol) methyl methacrylate] (POEGMA)–PDPA. Adapted with permissions.[70, 91] Copyright 2017, AAAS.

Marangoni effect

Besides the abovementioned examples of intrinsic asymmetry through swimmer geometry (i.e., asymmetric polymersomes), symmetry breaking can be alternatively achieved by instantaneous or dynamic asymmetry. Active droplets driven by the Marangoni effect are a notable example of such instantaneous asymmetry. The Marangoni effect originates from the surface tension gradient at a fluid-fluid interface (fluid flows from a low surface tension area to a high surface tension area), which arises from the response of droplets to temperature or concentration gradients in the surroundings.[81] In most cases, droplets of one liquid are dispersed in another immiscible liquid (continuous phase) and stabilized by surfactants at the liquid-liquid interface.[81, 92]

In the absence of any gradients, surfactant molecules distribute homogenously along the droplet interface and the whole system is symmetric (**Figure 1-5A**). However, if the local surfactant concentration at the interface changes, symmetry is broken, and such spontaneous asymmetric surface tension leads to a surrounding liquid flow around the droplets and eventually self-propulsion (**Figure 1-5A**).

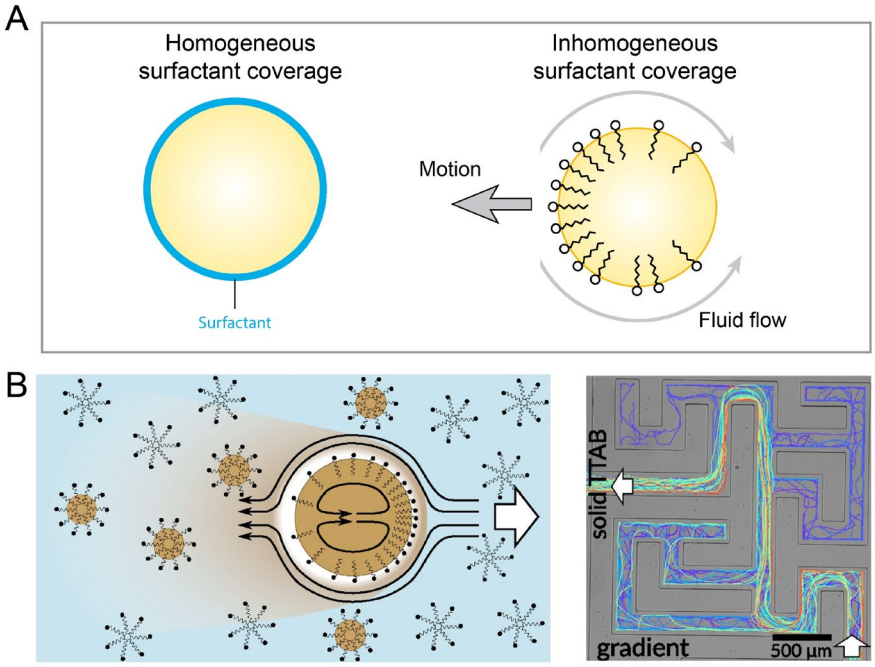

Figure 1-5 | Active droplets driven by the Marangoni effect. **A.** Droplets with homogenous and inhomogeneous interfacial surfactant coverage. The curved grey arrows point towards the high surface tension area where surrounding liquid flows toward. The droplet moves to the opposite direction. **B.** Oil droplets driven by the Marangoni effect arising from micellar solubilization are capable of positive chemotaxis and maze solving. Adapted with permissions.[79, 81] Copyright 2016 by Annual Reviews.

A surface tension gradient is required to drive droplets by Marangoni stress. To maintain a surface tension difference at the interface, surfactant gradients could be sustained by a chemical reaction or micellular solubilization.[79-85] Maass et al. reported a self-propelled droplet system capable of chemotaxis similar to that of a biological system.[79] They dissolved an oil phase consisting of 4-pentyl-4'-cyano-biphenyl (5CB) in an ionic surfactant tetradecyltrimethylammonium bromide (TTAB) containing solution. During the dissolution, oil molecules from the oil droplets continuously migrated to the centre of the surfactant micelles in the aqueous solution. This random migration led to

inhomogeneous surfactant coverage of oil droplets and induced Marangoni flow surrounding the oil droplets, eventually resulting in self-propulsion (**Figure 1-5B**). Furthermore, oil droplets displayed positive chemotaxis toward the TTAB gradient. Taking advantage of their chemotactic behaviour, such active droplets demonstrated biomimetic maze solving ability when TTAB solid was placed at the exit of maze.[79] Inhomogeneous surfactant coverage arising from a chemical reaction has also been employed in cellular motility mimicry. An active droplet driven by bond-forming reactions of lipid surfactants has been reported by Katsonis et al.[83] Interestingly, the Marangoni effect working in tandem with diffusiophoretic Janus micromotors has been shown to lead to collective behaviour.[84] At high micromotor density, their catalytic half decomposed hydrogen peroxide and generated oxygen at high speed and caused nucleation and growth of oxygen bubbles. Such bubble growth in the aqueous solution gave rise to Marangoni flow around the bubbles, leading to collective migration of micromotors toward the centre of the oxygen bubble.[84]

Other propulsion mechanisms

In addition to phoretic motion and the Marangoni effect, several other mechanisms have been employed to build self-propelled soft compartments and mimic cellular motility. For instance, Mann's group designed a catalase-containing organoclay/DNA semipermeable microcapsule, which in the presence of hydrogen peroxide exhibits enzyme-mediated oxygen bubble-dependent buoyancy.[71] Such buoyant motion of a giant protocell model could reach up to 40 mm/s and was offset by competing GOx-mediated consumption of the entrapped bubbles, which mimicked gas vesicle-mediated buoyancy of certain bacteria and archaea.[93] Based on the idea of buoyant motion, Wang et al. developed a system comprised of lipase-coated oil globules in water that are capable of seeking substrate upwards and settling down for digestion by adjusting their buoyancy through temperature-controlled enzyme reactions.[94] Inspired by actin polymerisation-induced motion of *Listeria*, Matsuura et al. developed a motile liposome system driven by light-responsive fibre growth at the posterior.[95] A photocleavable conjugate which released peptides was asymmetrically introduced to the surface of phase-segregated giant liposomes. Upon irradiation, peptides released from one side of the liposomes and self-assembled into nanofibers, driving propulsion of the liposomes, which is comparable to that of actin fibre-driven bacteria.[95]

1.5 Conclusions & Future perspective

The past decade has witnessed great progress in the emerging field of biomimicry – that is, as defined in this chapter, mimicking cellular behaviours *via* the "bottom-up" construction of cell-mimetic soft compartments. In order to construct such artificial cytomimetics, scientists from various disciplines have set out to engineer a diverse array of bio-inspired structural mimics, ranging from liposomes, polymersomes, proteinosomes to coacervates. Such soft architectures with unique physicochemical properties have advanced biomimetic processes in various aspects. Prominent advances include the construction of artificial cells with biocatalytic function mimicry of a rudimentary metabolism machinery inside soft compartments and better control over composition and permeability of artificial compartments. An important recent advance is the incorporation of motility, which can be triggered by signalling molecules and/or energy molecules in the system.

To further explore the possibilities of motile systems, an important next step would be incorporating propulsion mechanisms inspired by living systems into the design of next generation motors. In addition to their remarkable individual dynamics, it is worth exploring interactions between motors and their environments. An accurate description of their dynamics and environmental impact would provide an interesting platform to study fundamental processes and develop higher-order functionalities. In the end, mimicry of cellular functionalities will not only provide improved insights into fundamental principles of living systems, but could also pave the way for applications in nanotechnology and biomedicine with novel designs that can sense, respond to and interact with their surroundings.

1.6 Aim and Outline of this thesis

The general aim of this thesis is to develop a novel platform towards the microscopic engineering of motile and adaptive life-like systems. Various life-like functionalities and biomimetic processes, ranging from *in vitro* transcription-translation to cell budding and division, have been incorporated into synthetic cells. However, imitating cellular motility has been much less explored. In part, this is due to the lack of structural similarity between natural and synthetic systems, and the difficulty of integrating motion mechanisms in cell-mimetic systems. The bottom-up construction and engineering of a synthetic cell based micromotor is the objective of the research performed in **Chapter 2**, which demonstrates

control over size and (chemical) topology of a coacervate microdroplet cloaked with a polymer membrane. Such polymer membrane is endowed with chemical versatility which allows surface modification with catalytic species to drive autonomous motion. The fluidity and dynamicity of the membrane paves the way toward modulation of motion dynamics.

To propel at the microscale, random fluctuations are the first obstacle to overcome. Indeed, random fluctuations are inherent to all complex molecular systems. Nature has evolved mechanisms to control stochastic events to achieve the desired biological output. Inspired by this, **Chapter 3** presents an artificial platform based on coacervates that enables us to exploit stochasticity to direct motile behaviour. The fluidity of the polymer membrane and the diffusivity of surface propulsive units play a central role in generating a transient and dynamic asymmetry that imparts motility to such coacervates.

Motility is commonly studied as an individual functional element. Interaction between motors and their surroundings has important implications in the design of higher-order functionalities such as collective behaviour and inter-system communication. **Chapter 4** demonstrates a tunable experimental platform to gain insight into the dynamics of active particles in environments with restricted 3D topology. Self-propulsive soft micromotors are examined inside a larger soft lipid vesicle where confinement leads to a decrease in motility.

Chapter 5 presents a hierarchical motile system where propulsive nanoswimmers act as powering engine of a microscale soft compartment. As a motile unit, self-thermophoretic Janus swimmers recently reported by our group are employed. We encapsulate them inside coacervates to examine the transfer of phoretic motion from the individual nanoswimmers to the coacervate they reside in.

Finally, **Chapter 6** concludes this thesis and looks forward to further developments.

References

[1] Mason, A. F.; van Hest, J. C., Multifaceted cell mimicry in coacervate-based synthetic cells. *Emerging Top. Life Sci.* **2019,** *3* (5), 567-571.

[2] Rideau, E.; Dimova, R.; Schwille, P.; Wurm, F. R.; Landfester, K., Liposomes and polymersomes: a comparative review towards cell mimicking. *Chem. Soc. Rev.* **2018,** *47* (23), 8572-8610.

[3] Mason, A. F.; Thordarson, P., Polymersomes as protocellular constructs. *J. Polym. Sci., Part A: Polym. Chem.* **2017,** *55* (23), 3817-3825.

[4] Li, M.; Huang, X.; Tang, T.-Y. D.; Mann, S., Synthetic cellularity based on non-lipid micro-compartments and protocell models. *Curr. Opin. Chem. Biol.* **2014,** *22*, 1-11.

[5] Hosta-Rigau, L.; York-Duran, M. J.; Zhang, Y.; Goldie, K. N.; Städler, B., Confined multiple enzymatic (cascade) reactions within poly (dopamine)-based capsosomes. *ACS Appl. Mater. Interfaces* **2014,** *6* (15), 12771-12779.

[6] Mason, A. F.; Buddingh', B. C.; Williams, D. S.; van Hest, J. C., Hierarchical self-assembly of a copolymer-stabilized coacervate protocell. *J. Am. Chem. Soc.* **2017,** *139* (48), 17309-17312.

[7] Fernández-Medina, M.; Ramos-Docampo, M. A.; Hovorka, O.; Salgueiriño, V.; Städler, B., Recent Advances in Nano- and Micromotors. *Adv. Funct. Mater.* **2020,** *n/a* (n/a), 1908283.

[8] Gao, W.; Wang, J., The environmental impact of micro/nanomachines: a review. *ACS nano* **2014,** *8* (4), 3170-3180.

[9] Dey, K. K.; Sen, A., Chemically propelled molecules and machines. *J. Am. Chem. Soc.* **2017,** *139* (23), 7666-7676.

[10] Katuri, J.; Ma, X.; Stanton, M. M.; Sánchez, S., Designing micro-and nanoswimmers for specific applications. *Acc. Chem. Res.* **2016,** *50* (1), 2-11.

[11] Kuron, M.; Kreissl, P.; Holm, C., Toward Understanding of Self-Electrophoretic Propulsion under Realistic Conditions: From Bulk Reactions to Confinement Effects. *Acc. Chem. Res.* **2018,** *51* (12), 2998-3005.

[12] Ma, X.; Sánchez, S., Self-propelling micro-nanorobots: challenges and future perspectives in nanomedicine. *Nanomedicine* **2017**.

[13] Patiño, T.; Arqué, X.; Mestre, R.; Palacios, L.; Sánchez, S., Fundamental Aspects of Enzyme-Powered Micro-and Nanoswimmers. *Acc. Chem. Res.* **2018,** *51* (11), 2662-2671.

[14] Ren, L.; Wang, W.; Mallouk, T. E., Two Forces Are Better than One: Combining Chemical and Acoustic Propulsion for Enhanced Micromotor Functionality. *Acc. Chem. Res.* **2018,** *51* (9), 1948-1956.

[15] Šípová-Jungová, H.; Andrén, D.; Jones, S.; Käll, M., Nanoscale Inorganic Motors Driven by Light: Principles, Realizations, and Opportunities. *Chem. Rev.* **2020,** *120* (1), 269-287.

[16] Illien, P.; Golestanian, R.; Sen, A., 'Fuelled'motion: phoretic motility and collective behaviour of active colloids. *Chem. Soc. Rev.* **2017,** *46* (18), 5508-5518.

[17] Akbarzadeh, A.; Rezaei-Sadabady, R.; Davaran, S.; Joo, S. W.; Zarghami, N.; Hanifehpour, Y.; Samiei, M.; Kouhi, M.; Nejati-Koshki, K., Liposome: classification, preparation, and applications. *Nanoscale Res. Lett.* **2013,** *8* (1), 102.

[18] de Hoog, H.-P. M.; Nallani, M.; Tomczak, N., Self-assembled architectures with multiple aqueous compartments. *Soft Matter* **2012,** *8* (17), 4552-4561.

[19] Discher, D. E.; Ahmed, F., Polymersomes. *Annu. Rev. Biomed. Eng.* **2006,** *8*, 323-41.

[20] Patil, Y. P.; Jadhav, S., Novel methods for liposome preparation. *Chem. Phys. Lipids* **2014,** *177*, 8-18.

[21] van Swaay, D.; deMello, A., Microfluidic methods for forming liposomes. *Lab Chip* **2013,** *13* (5), 752-67.

[22] Walde, P.; Cosentino, K.; Engel, H.; Stano, P., Giant vesicles: preparations and applications. *ChemBioChem* **2010,** *11* (7), 848-65.

[23] Huang, X.; Li, M.; Green, D. C.; Williams, D. S.; Patil, A. J.; Mann, S., Interfacial assembly of protein–polymer nano-conjugates into stimulus-responsive biomimetic protocells. *Nat. Commun.* **2013,** *4*, 2239.

[24] Chandrawati, R.; Hosta-Rigau, L.; Vanderstraaten, D.; Lokuliyana, S. A.; Stadler, B.; Albericio, F.; Caruso, F., Engineering advanced capsosomes: maximizing the number of subcompartments, cargo retention, and temperature-triggered reaction. *ACS Nano* **2010,** *4* (3), 1351-61.

[25] Zhang, S.; Sun, H.-J.; Hughes, A. D.; Moussodia, R.-O.; Bertin, A.; Chen, Y.; Pochan, D. J.; Heiney, P. A.; Klein, M. L.; Percec, V., Self-assembly of amphiphilic Janus dendrimers into uniform onion-like

dendrimersomes with predictable size and number of bilayers. *Proc. Natl. Acad. Sci. U. S. A.* **2014,** *111* (25), 9058-9063.

[26] Mason, A. F.; Yewdall, N. A.; Welzen, P. L.; Shao, J.; van Stevendaal, M.; van Hest, J. C.; Williams, D. S.; Abdelmohsen, L. K., Mimicking Cellular Compartmentalization in a Hierarchical Protocell through Spontaneous Spatial Organization. *ACS Cent. Sci.* **2019,** *5* (8), 1360-1365.

[27] Koide, A.; Kishimura, A.; Osada, K.; Jang, W.-D.; Yamasaki, Y.; Kataoka, K., Semipermeable Polymer Vesicle (PICsome) Self-Assembled in Aqueous Medium from a Pair of Oppositely Charged Block Copolymers: Physiologically Stable Micro-/Nanocontainers of Water-Soluble Macromolecules. *J. Am. Chem. Soc.* **2006,** *128* (18), 5988-5989.

[28] Meier, W.; Nardin, C.; Winterhalter, M., Reconstitution of Channel Proteins in (Polymerized) ABA Triblock Copolymer Membranes. *Angew. Chem., Int. Ed.* **2000,** *39* (24), 4599-4602.

[29] Kumar, M.; Grzelakowski, M.; Zilles, J.; Clark, M.; Meier, W., Highly permeable polymeric membranes based on the incorporation of the functional water channel protein Aquaporin Z. *Proc. Natl. Acad. Sci. U. S. A.* **2007,** *104* (52), 20719.

[30] Belluati, A.; Mikhalevich, V.; Yorulmaz Avsar, S.; Daubian, D.; Craciun, I.; Chami, M.; Meier, W. P.; Palivan, C. G., How Do the Properties of Amphiphilic Polymer Membranes Influence the Functional Insertion of Peptide Pores? *Biomacromolecules* **2019,** *21* (2), 701-715.

[31] Noireaux, V.; Libchaber, A., A vesicle bioreactor as a step toward an artificial cell assembly. *Proc. Natl. Acad. Sci. U. S. A.* **2004,** *101* (51), 17669-17674.

[32] Gaitzsch, J.; Appelhans, D.; Wang, L.; Battaglia, G.; Voit, B., Synthetic Bio-nanoreactor: Mechanical and Chemical Control of Polymersome Membrane Permeability. *Angew. Chem., Int. Ed.* **2012,** *51* (18), 4448-4451.

[33] Liu, X.; Formanek, P.; Voit, B.; Appelhans, D., Functional cellular mimics for the spatiotemporal control of multiple enzymatic cascade reactions. *Angew. Chem., Int. Ed.* **2017,** *56* (51), 16233-16238.

[34] Thamboo, S.; Najer, A.; Belluati, A.; von Planta, C.; Wu, D.; Craciun, I.; Meier, W.; Palivan, C. G., Mimicking Cellular Signaling Pathways within Synthetic Multicompartment Vesicles with Triggered Enzyme Activity and Induced Ion Channel Recruitment. *Adv. Funct. Mater.* **2019,** *29* (40), 1904267.

[35] Wang, X.; Hu, J.; Liu, G.; Tian, J.; Wang, H.; Gong, M.; Liu, S., Reversibly Switching Bilayer Permeability and Release Modules of Photochromic Polymersomes Stabilized by Cooperative Noncovalent Interactions. *J. Am. Chem. Soc.* **2015,** *137* (48), 15262-15275.

[36] Shi, P.; Qin, J.; Wu, X.; Wang, L.; Zhang, T.; Yang, D.; Zan, X.; Appelhans, D., A Facile and Universal Method to Efficiently Fabricate Diverse Protein Capsules for Multiple Potential Applications. *ACS Appl. Mater. Interfaces* **2019,** *11* (42), 39209-39218.

[37] Liu, L.; Su, D.; Liu, X.; Wang, L.; Zhan, J.; Xie, H.; Meng, X.; Zhang, H.; Liu, J.; Huang, X., Construction of biological hybrid microcapsules with defined permeability towards programmed release of biomacromolecules. *Chem. Commun.* **2017,** *53* (85), 11678-11681.

[38] Kolb, V. M., *Handbook of Astrobiology*. CRC Press: 2018.

[39] Vieregg, J. R.; Tang, T. D., Polynucleotides in cellular mimics: coacervates and lipid vesicles. *Curr. Opin. Colloid Interface Sci.* **2016,** *26*, 50-57.

[40] Crosby, J.; Treadwell, T.; Hammerton, M.; Vasilakis, K.; Crump, M. P.; Williams, D. S.; Mann, S., Stabilization and enhanced reactivity of actinorhodin polyketide synthase minimal complex in polymer–nucleotide coacervate droplets. *Chem. Commun.* **2012,** *48* (97), 11832-11834.

[41] Williams, D. S.; Koga, S.; Hak, C. R. C.; Majrekar, A.; Patil, A. J.; Perriman, A. W.; Mann, S., Polymer/nucleotide droplets as bio-inspired functional micro-compartments. *Soft Matter* **2012,** *8* (22), 6004-6014.

[42] Tang, T.-Y. D.; Antognozzi, M.; Vicary, J. A.; Perriman, A. W.; Mann, S., Small-molecule uptake in membrane-free peptide/nucleotide protocells. *Soft Matter* **2013,** *9* (31), 7647-7656.

[43] Kumar, B. P.; Fothergill, J.; Bretherton, J.; Tian, L.; Patil, A. J.; Davis, S. A.; Mann, S., Chloroplast-containing coacervate micro-droplets as a step towards photosynthetically active membrane-free protocells. *Chem. Commun.* **2018,** *54* (29), 3594-3597.

[44] Yewdall, N. A.; Mason, A. F.; van Hest, J. C. M., The hallmarks of living systems: towards creating artificial cells. *Interface Focus* **2018,** *8* (5), 20180023.

[45] Mason, A. F.; Buddingh', B. C.; Williams, D. S.; van Hest, J. C. M., Hierarchical Self-Assembly of a Copolymer-Stabilized Coacervate Protocell. *J. Am. Chem. Soc.* **2017,** *139* (48), 17309-17312.

[46] Keating, C. D., Aqueous phase separation as a possible route to compartmentalization of biological molecules. *Acc. Chem. Res.* **2012,** *45* (12), 2114-2124.

[47] Aumiller Jr, W. M.; Keating, C. D., Phosphorylation-mediated RNA/peptide complex coacervation as a model for intracellular liquid organelles. *Nat. Chem.* **2015,** *8*, 129.
[48] Dewey, D. C.; Strulson, C. A.; Cacace, D. N.; Bevilacqua, P. C.; Keating, C. D., Bioreactor droplets from liposome-stabilized all-aqueous emulsions. *Nat. Commun.* **2014,** *5* (1), 4670.
[49] Koga, S.; Williams, D. S.; Perriman, A. W.; Mann, S., Peptide–nucleotide microdroplets as a step towards a membrane-free protocell model. *Nat. Chem.* **2011,** *3* (9), 720.
[50] Ehsani-Zonouz, A.; Golestani, A.; Nemat-Gorgani, M., Interaction of hexokinase with the outer mitochondrial membrane and a hydrophobic matrix. *Mol. Cell. Biochem.* **2001,** *223* (1-2), 81-87.
[51] Strulson, C. A.; Molden, R. C.; Keating, C. D.; Bevilacqua, P. C., RNA catalysis through compartmentalization. *Nat. Chem.* **2012,** *4*, 941.
[52] Vriezema, D. M.; Garcia, P. M.; Sancho Oltra, N.; Hatzakis, N. S.; Kuiper, S. M.; Nolte, R. J.; Rowan, A. E.; van Hest, J. C., Positional assembly of enzymes in polymersome nanoreactors for cascade reactions. *Angew. Chem., Int. Ed.* **2007,** *46* (39), 7378-82.
[53] Su, J.; Wang, S.; Xu, Z.; Wu, G.; Wang, L.; Huang, X., Interfacial self-assembly of gold nanoparticle-polymer nanoconjugates into microcapsules with near-infrared light modulated biphasic catalysis efficiency. *Chem. Commun.* **2019,** *55* (72), 10760-10763.
[54] Li, J.; Liu, X.; Abdelmohsen, L. K. E. A.; Williams, D. S.; Huang, X., Spatial Organization in Proteinaceous Membrane-Stabilized Coacervate Protocells. *Small* **2019,** *15* (36), e1902893.
[55] Huang, X.; Li, M.; Mann, S., Membrane-mediated cascade reactions by enzyme-polymer proteinosomes. *Chem. Commun.* **2014,** *50* (47), 6278-80.
[56] Nijemeisland, M.; Abdelmohsen, L. K.; Huck, W. T.; Wilson, D. A.; van Hest, J. C., A compartmentalized out-of-equilibrium enzymatic reaction network for sustained autonomous movement. *ACS Cent. Sci.* **2016,** *2* (11), 843-849.
[57] Kearns, D. B., A field guide to bacterial swarming motility. *Nat. Rev. Microbiol.* **2010,** *8* (9), 634-44.
[58] Lin, Y.; Wang, L.; Huang, X., Dynamic Behaviour in Microcompartments. *Chem. - Eur. J.* **2019,** *25* (72), 16440-16450.
[59] Lauga, E., Life around the scallop theorem. *Soft Matter* **2011,** *7* (7), 3060-3065.
[60] Purcell, E. M., Life at low Reynolds number. *American journal of physics* **1977,** *45* (1), 3-11.
[61] Romanczuk, P.; Schimansky-Geier, L., Brownian Motion with Active Fluctuations. *Phys. Rev. Lett.* **2011,** *106* (23), 230601.
[62] Ebbens, S.; Tu, M.-H.; Howse, J. R.; Golestanian, R., Size dependence of the propulsion velocity for catalytic Janus-sphere swimmers. *Physical Review E* **2012,** *85* (2), 020401.
[63] Gao, W.; Pei, A.; Wang, J., Water-driven micromotors. *ACS nano* **2012,** *6* (9), 8432-8438.
[64] Bunea, A.-I.; Pavel, I.-A.; David, S.; Gáspár, S., Modification with hemeproteins increases the diffusive movement of nanorods in dilute hydrogen peroxide solutions. *Chem. Commun.* **2013,** *49* (78), 8803-8805.
[65] Wang, W.; Duan, W.; Sen, A.; Mallouk, T. E., Catalytically powered dynamic assembly of rod-shaped nanomotors and passive tracer particles. *Proc. Natl. Acad. Sci. U. S. A.* **2013,** *110* (44), 17744-9.
[66] Pavel, I. A.; Bunea, A. I.; David, S.; Gáspár, S., Nanorods with Biocatalytically Induced Self - Electrophoresis. *ChemCatChem* **2014,** *6* (3), 866-872.
[67] Dey, K. K.; Zhao, X.; Tansi, B. M.; Mendez-Ortiz, W. J.; Cordova-Figueroa, U. M.; Golestanian, R.; Sen, A., Micromotors Powered by Enzyme Catalysis. *Nano Lett.* **2015,** *15* (12), 8311-5.
[68] Ma, X.; Hahn, K.; Sanchez, S., Catalytic mesoporous Janus nanomotors for active cargo delivery. *J. Am. Chem. Soc.* **2015,** *137* (15), 4976-4979.
[69] Ghosh, S.; Mohajerani, F.; Son, S.; Velegol, D.; Butler, P. J.; Sen, A., Motility of Enzyme-Powered Vesicles. *Nano Lett.* **2019,** *19* (9), 6019-6026.
[70] Abdelmohsen, L. K.; Nijemeisland, M.; Pawar, G. M.; Janssen, G.-J. A.; Nolte, R. J.; van Hest, J. C.; Wilson, D. A., Dynamic loading and unloading of proteins in polymeric stomatocytes: Formation of an enzyme-loaded supramolecular nanomotor. *ACS nano* **2016,** *10* (2), 2652-2660.
[71] Kumar, B. V. V. S. P.; Patil, A. J.; Mann, S., Enzyme-powered motility in buoyant organoclay/DNA protocells. *Nat. Chem.* **2018,** *10* (11), 1154-1163.
[72] Hortelão, A. C.; García-Jimeno, S.; Cano-Sarabia, M.; Patiño, T.; Maspoch, D.; Sanchez, S., LipoBots: Using Liposomal Vesicles as Protective Shell of Urease-Based Nanomotors. *Adv. Funct. Mater.* **2020,** *30* (42).
[73] Wang, W.; Duan, W. T.; Ahmed, S.; Mallouk, T. E.; Sen, A., Small power: Autonomous nano- and micromotors propelled by self-generated gradients. *Nano Today* **2013,** *8* (5), 531-554.

[74] Calvo-Marzal, P.; Sattayasamitsathit, S.; Balasubramanian, S.; Windmiller, J. R.; Dao, C.; Wang, J., Propulsion of nanowire diodes. *Chem. Commun.* **2010,** *46* (10), 1623-1624.

[75] Gao, W.; Sattayasamitsathit, S.; Manesh, K. M.; Weihs, D.; Wang, J., Magnetically Powered Flexible Metal Nanowire Motors. *J. Am. Chem. Soc.* **2010,** *132* (41), 14403-14405.

[76] Jiang, H.-R.; Yoshinaga, N.; Sano, M., Active Motion of a Janus Particle by Self-Thermophoresis in a Defocused Laser Beam. *Phys. Rev. Lett.* **2010,** *105* (26), 268302.

[77] Kadiri, V. M.; Bussi, C.; Holle, A. W.; Son, K.; Kwon, H.; Schütz, G.; Gutierrez, M. G.; Fischer, P., Biocompatible Magnetic Micro- and Nanodevices: Fabrication of FePt Nanopropellers and Cell Transfection. *Adv. Mater.* **2020,** *32* (25), 2001114.

[78] Li, Q.; Li, S.; Zhang, X.; Xu, W.; Han, X., Programmed magnetic manipulation of vesicles into spatially coded prototissue architectures arrays. *Nat. Commun.* **2020,** *11* (1), 232.

[79] Jin, C.; Krüger, C.; Maass, C. C., Chemotaxis and autochemotaxis of self-propelling droplet swimmers. *Proc. Natl. Acad. Sci. U. S. A.* **2017,** *114* (20), 5089.

[80] Izri, Z.; van der Linden, M. N.; Michelin, S.; Dauchot, O., Self-Propulsion of Pure Water Droplets by Spontaneous Marangoni-Stress-Driven Motion. *Phys. Rev. Lett.* **2014,** *113* (24), 248302.

[81] Maass, C. C.; Krüger, C.; Herminghaus, S.; Bahr, C., Swimming Droplets. *Annual Review of Condensed Matter Physics* **2016,** *7* (1), 171-193.

[82] van der Weijden, A.; Winkens, M.; Schoenmakers, S. M. C.; Huck, W. T. S.; Korevaar, P. A., Autonomous mesoscale positioning emerging from myelin filament self-organization and Marangoni flows. *Nat. Commun.* **2020,** *11* (1), 4800.

[83] Babu, D.; Scanes, R. J. H.; Plamont, R.; Ryabchun, A.; Lancia, F.; Kudernac, T.; Fletcher, S. P.; Katsonis, N., Acceleration of lipid reproduction by emergence of microscopic motion. *Nat. Commun.* **2021,** *12* (1), 2959.

[84] Manjare, M.; Yang, F.; Qiao, R.; Zhao, Y., Marangoni Flow Induced Collective Motion of Catalytic Micromotors. *J. Phys. Chem. C* **2015,** *119* (51), 28361-28367.

[85] Zhao, G.; Pumera, M., Marangoni self-propelled capsules in a maze: pollutants 'sense and act' in complex channel environments. *Lab Chip* **2014,** *14* (15), 2818-2823.

[86] Golestanian, R.; Liverpool, T. B.; Ajdari, A., Propulsion of a molecular machine by asymmetric distribution of reaction products. *Phys. Rev. Lett.* **2005,** *94* (22), 220801.

[87] Golestanian, R.; Liverpool, T.; Ajdari, A., Designing phoretic micro-and nano-swimmers. *New J. Phys.* **2007,** *9* (5), 126.

[88] Howse, J. R.; Jones, R. A.; Ryan, A. J.; Gough, T.; Vafabakhsh, R.; Golestanian, R., Self-motile colloidal particles: from directed propulsion to random walk. *Phys. Rev. Lett.* **2007,** *99* (4), 048102.

[89] Nijs, B.; Blaaderen, A.; Roeland, J.; van Hest, J. C., Fuel concentration dependent movement of supramolecular catalytic nanomotors. *Nanoscale* **2013,** *5* (4), 1315-1318.

[90] Tu, Y.; Peng, F.; Sui, X.; Men, Y.; White, P. B.; van Hest, J. C. M.; Wilson, D. A., Self-propelled supramolecular nanomotors with temperature-responsive speed regulation. *Nat. Chem.* **2017,** *9* (5), 480-486.

[91] Joseph, A.; Contini, C.; Cecchin, D.; Nyberg, S.; Ruiz-Perez, L.; Gaitzsch, J.; Fullstone, G.; Tian, X.; Azizi, J.; Preston, J.; Volpe, G.; Battaglia, G., Chemotactic synthetic vesicles: Design and applications in blood-brain barrier crossing. *Sci. Adv.* **2017,** *3* (8), e1700362.

[92] Santiago, I.; Simmel, F. C., Self-Propulsion Strategies for Artificial Cell-Like Compartments. *Nanomaterials* **2019,** *9* (12), 1680.

[93] Jarrell, K. F.; McBride, M. J., The surprisingly diverse ways that prokaryotes move. *Nat. Rev. Microbiol.* **2008,** *6* (6), 466-76.

[94] Wang, L.; Lin, Y.; Zhou, Y.; Xie, H.; Song, J.; Li, M.; Huang, Y.; Huang, X.; Mann, S., Autonomic Behaviors in Lipase-Active Oil Droplets. *Angew. Chem., Int. Ed.* **2019,** *58* (4), 1067-1071.

[95] Inaba, H.; Uemura, A.; Morishita, K.; Kohiki, T.; Shigenaga, A.; Otaka, A.; Matsuura, K., Light-induced propulsion of a giant liposome driven by peptide nanofibre growth. *Scientific Reports* **2018,** *8* (1), 6243.

CHAPTER 2

Assembly and characterization of coacervate-based micromotors

Abstract

Over the past decade, various life-like functionalities and biomimetic processes, ranging from *in vitro* transcription-translation to cell budding and division, have been incorporated into synthetic cells. However, imitating cellular motility has been much less explored. In part, this is due to the lack of structural similarity between natural and synthetic systems, and the difficulty of integrating motion mechanisms in cell-mimetic systems. In this chapter, we report on the bottom-up construction and engineering of a synthetic cell based micromotor, namely, a coacervate microdroplet cloaked with a polymer membrane. The chemical versatility of such membrane allows for the conjugation of catalytic units (i.e. enzymes), which are able to transduce chemical energy into motion. Moreover, this polymeric membrane is fluidic, able to translocate transiently and randomly, allowing enzymes to freely diffuse laterally, giving rise to transient morphological heterogeneity. This leads to transient asymmetry in catalyst positioning, causing self-propulsion upon addition of fuel.

This chapter is adapted from the publication: Song, S.; Mason, A. F.; Post, R. A. J.; De Corato, M.; Mestre, R.; Yewdall, N. A.; Cao, S.; van der Hofstad, R. W.; Sanchez, S.; Abdelmohsen, L. K. E. A.; van Hest, J. C. M., Engineering transient dynamics of artificial cells by stochastic distribution of enzymes. *Nat. Commun.* **2021,** *12* (1), 6897.

2.1 Introduction

Natural cells are sophisticated membrane-bound units that comprise the fundamental molecules and functions that keep organisms alive.[1-2] Research in the area of synthetic cells (or protocell models) focuses on shedding light on prebiotic forms of early life, especially towards understanding the structure, function and their evolutionary process.[3] Although it is impossible to know how exactly life emerged, creating synthetic cells with life-like features is a first step in the direction to understand the prerequisites that would have enabled complex molecular systems to evolve in a living entity. For this purpose a wide range of representative synthetic cell models have been created, based on, for example, liposomes,[4] polymersomes [5] and proteinosomes[6]. Among these promising candidates, there has been a surge in the application of liquid-liquid phase separated materials (i.e. coacervates) as synthetic cell platforms due to their remarkable ability to strongly sequester functional materials and their resemblance to the crowded microenvironment found in the cell's cytoplasm. One common type of coacervate compartments are membrane-free microdroplets, formed through the interaction between oppositely charged polyionic (macro)molecules. A membrane-less coacervate was reported by Oparin as a prebiotic protocell model and a basic metabolic unit resembling those formed on the early earth before the formation of membranes.[7] However, the coacervates' membrane-less nature renders them a rudimentary form of protocells, which limits the resemblance to eukaryotic cells.[3, 8] Their lack of a boundary can result in rapid coalescence and poor temporal stability. Such coacervate systems are also sensitive to variations in ionic strength and they easily dissociate at sufficiently high salt concentration. To overcome this complication, a semipermeable membrane-stabilized coacervate was developed in our group,[9] which involves self-assembly of a polymer membrane on the surface of a coacervate microdroplet. The coacervate core was first assembled from oppositely charged amylose derivatives, and was subsequently stabilized by the addition of a block terpolymer, comprised of a hydrophilic poly(ethylene glycol) (PEG) segment, a hydrophobic poly(caprolactone-gradient-trimethylene carbonate) (PCL-*g*-PTMC) domain and a negatively charged poly(glutamic acid) (PGlu) unit for anchoring onto the net positively charged coacervate core (PEG-*b*-PCL-*g*-PTMC-*b*-PGlu). Several life-like functions have been achieved with this polymer-stabilised coacervate system, such as mimicry of cellular compartmentalization,[10] spatial organization of bioactive components[11] and interaction with living cells.[12] The

coacervate core has been extensively studied,[13] however, the unique features of the polymeric membrane remain underexplored.

In this chapter, we aim to equip the above-mentioned polymer-stabilized coacervate system with higher-order functionality; namely, motility – an essential behaviour of living systems across different length scales. Such motile function is crucial for cells and organisms to survive in complex environments. The introduction of motile features in synthetic cell systems allows us to deepen our understanding of motion on the microscale, which could be potentially applied to a wide range of fields, such as drug delivery and soft nano robotics. To translate cell-like motility to an active artificial motor system, a robust platform should be created that is able to change its properties while retaining its integrity. This requirement could be fulfilled by the physicochemical engineering of the aforementioned polymer-stabilized coacervate system. To this end, we embarked on the bottom-up engineering of motile coacervate-based synthetic cells that are equipped with a fluidic polymeric membrane and surface-attached laterally diffusive enzymes. The lateral diffusion should lead to dynamic asymmetry of enzyme distribution, which could be applied to induce motility in presence of fuel, as will be discussed in Chapter 3. In this chapter, we describe methodologies to control the size and topology of the coacervate system and thoroughly study the dynamics of the polymeric membrane.

2.2 Assembly and size control of polymer-stabilized coacervates

Previously, our group demonstrated that a triblock polymer, poly(ethylene glycol)-*b*-poly(ε-caprolactone)-*g*-poly(trimethylene carbonate)-*b*-poly(glutamic acid) (PEG-*b*-PCL-*g*-PTMC-*b*-PGlu), can stabilize a coacervate system,[14] composed of two oppositely charged amyloses. The synthesis of PEG_{44}- *b*-PCL_{50}-*g*-$PTMC_{50}$-*b*-$PGlu_8$ was carried out in four main steps: A ring-opening polymerization of ε-caprolactone and trimethylene carbonate was performed with monomethoxy-PEG-OH macroinitiator, aiming for a composition of PEG_{44}-PCL_{50}-$PTMC_{50}$.[15] This was followed by a carbodiimide-mediated esterification between PEG-PCL-PTMC and Boc-L-phenylalanine (Boc-L-Phe), and deprotection of the Boc group with trifluoro acetic acid (TFA) to introduce a terminal amine onto the diblock copolymer. The primary amine was used as initiator for the ring-opening polymerization of the *N*-carboxyanhydride γ-benzyl-L-glutamate (NCA-BLG), which after hydrogenation of the purified product to remove the benzyl-protecting group, yielded the final terpolymer with an oligo(glutamate block) (this step was

performed by Dr. Alexander Mason). The composition of the resulting terpolymer was confirmed using ^{1}H NMR spectroscopy (**Figure S2-1**).

To assemble polymer-stabilized coacervates, electrostatic interaction was employed: the complex coacervate core was first assembled from two amylose derivatives, quaternary amine modified amylose (Q-Am) and carboxymethyl modified amylose (Cm-Am) in 2:1 molar ratio. These two amylose derivatives are oppositely charged, and the 2:1 molar ratio resulted in an overall positively charged coacervate core. The subsequent addition of the PEG-*b*-PCL-*g*-PTMC-*b*-PGlu terpolymer with a negatively charged poly(glutamic acid) segment facilitated the stabilization of the whole system via electrostatic interaction (**Figure 2-1**).

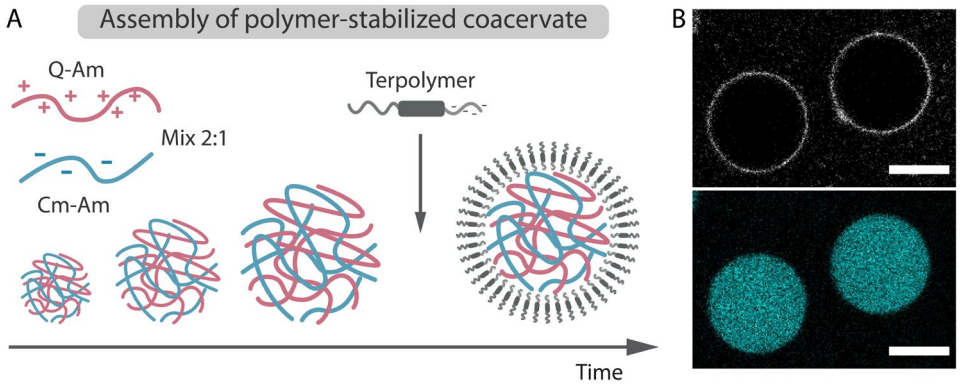

Figure 2-1 | **A.** Schematic illustration of hierarchical assembly of polymer-stabilized coacervates. First, oppositely charged modified amyloses (Q-Am and Cm-Am) are mixed in a 2:1 molar ratio, immediately forming complex coacervate microdroplets that coalesce and increase in size over time. This growth is arrested by the addition of a carefully designed block terpolymer, PEG-PCL-PTMC-PGlu, which self-assembles on the surface of coacervate microdroplets. **B.** Confocal images of polymer-stabilized coacervates. Grey: Nile red in the polymeric membrane; Cyan: Atto 488 labelled BSA, added as cargo to the coacervates. Scale bar represents 10 µm.

The size of a micromotor has a great impact on its motion dynamics, therefore it is important to control the size during assembly of the coacervates. To this end, three methods were developed. First, the size of the coacervate droplets was controlled during their formation, by halting the growth of the coacervates by adding stabilizing terpolymer at different time points after the start of the coacervation process.[14] However, this process has as main drawback that there is a lower limit of size (about 6 µm in diameter). To further downsize coacervates, firstly the volume of amylose solutions was varied. We observed the overall tendency that size decreased as the volume decreased. 1 unit volume (1V)

denotes 200 µL Q-Am and 100 µL Cm-Am. As volume decreased from 1V to 0.2V (40 µL Q-Am and 20 µL Cm-Am), the diameter of the coacervates decreased from 10.3 ± 3.4 to 2.57 ± 0.71 µm, as shown in **Figure 2-2** (Dye Atto 488 labelled BSA was encapsulated in the coacervates for image analysis, see Experimental section for details). A significant drop in size was observed from 0.5V to 0.4V, where the size declined from 9.34 ± 2.57 µm to 3.10 ± 1.29 µm. Although intuitively one would expect no relationship between the solution volume and coacervation process (i.e. coacervate size), our results could be attributed to potential change in shear stress that takes place during the mixing process, which is performed in an Eppendorf shaker under continuous shaking conditions (See Experimental section). Indeed, previous investigations demonstrated the impact of shear stress and Reynolds number (shear stress is a function of Reynolds number) on the final complex coacervates' morphology and size. [16-17] Reynolds number (*Re*), a dimensionless value that represents the ratio between inertial and viscous forces, is typically used to indicate the flow state (i.e., laminar or turbulent) and consequent shear stress of fluid flow. *Re* is defined as $Re = \frac{\rho v d}{\mu}$, where ρ is the fluid density, v the flow speed, μ the viscosity of fluid and d the characteristic dimension. In our case, the shaking speed was constant amongst all samples, but the different volumes (ranging from 60 µL for 0.2V to 300 µL for 1V) with the same shaking speed are expected to lead to variations in the Reynolds number, specifically the characteristic dimension *d*. Several studies demonstrated that under shaking conditions (as compared to stirring conditions) the Reynolds number had a more complex form and non-linearly increased with filling volume in one sample vessel.[18-19] Such relation between volume and *Re* can explain the observed decrease in coacervate size.

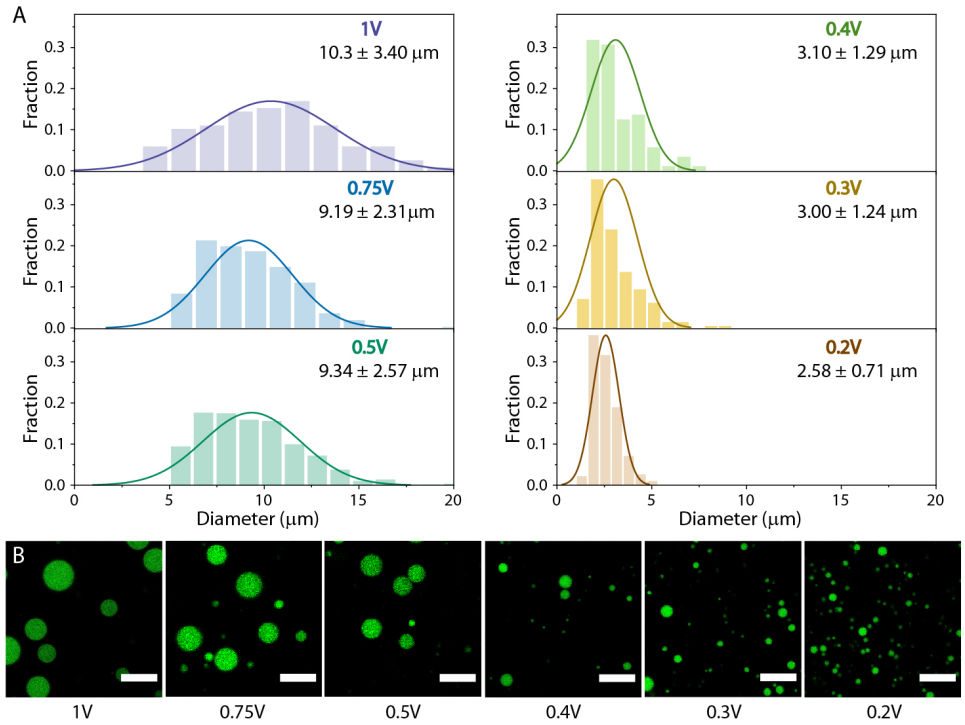

Figure 2-2 | Controlling the size of coacervates via the applied volume of amylose derivative solutions. 1V denotes 200 µL Q-Am and 100 µL CM-Am, and terpolymer was added after 1 min of growth time. **A.** Histogram charts were obtained by analyzing at least 100 coacervates for each volume using confocal microscopy. **B.** Representative confocal images of each size group (Green: Atto 488 labelled BSA). Scale bar represents 20 µm.

In order to construct coacervates with a diameter of less than 2 µm, the following ultrasonication method was developed. Eppendorf tubes containing amylose solutions were placed in an ultrasonic bath instead of an Eppendorf shaker used in the previous methods. With this approach, the diameter of the coacervates was reduced to ca. 1.2 µm (**Figure 2-3**). Interestingly, the coacervate growth time had in this case a minor influence on the size, as only slight differences in size were observed when terpolymer was added after 1.5, 3 or 5 min.

Finally, we applied mechanical extrusion as a methodology to reduce the coacervate size. Extrusion is a common technique used to produce homogenous nano-sized liposomes. Coacervates were filtered using a mini-extruder with a pore size of 1 µm. Surprisingly, this did not result in size reduction, and, on the contrary, an overall decrease in coacervate number was observed, evident from bright-field and confocal images

(**Figure S2-2**). Such decrease in number could be attributed to the adhesion of the polymeric membrane onto the filter, leading to their disruption and disassociation.

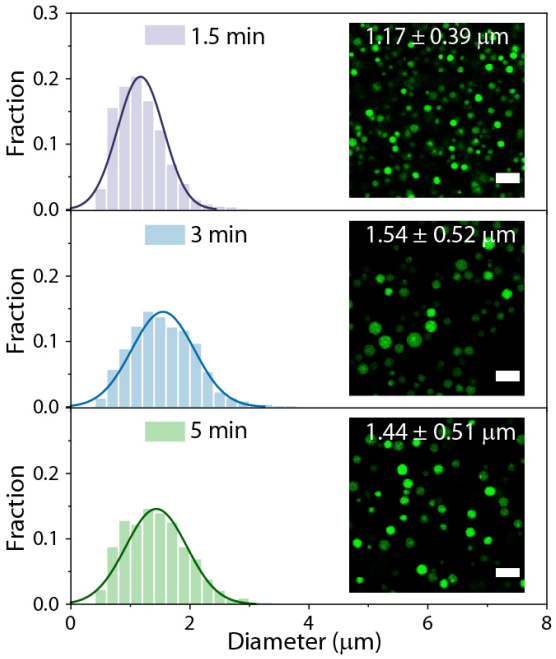

Figure 2-3 | Size of coacervates is significantly reduced with the ultrasonication method. Coacervate growth time does not have a significant effect on the size. Scale bar represents 5 µm. Histogram charts were obtained by including at least 280 coacervates per condition.

2.3 Surface attachment of enzymes as propulsive units

To equip our coacervate system with motility, propulsive (catalytic) units had to be installed. Therefore, two enzymes, catalase (CAT) and urease (UR), were selected as the propulsive units due to their frequently reported use as catalytic engines able to propel micron and nano-sized particles in the presence of hydrogen peroxide or urea, respectively.[20-22] The attachment of these enzymes to the coacervate membrane (**Figure 2-4**) was facilitated by the strain-promoted alkyne-azide cycloaddition (SPAAC) reaction. For this purpose, CAT and UR were firstly functionalized with dibenzocyclooctyne (DBCO) and Cyanine5 (Cy5, for visualization under confocal microscopy), generating DBCO-CAT and DBCO-UR. By using a combination of PEG-*b*-PCL-*g*-PTMC-*b*-PGlu terpolymer and an azide-functionalized block polymer, α-azido-poly(ethylene glycol)-*b*-poly(ε-caprolactone-*gradient*-trimethylene carbonate) (composition confirmed by ^{1}H NMR as

shown in **Figure S2-3**), an azido-functionalized polymer membrane was created around the coacervate core. DBCO-CAT (or DBCO-UR) was subsequently added to the azido-coacervate suspension to initiate the conjugation. After 2 hours, unbound enzymes were removed by centrifugation and enzyme-attached coacervates were resuspended in phosphate-buffered saline (PBS).

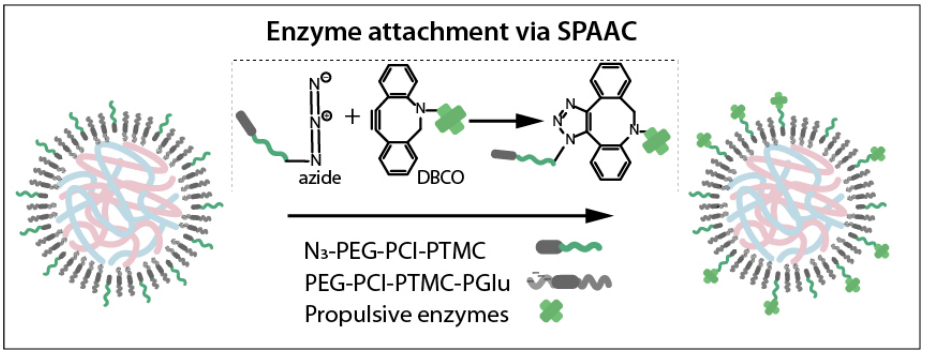

Figure 2-4 | Schematic illustration of DBCO-functionalized enzyme attachment on the azido-containing polymeric membrane via strain-promoted alkyne-azide cycloaddition (SPAAC) click reaction.

To validate the attachment of the enzymes to the coacervate surface, confocal microscopy images were taken, which confirmed the successful enzyme-membrane coupling, manifested as a ring-like distribution of Cy5-labelled CAT (**Figure 2-5**). UR was also successfully attached to the polymeric membrane of coacervates (**Figure S2-4**). Conjugation efficiency (amount of enzymes that were covalently attached on the coacervates compared to amount of enzymes added in the beginning) was obtained by measuring and comparing the fluorescence of dye-labelled enzymes from the supernatant (unbound enzymes) and pellet (enzymes on the membrane). The conjugation efficiencies of CAT/UR attached onto coacervates (d~1.2 μm) are listed in **Table 2-1**.

Table 2-1| Conjugation efficiencies of CAT/UR attached onto coacervates.

Conditions	*Conjugation efficiency / %*
CAT-coacervate (d~1.2 μm)	16.0
UR-coacervate (d~1.2 μm)	14.8

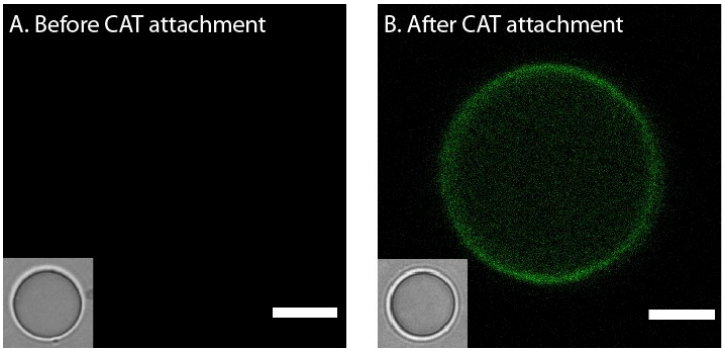

Figure 2-5 | Coacervate functionalization with CAT. Before (**A**) and after (**B**) CAT attachment to the surface of coacervates. A ring structure was seen in **B** indicating surface-localized attachment of enzymes (Green: Cy5 labelled CAT). Inserts are corresponding bright-field images. Scale bar represents 2 μm.

2.4 Fluidic membrane and laterally diffusive enzymes

Previous research from our group indicated that the terpolymer has a glass transition temperature (T_g) below 0 °C,[13] meaning the membrane is fluidic at room temperature. To explore the influence of membrane fluidity on the enzyme distribution, we performed fluorescence recovery after photobleaching (FRAP) experiments on the enzyme-attached coacervates. To monitor the lateral diffusion of surface-attached enzymes, a selected circular area on the membrane was bleached (100% laser intensity), and the fluorescence intensity in the bleached area was monitored (with 1-2% laser intensity) over time. Faster fluorescence recovery in the bleached area indicated faster lateral diffusion of enzymes on the membrane. Image analysis revealed that the fluorescence from CAT recovered after 52 seconds (**Figure 2-6A**). To obtain a quantitative result, the average background fluorescence (Bg) was subtracted from the fluorescence intensity at time t, I(t), and corrected for unintentional photobleaching, which was calculated as

$$I(t) = \frac{ROI(t) - Bg}{Ref(t) - Bg},$$

whereas ROI(t) is the intensity of the bleached area at time t, Ref(t) is the intensity of an unbleached fluorescent area (same size as bleached area) and Bg is the average intensity of a background area. I(t) was further normalized such that pre-bleach intensity was set to 1. This was done by dividing I(t) by the average value of background-subtracted pre-bleach intensity within the bleach area. Normalized intensity $I(t)_{normalized}$ was plotted against time to get the FRAP recovery curve (**Figure 2-6B**). This recovery curve was fitted with $I(t)_{normalized} = B - Ae^{-\tau t}$, assuming exponential kinetics, to obtain parameter τ. In the

above equation, τ is the recovery time constant and A and B are two independent constants. Then, the recovery half-time $\tau_{1/2}$ and apparent diffusion coefficient D_L were calculated from $\tau_{1/2} = - \ln 0.5 / \tau$ and $D_L = 0.88\ \omega^2 / 2\tau_{1/2}$ (for a circular bleaching area), respectively.[23] We obtained a lateral diffusion (D_L) of $3.6 \times 10^{-2} \pm 8.0 \times 10^{-4}$ μm² / s for CAT-coacervates and $3.0 \times 10^{-2} \pm 5.0 \times 10^{-4}$ μm² / s for UR-coacervates (**Figure S2-5**). The results were obtained by measuring at least 6 different enzyme-attached coacervates for each case. Such results confirmed the ability of membrane-bound enzymes to translocate diffusively along the surface. Moreover, the lateral diffusivity of surface-bound UR is very close to that of CAT, as the fluidity of this polymeric membrane instead of enzyme properties probably plays a dominant role in diffusivity of these surface-tethered substances.

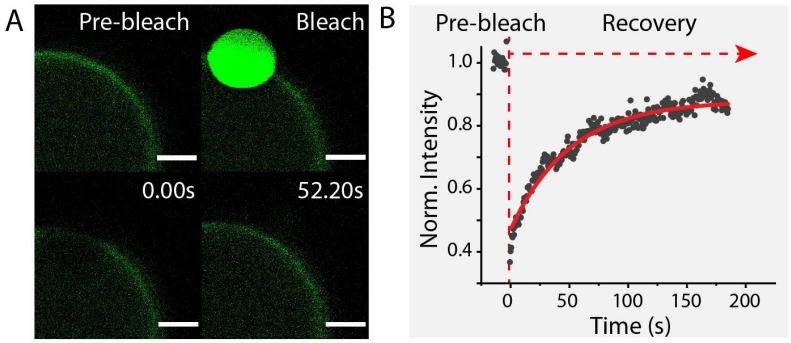

Figure 2-6 | **A.** FRAP measurement showing laser-mediated bleaching of a circular spot on the membrane and subsequent fluorescence recovery of the bleached spot due to Cy5 (green) labelled catalase laterally diffusing along the fluidic membrane. **B.** FRAP recovery curve with black dots representing experimental data and red curve exponential fitting.

2.5 "Freezing" the diffusion of enzymes

Having confirmed the lateral diffusion of enzymes on the surface of the coacervates, we continued to investigate a method that allows tuning of enzyme diffusivity. We envisioned that enzyme diffusion can be "frozen" or slowed down by means of in-situ crosslinking. This was performed by crosslinking of catalase using a chemical crosslinker, namely, glutaraldehyde (GA). In order to avoid unwanted aggregation of catalase, crosslinking was carried out after extensive washing steps to remove any unbound catalase (**Figure 2-7**). FRAP measurements were performed on CAT-coacervates with crosslinked surface enzymes to test the extent of decrease in lateral diffusivity. An evident drop in fluorescence recovery speed was observed, as there was no significant recovery

more than 100 s after bleaching (**Figure 2-8A**), compared to obvious fluorescence recovery after ~52 s in the case of no crosslinking (**Figure 2-6**). Although the enzyme diffusivity was drastically diminished, it is important to note that enzymes were not fully static even after crosslinking, as a slight recovery in intensity was observed (**Figure 2-8B**).

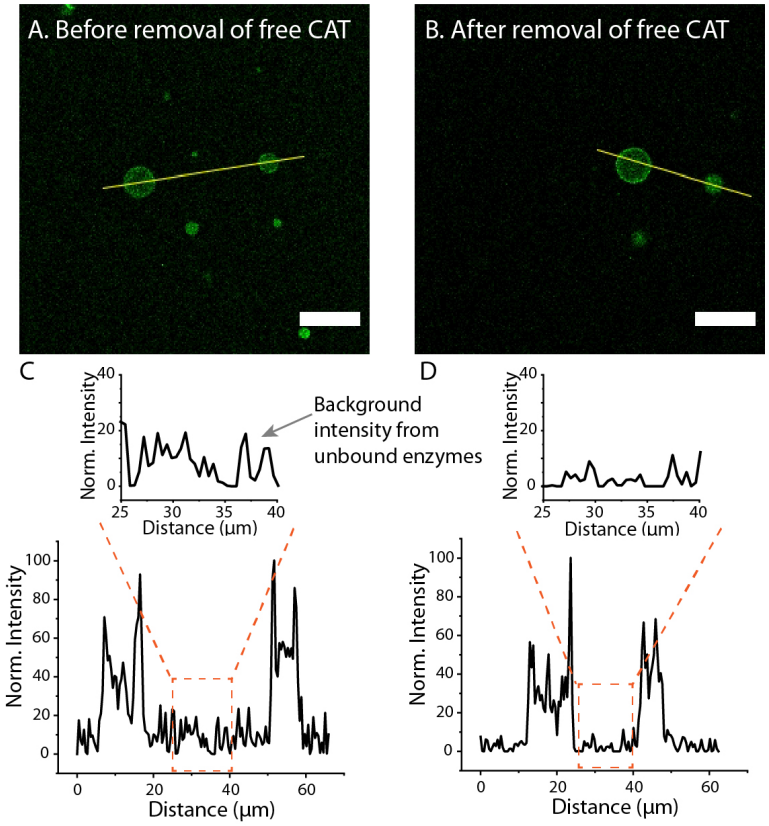

Figure 2-7 | CAT-coacervates before (**A**) and after (**B**) unbound CAT removal by centrifugation and resuspension. Line intensity profiles of corresponding yellow lines in **A** and **B** show that the background fluorescence intensity after unbound CAT removal (**D**) is significantly lower than before (**C**), indicating the effectiveness of said purification. Scale bars represent 20 µm.

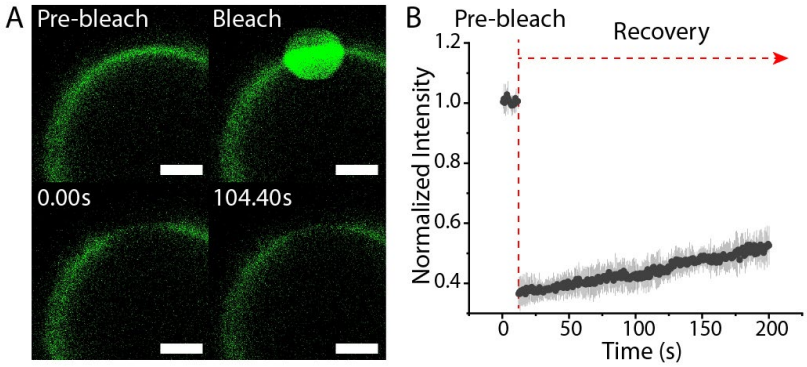

Figure 2-8 | **A.** FRAP measurements confirmed decreased lateral diffusivity of CAT after crosslinking, with no significant recovery in the bleached area even 100 s after bleaching (green: Cy5-CAT). Scale bar represents 2 µm. **B.** The fluorescence recovery curve shows only a slight recovery in intensity, indicating that crosslinked CAT clusters diffuse much more slowly compared to non-crosslinked CAT molecules on the membrane.

2.6 Conclusions

In summary, we constructed a polymer-cloaked coacervate system, which allows control over two key parameters essential for motion; namely size and (chemical) topology. Control over coacervate size with narrow size distribution was attained by two methods based on ultrasonication and amylose volume tuning. Secondly, the chemical versatility of the PEG-*b*-PCL-*g*-PTMC polymer membrane promoted surface modification of the coacervates, by conjugation of enzymes. FRAP measurements confirmed the fluidity of the enzyme-bound polymeric membrane and consequent lateral enzyme diffusivity. Such dynamic membrane generates a system with transient asymmetry. Further in-situ crosslinking of surface enzymes allowed us to tune the enzyme diffusivity, paving the way toward possible modulation of motion dynamics.

Experimental section

Materials

All materials were used as received unless otherwise stated. For the synthesis of polymers: monomethoxy poly(ethylene glycol) (1 and 2 kDa) and azido-PEG-OH macroinitiator (3 kDa) were purchased from Rapp Polymere, trimethylene carbonate was purchased from TCI Europe. For the preparation of modified amylose derivatives: amylose (12-16 kDa) was supplied by Carbosynth and 3-chloro-2-hydroxypropyltrimethyl ammonium chloride (65 wt% in water) was supplied by TCI Europe. Catalase (from bovine liver), urease (Jack bean), dibenzocyclooctyne-PEG4-maleimide (DBCO-PEG4-mal), dibenzocyclooctyne-NHS ester (DBCO-NHS), 30% hydrogen peroxide solution, Atto 488-NHS ester were obtained from Sigma-Aldrich. Sulfo-Cyanine5 NHS ester was obtained from Lumiprobe. 3-Azido-7-hydroxycoumarin was obtained from Baseclick GmbH. Hydrogen peroxide solutions used for motility experiments were prepared by sequential dilutions of 30% hydrogen peroxide solution.

Synthesis of polymers

Synthesis of poly(ethylene glycol)-b-poly(ε-caprolactone)-g-poly(trimethylene carbonate)-b-poly(glutamic acid) (PEG_{44}- b-PCL_{50}-g-$PTMC_{50}$-b-$PGlu_8$) terpolymer

Step 1 - Preparation of poly(ethylene glycol)-poly(ε-caprolactone-gradient-trimethylene carbonate) (PEG-PCl-PTMC). According to a modified literature procedure, the organocatalyzed ring-opening polymerization of ε-caprolactone and trimethylene carbonate was performed, aiming for a composition of PEG_{44}-PCL_{50}-g-TMC_{50}.[15] Monomethoxy-PEG-OH macroinitiator (2 kDa, 0.2 mmol, 400 mg) was weighed into a round-bottomed flask along with ε-caprolactone (ε-CL, 10 mmol, 1108 µL) and trimethylene carbonate (TMC, 10 mmol, 1121 mg) and dried via azeotropic evaporation of added toluene (x3). The dried reagents were then re-dissolved in dry toluene (20 mL) and methanesulfonic acid (0.6 mmol, 39 µL) was added, under argon. The reaction mixture was stirred at 30 °C for 6 h, after which the product was precipitated into ice-cold methanol. This yielded 2.1 g of a waxy solid (85 % yield) and the composition of the resulting copolymer was confirmed by ^{1}H NMR (**Figure S2-1**), comparing the protons of PEG (3.65-3.7 ppm), terminal methyl unit (singlet at 3.40 ppm) to PCL CH_2 (multiplet at 2.40-2.25 ppm) and PTMC CH_2 (multiplet at 2.2-1.8 ppm). GPC analysis (using a PL gel 5 µm mixed D column, with THF as eluent and PS standards) yielded a Đ of 1.1.

Step 2 - Chain-end modification with Boc-L-phenylalanine and deprotection. For the incorporation of a terminal amine onto the diblock copolymer, we performed a carbodiimide-mediated esterification between PEG-PCL-PTMC and Boc-L-phenylalanine (Boc-L-Phe). 1.3 g (ca. 0.1 mmol) of PEG-PCL-PTMC copolymer was dissolved in acetonitrile and to it was added *N,N'*-dicyclohexylcarbodiimide (0.2 mmol, 41.9 mg), Boc-L-Phe (0.5 mmol, 23.4 mg), and 4-dimethylaminopyridine (0.02 mmol, 2.5 mg) on ice. The reaction mixture was stirred for 24 h at RT and afterwards placed directly in the freezer overnight to facilitate precipitation of dicyclohexylurea by-product. After cold filtration of the reaction mixture, it was concentrated and then precipitated into cold methanol. ^{1}H NMR spectroscopy was used to verify the product and to confirm disappearance of the terminal TMC signal at 1.92 ppm due to addition of phenylalanine at the terminus, and emergence of aromatic protons at around 7.2-7.3 ppm and Boc protons at 1.45 ppm, before deprotection. The resulting copolymer was then dissolved in 5 mL DCM, to which 5 mL of trifluoro acetic acid (TFA) was added (on ice) and the mixture was allowed to warm to RT

whilst stirring for 2 h. After 2 h the solvent was evaporated and the copolymer was washed with $NaHCO_3$, 1 M NaCl and brine before drying on $MgSO_4$, filtration and evaporation of the majority of the solvent so that the copolymer could be precipitated into ice-cold methanol. ^1H NMR clearly showed that the signal arising from the Boc group had disappeared. GPC analysis before and after deprotection yielded a Đ of 1.1, indicating that TFA treatment did not induce copolymer hydrolysis.

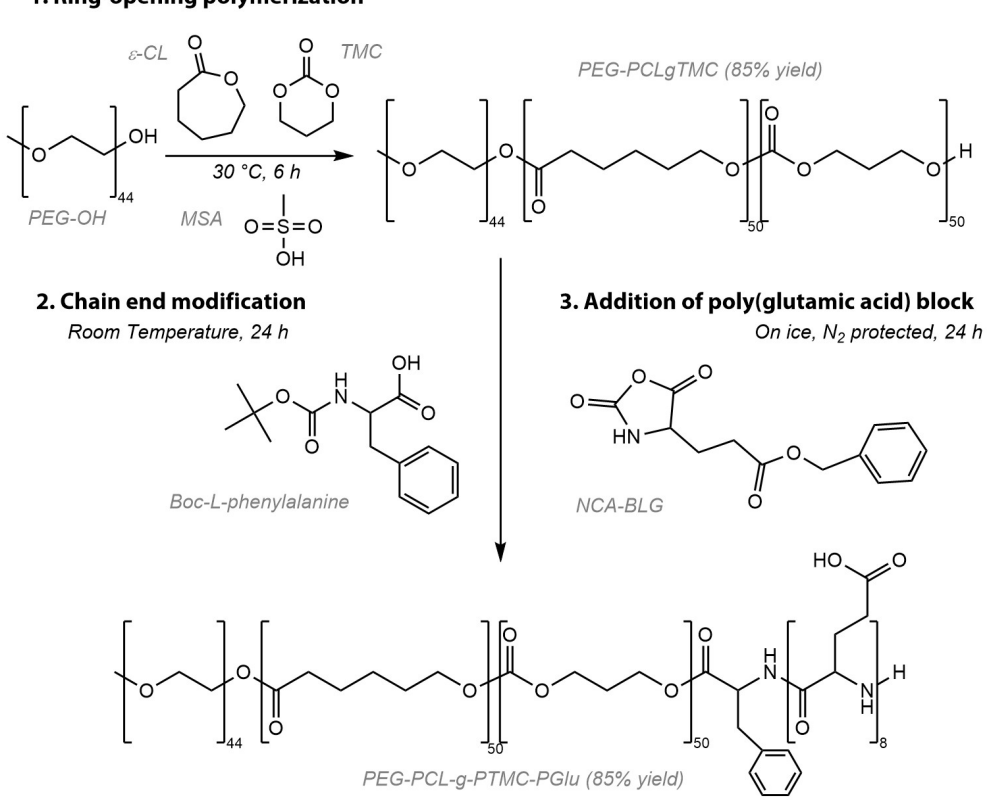

Scheme S1: Synthesis of PEG_{44}-*b*-PCL_{50}-*g*-$PTMC_{50}$-b-$PGlu_8$ terpolymer. Poly(ethylene glycol)$_{44}$ monomethyl ether was used to initiate the ring opening polymerisation of ε-caprolactone and trimethylene carbonate (step 1). The terminal alcohol of this polymer was subsequently modified via a Steglich esterification with Boc-L-Phe-OH to yield a primary amine after TFA deprotection (step 2). The final poly(L-glutamic acid) block was introduced by the ring opening polymerization of *N*-carboxyanhydride γ-benzyl-L-glutamate, followed by hydrogenation (step 3).

Step 3 - Polymerization and deprotection of *N*-carboxyanhydride γ-benzyl-L-glutamate (NCA-BLG) (performed by Dr. Alexander Mason). Following a published method for the controlled polymerization of NCA-BLG by lowering the temperature and maintaining a constant flow of N_2 in order to remove CO_2 by-product,[24] we aimed to add between 8 and 10 BLG units onto the amine-terminus of the copolymer chains. 1 g of Phe-terminated copolymer was weighed into a Schlenk flask and dissolved with ca. 3 mL of dry DMF and cooled in an ice bath. To the cooled mixture 160 mg of NCA-BLG was added under Ar and the reaction was left under a constant flow of N_2 for 24 h. The product was precipitated into cold methanol

and analysed by ^{1}H NMR to confirm the overall composition and, in particular, the presence of benzylic and aromatic protons at 5.0-5.2 and 7.1-7.4 ppm, respectively. Benzyl-protected terpolymer was dissolved in 10 mL THF and 10 mL methanol was added before applying hydrogenation using the H-Cube at 60 °C with 30 bars of H_2 pressure and a flow rate of 1 mL/min to facilitate removal of the benzyl protecting groups. The product was concentrated, then precipitated into cold ether, and dissolved in dioxane before lyophilisation to yield a waxy solid, 0.9 g (85 % yield). ^{1}H NMR was used to confirm successful deprotection of the BLG units, and GPC data indicated that the polydispersity did not increase beyond 1.1 during this process.

Synthesis of azido-poly(ethylene glycol)-b-poly(ε-caprolactone)-g-poly(trimethylene carbonate) (azido-PEG$_{68}$-b-PCL50-g-PTMC$_{50}$) block copolymers (azido-pol)

This synthesis was performed by Dr. Shoupeng Cao. The synthesis protocol was modified from a literature procedure.[15] First, azido-PEG-OH macroinitiator (3 kDa, 0.1 mmol, 300 mg) was weighed into a round bottom flask along ε- CL (5 mmol, 553 µL) and TMC (5 mmol, 510 mg) and dried via azeotropic evaporation of added toluene (x3). The dried reagents were then re-dissolved in dry DCM (10 mL) and dry methanesulfonic acid (0.2 mmol, 14 µL) was added under argon. The reaction was stirred at 30 °C overnight, after which there was no sign of unreacted monomers, as confirmed by ^{1}H NMR. After the reaction was finished, the solution was concentrated and copolymer precipitated into ice cold MeOH (x2), followed by dissolution in dioxane and lyophilization to yield 1.01 g of a waxy solid (78% yield). Copolymer composition was ascertained from the ^{1}H NMR spectrum in the same manner as for step 1 of the terpolymer synthesis above. GPC analysis (using a PL gel 5 µm mixed D column, with THF as eluent and PS standards) yielded Mn = 15.7 kDa, Đ = 1.12. Copolymer composition was confirmed by ^{1}H NMR (**Figure S2-3**).

Modification of enzymes

Catalase modification: Cy5-DBCO-Catalase

Catalase was modified with Cy5 and DBCO as follows: 20 mg (0.08 µmol) catalase was dissolved in 2.5 mL 0.1 M sodium bicarbonate buffer (adjusted to pH = 8.2) in a glass vial, to which 125 µL of an aqueous solution of sulfo-Cy5-NHS ester (4 mg/mL, 5.1 mM) was added. This 8:1 (dye: protein) stoichiometry was chosen to ensure sufficient dye labeling as the NHS ester is easily hydrolyzed. The mixture was covered with aluminum foil and stirred overnight at 4°C and then dialyzed for 24 hours against 1x PBS buffer. Cy5 labeled catalase was purified via fast protein liquid chromatography (FPLC, BioRad NGC system). DBCO-PEG4-mal was dissolved in PBS (1 mg/mL, 1.5 mM) by vigorous vortexing and sonication and added into the Cy5-catalase solution. The reaction was carried out overnight by gentle stirring at 4°C. The obtained CAT was purified by FPLC. The concentration was determined to be 2.3 mg/mL (9.3 µM) by Nanodrop analysis. The Cy5 labelling number per catalase tetramer was determined to be 2 and DBCO (absorption peak at 310 nm) labelling number per catalase tetramer was determined to be 1 by Nanodrop analysis.

Urease modification: Cy5-DBCO-Urease

Urease was modified with Sulfo-Cy5-NHS ester and DBCO-NHS ester as follows: 100 mg (0.18 µmol) urease was dissolved in 10 mL 0.1 M sodium bicarbonate buffer (adjusted to pH = 8.2) in a glass vial, to which 1.14 mg (1.47 µmol) sulfo-Cy5-NHS ester powder and 0.3 mg (0.73 µmol) DBCO-NHS ester (in DMSO) were added. The excess of NHS ester was to ensure sufficient dye labeling as it is easily hydrolyzed. The mixture

was covered with aluminum foil and stirred overnight at 4°C and then dialyzed for 24 hours against 1x PBS buffer. The obtained UR was then purified with FPLC. The concentration was determined to be 3.7 mg/mL (6.7 μM) by Nanodrop analysis. The Cy5 labelling number per urease was determined to be 1.4 and DBCO (absorption peak at 310 nm) labelling number per catalase tetramer was determined to be 0.5 by Nanodrop analysis.

Bovine serum albumin modification

Bovine serum albumin (BSA) was succinylated and modified with the Atto 488 dye as follows: 5 mg BSA was dissolved in 2.5 mL 100 mM $NaHCO_3$ (adjusted to pH 9) in a 1.5 mL Eppendorf tube (BSA concentration 2.5 mg/mL), to which 20 μL Atto 488-NHS ester (10 mM, in DMSO) was subsequently added. The reaction mixture was gently stirred at room temperature overnight. The next day, succinic anhydride was added directly to the reaction mixture at a final concentration of 50 mM. The reaction mixture was gently stirred under aluminum foil for another 4 hours before purification by FPLC and the concentration was determined to be approximately 1.2 mg/mL. Atto 488 labeling number per BSA was determined to be 1.2 by UV-Vis spectroscopy.

Catalase activity assay before and after modification

The activity of Cy5-DBCO-CAT was determined by measuring the decomposition of hydrogen peroxide over time via UV-Vis spectroscopy (JASCO V-650). In these assays, 0.1 mL of diluted catalase (unmodified, 5 μg/mL or modified, 6.9 μg/mL) in PBS solution was mixed with 2.9 mL hydrogen peroxide solution (0.036 wt% in water), and the characteristic absorbance at 240 nm (A_{240}) was monitored over time. Enzyme activity was calculated according to:

$$\text{Units/mL enzyme} = \frac{3.45 \times df}{time \times 0.1},$$

where 3.45 corresponds to the decomposition of 3.45 μmoles of hydrogen peroxide in a 3.0 ml reaction mixture producing a decrease in the A_{240} from 0.45 to 0.40, *df* is the dilution factor and *time* (minutes) is the time for A_{240} to decrease from 0.45 to 0.40. Enzyme activities of unmodified catalase and modified catalase were determined after 3 individual measurements to be about 10×10^3 U/mg and 5×10^3 U/mg, respectively. Unit (U) is defined as: one unit of catalase will decompose 1.0 μmole of H_2O_2 per minute at pH 7.0 at 25 °C.[25]

Urease activity assay before and after modification

Urease activity was tested by measuring the pH change in solution upon addition of its substrate urea. First the pH of the urease solution was adjusted to around 4.0 by HCl addition, then urea was added and the pH change over time was recorded. Ten minutes after urea addition, the pH recording stopped. Urease activity before and after modification were both tested. The urease (before modification, as purchased from Sigma-Aldrich) has an enzyme activity about 30000 units/g solid. After modification, urease kept about 74% activity according to:

$$\text{Relative activity} = \frac{\Delta pH\ (urease\ after\ modification)}{\Delta pH\ (urease\ before\ modification)}.$$

One micromolar unit will produce 1.0 μmole of NH_3 from urea per min at pH 7.0 at 25 °C.

Assembly of polymer-stabilized coacervates

Volume tuning method using Eppendorf shaker

To 200 µL 0.5 mg/mL quaternized amylose (Q-Am) solution in an Eppendorf tube was added 100 µL 0.5 mg/mL carboxymethyl amylose (Cm-Am) solution to induce coacervation. The mixture was placed in an Eppendorf shaker (ThermoMixer) at 1500 rpm for 1 minute to allow the coacervate growth, followed by addition of 10 µL 50 mg/mL terpolymer mixture in PEG 350 to generate a polymeric membrane and stabilize the coacervate core. The final concentration of coacervate suspension was 0.32 mg/mL in Q-Am.

1 unit volume (1V) denotes 200 µL Q-Am and 100 µL Cm-Am. For other volumes, corresponding amounts of amylose solutions and polymer solution were added to form coacervates. For example, 100 µL Q-Am, 50 µL Cm-Am and 5 µL polymer mixture were used to form 0.5V coacervates.

Ultrasonication method

The amylose mixture was placed in an ultrasonication bath instead of an Eppendorf shaker. Other steps are the same as the volume tuning method.

Extrusion method

Mini-extruder from Avanti was used to perform extrusion of coacervates. A filter with a pore size of 1 µm was pre-wet by 1x PBS and secured on the filter support, followed by assembly of extruder. Coacervate suspension obtained from volume tuning method was filled in a gas-tight glass syringe. This filled syringe and another empty syringe were inserted into the extruder stand. The plunger of the filled syringe was gently pushed until the coacervate suspension was completely transferred to the alternate syringe. 5 pushes were conducted in total to make 10 passes of through the filter.

Coacervates for image analysis

To facilitate size analysis, succinylated Atto 488 labelled bovine serum albumin (BSA) was loaded in the interior of the coacervates. To assemble BSA loaded coacervates, after addition of Cm-Am, 10 µL BSA was added to the amylose mixture, followed by a proper growth time and addition of the membrane-forming terpolymer.

Coacervates for enzyme surface attachment

A polymer mixture (20%v/v 50 mg/mL azido-PEG_{68}-b-PCL_{50}-g-$PTMC_{50}$ and 80%v/v 50 mg/mL terpolymer in PEG 350) was used to make coacervates with an azide-functional membrane for enzyme attachment. Other steps were the same as described above.

Surface attachment of CAT and UR to coacervate surface

After the assembly of coacervates, 46 µg (2.3 mg/mL, 20 µL) of CAT (Cy5-DBCO-Catalase) or 54 µg (3.7 mg/mL, 14.5 µL) UR (Cy5-DBCO-Urease) were added to 0.32 mg/mL 300 µL coacervate suspension to allow enzyme attachment on the polymeric membrane through strain-promoted azide–alkyne cycloaddition (SPAAC) between the azido-group installed on the polymer membrane and the DBCO moiety introduced in the enzyme. The reaction was carried out for two hours, followed by separation of unbound enzymes by centrifugation and refreshing the supernatant with 1x PBS.

Conjugation efficiency was obtained by measuring and comparing the fluorescence of dye-labelled enzymes from the supernatant (unbound enzymes) and pellet (enzymes on the membrane). First, CAT-/UR-coacervates were centrifugated (800×G, 5 min) to obtain supernatant containing unbound enzymes and pellet containing enzyme-attached coacervates, followed by resuspension of pellet with 1× PBS. The

fluorescence from the supernatant and resuspended pellet were subsequently measured by a plate reader (triplicate samples). Conjugation efficiency was calculated as follows:

$$\text{Conjugation efficiency (\%)} = \frac{I_{p,avg}}{I_{p,avg} + I_{s,avg}} \times 100,$$

where $I_{p,avg}$ is average fluorescence intensity of the pellet and $I_{s,avg}$ average fluorescence intensity of the supernatant.

Enzyme activity test after surface attachment via SPAAC reaction

Catalase activity after surface attachment was tested qualitatively. After surface attachment and removal of unbound catalase via centrifugation, 0.2 mL 5 wt% H_2O_2 was added to 0.2 mL 0.32 mg/mL CAT-coacervate suspension in PBS buffer, and generation of a large amount of oxygen bubbles was observed, which confirmed catalase was still sufficiently active after surface attachment.

In situ crosslinking of CAT on the polymeric membrane

After CAT-coacervate fabrication, 109 µL of glutaraldehyde in 1x PBS (GA, 275 mM) and 91 µL of 1x PBS were added to 100 µL 0.32 mg/mL CAT-coacervate suspension. The final concentration of GA was 100 mM. The reaction was carried out for 3 hours at room temperature with mild stirring. Unreacted GA was removed by centrifugation and resuspension of the coacervates twice in 1x PBS.

Supporting Information

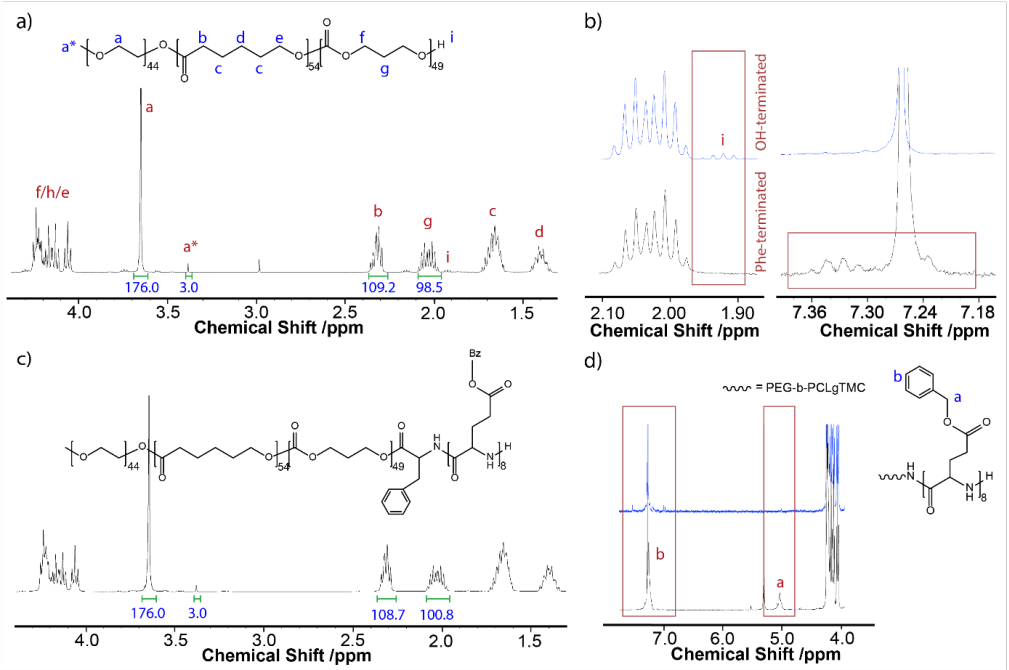

Figure S2-1 | ^{1}H NMR analysis of terpolymer synthesis. (a) analysis of PEG-PCLgPTMC, (b) demonstration of the complete chain-end modification of PEG-PCLgPTMC with Boc-L-Phe, (c) analysis of the product of ring opening polymerization of BLG-NCA and (d) specific evaluation of PBLG content of the resulting terpolymer using benzylic and aromatic protons at 5.0-5.2 and 7.1-7.4 ppm, with upper spectrum showing successful deprotection by hydrogenation.

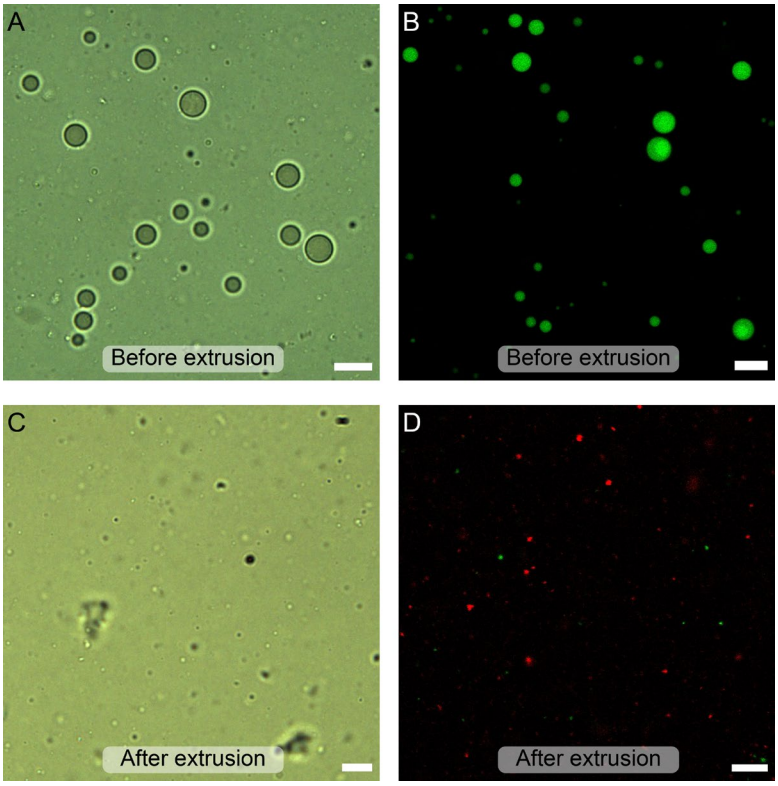

Figure S2-2 | Coacervates analyzed before and after filtration with a micro-extruder. **A, B.** Bright-field and confocal images of coacervates before extrusion. Green: Atto488-labeled BSA encapsulated in the core of coacervates. Scale bar represents 10 µm. **C, D.** Bright-field and confocal images of coacervates after extrusion. Red: Nile Red in the membrane of coacervates. Scale bar represents 5 µm. It is clear from the confocal image (D) that coacervate cores were dissociated from the polymer membrane.

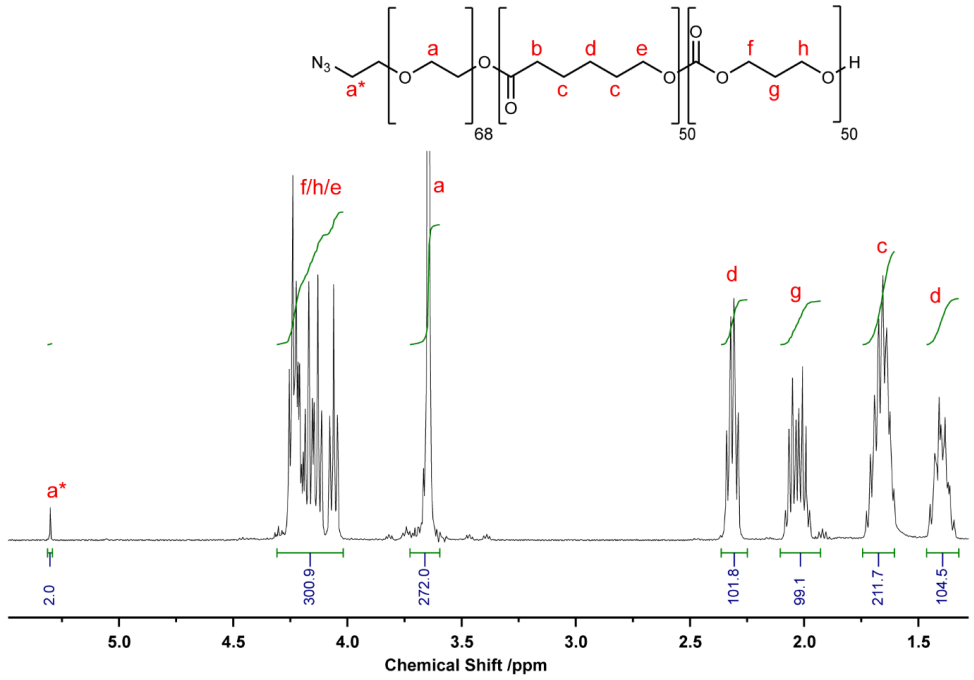

Figure S2-3 | ^{1}H NMR analysis of azido-PEG$_{68}$-b-PCL$_{50}$-g-PTMC$_{50}$. This spectrum confirms M_n by comparing the integrals of the PEG block to the new PCL and PTMC blocks, and the retention of azido functionality (a*).

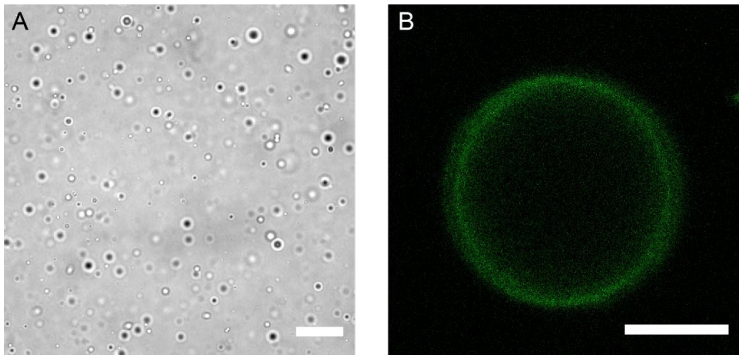

Figure S2-4 | Bright field (A) and confocal image (B) of UR-coacervates. The ring-like structure in (B) confirms the successful enzyme-membrane coupling. Scale bars represent 20 µm (A) and 5 µm (B).

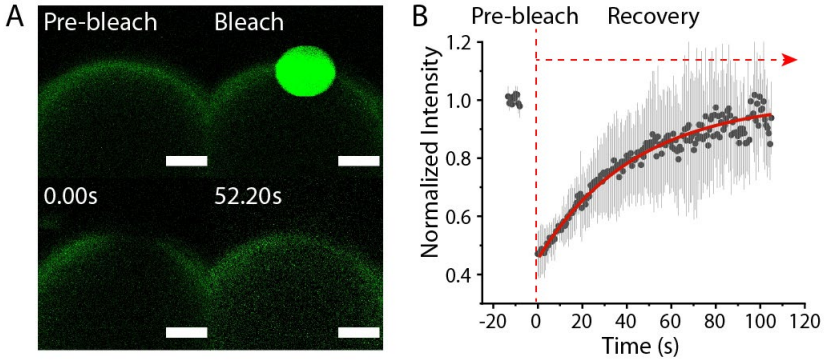

Figure S2-5 | FRAP measurements were performed on UR-coacervates to test the lateral diffusivity of urease. (A) Substantial recovery 52.2 seconds after laser bleaching was observed (Green: Cy5 from CAT). (B) FRAP recovery curve with black dots representing experimental data and red curve exponential fitting. Lateral diffusivity of surface-bound UR was determined to be around 0.03 $\mu m^2/s$. Scale bar represents 2 µm.

Acknowledgements

Dr. Alexander Mason and Dr. Amy Yewdall are thanked for their collaboration. Dr. Alexander Mason is additionally thanked for guidance in terpolymer synthesis. Dr. Shoupeng Cao is thanked for providing the azido-functionalized polymer. Dr. Bastiaan Buddingh', Wiggert Altenburg and Marleen van Stevendaal are kindly acknowledged for useful tips and discussions.

References

[1] Bayley, H.; Wu, L.-F.; Sutherland, J. D.; Le Vay, K.; Mutschler, H.; Berger, I.; Tölzer, C.; Gupta, K.; Evanoff, M.; Komor, A. C., Building blocks for cells and tissues: Beyond a game. *Emerging Top. Life Sci.* **2019,** *3*, 433-434.

[2] Yeh Martín, N.; Valer, L.; Mansy, S. S., Toward long-lasting artificial cells that better mimic natural living cells. *Emerging Top. Life Sci.* **2019,** *3* (5), 597-607.

[3] Mason, A. F.; van Hest, J. C., Multifaceted cell mimicry in coacervate-based synthetic cells. *Emerging Top. Life Sci.* **2019,** *3* (5), 567-571.

[4] Rideau, E.; Dimova, R.; Schwille, P.; Wurm, F. R.; Landfester, K., Liposomes and polymersomes: a comparative review towards cell mimicking. *Chem. Soc. Rev.* **2018,** *47* (23), 8572-8610.

[5] Mason, A. F.; Thordarson, P., Polymersomes as protocellular constructs. *J. Polym. Sci., Part A: Polym. Chem.* **2017,** *55* (23), 3817-3825.

[6] Li, M.; Huang, X.; Tang, T.-Y. D.; Mann, S., Synthetic cellularity based on non-lipid micro-compartments and protocell models. *Curr. Opin. Chem. Biol.* **2014,** *22*, 1-11.

[7] Kolb, V. M., *Handbook of Astrobiology*. CRC Press: 2018.

[8] Yewdall, N. A.; Mason, A. F.; van Hest, J. C. M., The hallmarks of living systems: towards creating artificial cells. *Interface Focus* **2018,** *8* (5), 20180023.

[9] Mason, A. F.; Buddingh', B. C.; Williams, D. S.; van Hest, J. C. M., Hierarchical Self-Assembly of a Copolymer-Stabilized Coacervate Protocell. *J. Am. Chem. Soc.* **2017,** *139* (48), 17309-17312.

[10] Mason, A. F.; Yewdall, N. A.; Welzen, P. L.; Shao, J.; van Stevendaal, M.; van Hest, J. C.; Williams, D. S.; Abdelmohsen, L. K., Mimicking Cellular Compartmentalization in a Hierarchical Protocell through Spontaneous Spatial Organization. *ACS Cent. Sci.* **2019,** *5* (8), 1360-1365.

[11] Altenburg, W. J.; Yewdall, N. A.; Vervoort, D. F. M.; van Stevendaal, M. H. M. E.; Mason, A. F.; van Hest, J. C. M., Programmed spatial organization of biomacromolecules into discrete, coacervate-based protocells. *Nat. Commun.* **2020,** *11* (1), 6282.

[12] van Stevendaal, M. H. M. E.; Vasiukas, L.; Yewdall, N. A.; Mason, A. F.; van Hest, J. C. M., Engineering of Biocompatible Coacervate-Based Synthetic Cells. *ACS Appl. Mater. Interfaces* **2021,** *13* (7), 7879-7889.

[13] Yewdall, N. A.; Buddingh, B. C.; Altenburg, W. J.; Timmermans, S.; Vervoort, D. F. M.; Abdelmohsen, L.; Mason, A. F.; van Hest, J. C. M., Physicochemical Characterization of Polymer-Stabilized Coacervate Protocells. *ChemBioChem* **2019,** *20* (20), 2643-2652.

[14] Mason, A. F.; Buddingh', B. C.; Williams, D. S.; van Hest, J. C., Hierarchical self-assembly of a copolymer-stabilized coacervate protocell. *J. Am. Chem. Soc.* **2017,** *139* (48), 17309-17312.

[15] Couffin, A.; Delcroix, D.; Martín-Vaca, B.; Bourissou, D.; Navarro, C., Mild and efficient preparation of block and gradient copolymers by methanesulfonic acid catalyzed ring-opening polymerization of caprolactone and trimethylene carbonate. *Macromolecules* **2013,** *46* (11), 4354-4360.

[16] Lemetter, C. Y. G.; Meeuse, F. M.; Zuidam, N. J., Control of the morphology and the size of complex coacervate microcapsules during scale-up. *AIChE Journal* **2009,** *55* (6), 1487-1496.

[17] Lemos, Y. P.; Mariano Marfil, P. H.; Nicoletti, V. R., Particle size characteristics of buriti oil microcapsules produced by gelatin-sodium alginate complex coacervation: Effect of stirring speed. *International Journal of Food Properties* **2017,** *20* (sup2), 1438-1447.

[18] Büchs, J.; Lotter, S.; Milbradt, C., Out-of-phase operating conditions, a hitherto unknown phenomenon in shaking bioreactors. *Biochemical Engineering Journal* **2001,** *7* (2), 135-141.

[19] Dürauer, A.; Hobiger, S.; Walther, C.; Jungbauer, A., Mixing at the microscale: Power input in shaken microtiter plates. *Biotechnology Journal* **2016,** *11* (12), 1539-1549.

[20] Arqué, X.; Romero-Rivera, A.; Feixas, F.; Patiño, T.; Osuna, S.; Sánchez, S., Intrinsic enzymatic properties modulate the self-propulsion of micromotors. *Nat. Commun.* **2019,** *10* (1), 2826.

[21] Patiño, T.; Feiner-Gracia, N.; Arqué, X.; Miguel-López, A.; Jannasch, A.; Stumpp, T.; Schäffer, E.; Albertazzi, L.; Sanchez, S., Influence of enzyme quantity and distribution on the self-propulsion of non-Janus urease powered micromotors. *J. Am. Chem. Soc.* **2018,** *140* (25), 7896-7903.

[22] Kumar, B. V. V. S. P.; Patil, A. J.; Mann, S., Enzyme-powered motility in buoyant organoclay/DNA protocells. *Nat. Chem.* **2018,** *10* (11), 1154-1163.

[23] Axelrod, D.; Koppel, D.; Schlessinger, J.; Elson, E.; Webb, W. W., Mobility measurement by analysis of fluorescence photobleaching recovery kinetics. *Biophys. J.* **1976,** *16* (9), 1055-1069.

[24] Zou, J.; Fan, J.; He, X.; Zhang, S.; Wang, H.; Wooley, K. L., A facile glovebox-free strategy to significantly accelerate the syntheses of well-defined polypeptides by N-carboxyanhydride (NCA) ring opening polymerizations. *Macromolecules* **2013,** *46* (10), 4223-4226.

[25] Enzymatic Assay of Catalase (EC 1.11.1.6). https://www.sigmaaldrich.com/NL/en/technical-documents/protocol/protein-biology/enzyme-activity-assays/enzymatic-assay-of-catalase.

CHAPTER 3

Engineering coacervate-based motors by stochastic distribution of enzymes

Abstract

Random fluctuations are inherent to all complex molecular systems. Although nature has evolved mechanisms to control stochastic events to achieve the desired biological output, reproducing this in synthetic systems represents a significant challenge. Here we present an artificial platform that enables us to exploit stochasticity to direct motile behavior. We find that enzymes, when confined to the fluidic polymer membrane of a core-shell coacervate, are distributed stochastically in time and space. This results in a transient, asymmetric configuration of propulsive units, which imparts motility to such coacervates in presence of substrate. This mechanism is confirmed by stochastic modelling and simulations in silico. Furthermore, we show that a deeper understanding of the mechanism of stochasticity could be utilized to modulate the motion output. Conceptually, this work represents a leap in design philosophy in the construction of synthetic systems with life-like behaviours.

This chapter is adapted from the publication: Song, S.; Mason, A. F.; Post, R. A. J.; De Corato, M.; Mestre, R.; Yewdall, N. A.; Cao, S.; van der Hofstad, R. W.; Sanchez, S.; Abdelmohsen, L. K. E. A.; van Hest, J. C. M., Engineering transient dynamics of artificial cells by stochastic distribution of enzymes. *Nat. Commun.* **2021,** *12* (1), 6897.

3.1 Introduction

Underlying the macroscopic behaviour of living organisms are a plethora of transient processes comprising nano/microscopic supramolecular systems. At this length scale, random thermal fluctuations can have significant consequences on the macroscopic outcome. Stochastic events that occur in an ever-fluctuating biological environment play an important role in directing complex cellular processes. In order to provide a robust response to varying input, nature has developed a range of approaches to translate stochasticity into adaptive biological output. Specific examples include the dampening of cellular noise to stabilize stochastic decisions in neuronal cell development[1] and the autonomous motion of motor proteins,[2-3] a consequence of fluctuating biochemical reactions.

Self-propulsion, as a consequence of transducing chemical energy into kinetic energy, is an intrinsically recognizable biological behaviour that requires a number of dynamic and internally regulated processes. For example, motion observed in cells is a consequence of the constant remodelling of the tubulin-based cytoskeleton, where constructive and deconstructive processes are working in concert under control of, amongst others, fluctuations in GTP concentration.[4] While a number of synthetic systems are capable of autonomous motion at length scales similar to those observed in biology,[5-9] they do not rival the natural ones in terms of dynamic complexity. This overarching challenge can be overcome by exploiting inherently dynamic systems (i.e., systems with stochastic/random properties) for motion.

Stochasticity is of course not only present in biological systems. Stochastic processes have been observed in many synthetic systems as well, and have been used to interpret their specific behaviour. For example, in the field of active systems, the stochastic positioning of propulsive units has been used as an explanation for the observed non-Brownian behaviour (e.g. motility). Specific examples include the stochastic attachment in a fixed position of enzymes to the surface of nanoparticles by Sanchez et al.,[10] and the conjugation of enzymes to the fluid membrane of liposomes by Sen et al.[11] However, in contrast to nature, stochasticity has not yet been used in active motor systems, or any other synthetic systems, as a purposely introduced component to control the system's features. In order to incorporate more life-like behaviour in active matter, stochasticity should be given a more prominent role.

In this chapter, we describe a micromotor system in which we have been able to include stochasticity as a design element. Our micromotor is based on the coacervate

microdroplet cloaked with a fluidic polymer membrane, as described in Chapter 2. To this membrane, enzymes are conjugated as propulsive units. Moreover, as this membrane is fluid at room temperature,[12-13] the continuous spatiotemporal reorganization of such propulsive units is ensured. As such, we hypothesize that this transient asymmetry will lead to a variety of random, continuously changing organizational states, with a fraction of these displaying sufficient polarization to generate an instantaneous net propulsion capable of actively propelling the coacervates. This mechanistic hypothesis has been validated experimentally and *in silico*. We have also identified important parameters for the modulation of these molecular fluctuations, namely, enzyme density and lateral diffusivity, which impact the motility output. Importantly, theoretical simulations further confirm our hypothesis that a stochastic process governs the motile behaviour.

3.2 Design and rationale of coacervate-based micromotors

Morphological asymmetry (e.g., motor shape, catalyst distribution) is a prerequisite for autonomous motion.[14-17] Asymmetry can be imposed on the motor through its external environment (e.g., concentration gradient) or in the motor structure itself (e.g., shape). This has been achieved by, for example, the construction of Janus particles, which are hemi-spherically covered with active catalysts.[9, 18-21] Marangoni stress has also been employed as a propulsion force in surfactant-stabilised liquid droplet systems,[22-28] which can be achieved by modification of surfactant layers and consequent spontaneous symmetry-breaking of droplet interfaces. Recently, a random surface distribution of enzymes has been shown to propel micromotors in the presence of fuel.[10] This inspired us to construct a system, in which asymmetry (i.e. heterogeneous distribution of enzymes) is transient and dynamic, enabled by the inherent fluidity of a polymer membrane (**Figure 3-1D, E**). This approach is in contrast to other investigations that employ static and fixed surface distribution of catalysts (**Figure 3-1B, C**). Our platform is composed of a complex coacervate droplet stabilized by a terpolymer membrane, as described in Chapter 2. The chemical nature of the membrane made it possible to securely tether enzymes (catalase CAT and urease UR) to the surface (Chapter 2). Due to the experimentally validated membrane fluidity and enzyme diffusivity, the enzyme organization on the surface continuously changed. During the course of time-lapse confocal imaging, a highly punctate, dynamic radial distribution of CAT was observed (**Figure 3-2**), confirming our hypothesis that the fluidic polymer membrane results in dynamic enzyme clustering and hence a transient asymmetrical distribution of propulsive units. With this unique design,

we proposed that a fraction of these transient asymmetrical organizations of propulsive enzymes would generate sufficient polarization and lead to self-propulsion of coacervates in presence of fuel (**Figure 3-1A**).

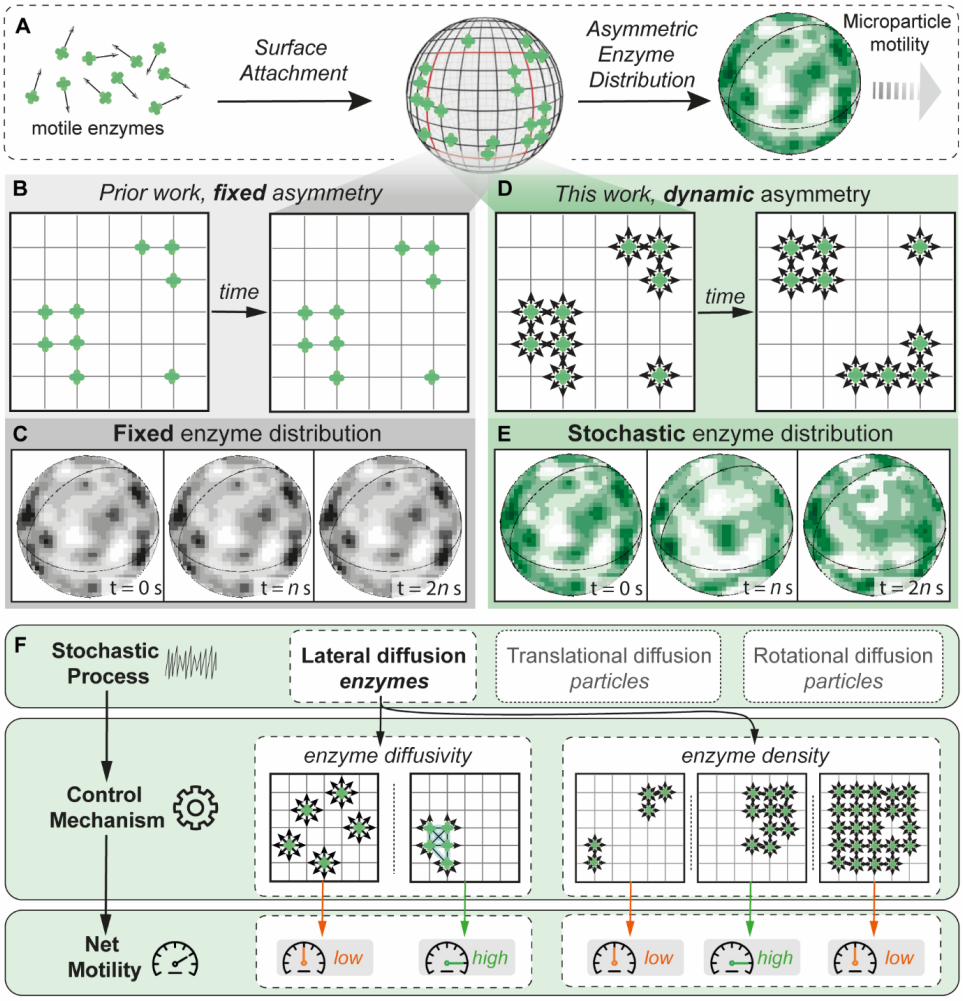

Figure 3-1 | Design philosophy to translate a stochastic process into autonomous motion in an artificial system. **A.** Coacervates with surface-confined enzymes and consequent transient asymmetry, leading to autonomous motility of coacervates in the presence of fuel. Schematic outlining the difference between static (**B, C**) and dynamic (**D, E**) structural asymmetry. Static asymmetry with fixed enzyme distribution does not change with time (**C**), while dynamic asymmetry features a spatiotemporally stochastic enzyme distribution (**E**). **F.** Stochasticity can be utilized for modulating the motion output via tuning either the lifetime of the transient asymmetry (enzyme diffusivity) or the organizational states of enzyme distribution (enzyme density).

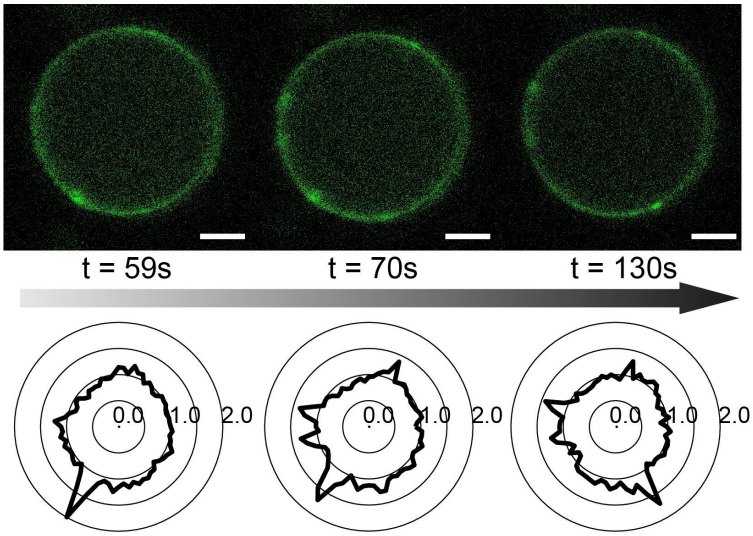

Figure 3-2 | Confocal images taken at different time points (upper row) of one single enzyme-functionalized coacervate, with brighter spots along the ring suggesting catalase enzyme clustering. Bottom row displays corresponding intensity radial plots with spikes representing higher local intensity. A radial number of 1.0 indicates evenly distributed enzymes, while a radial number > 1.0 indicates higher local enzyme density (enzyme clustering). Scale bar represents 2 μm.

3.3 Motility of coacervate-based micromotors

Having confirmed the transient asymmetry on the coacervate membrane, we set out to test coacervate motility. Motion of CAT- and UR-coacervates was recorded in the presence or absence of their respective substrate by bright-field microscopy. Coacervates with a diameter of 1.2 ± 0.4 μm (assembly of differently sized coacervates was discussed in Chapter 2) were chosen for motility experiments due to their small size and their ability to exhibit Brownian motion, which facilitates their autonomous motion (in the presence of fuel) and decreases the chance of sedimentation, compared to their larger counterparts. The coacervate suspension and their corresponding substrate (hydrogen peroxide or urea) were first mixed thoroughly and immediately added to the experimental chamber. The recording started shortly after. Videos were recorded at 25 FPS and for a period of 30–35 s. For each condition, 15-20 coacervates were analysed. For CAT-coacervates, the hydrogen peroxide concentration after mixing was set to 10 mM. This rather low concentration was chosen to avoid oxygen bubble generation that could disturb the liquid inside the chamber and mask self-propulsion. CAT- or UR-coacervate suspensions

in the experimental chamber were generally replaced every 3 minutes to maintain a constant substrate concentration.

The motility of both CAT- and UR-coacervates was analysed using a tailor-made Python script,[29-30] where X and Y trajectory data were extracted and the mean square displacement (MSD) was calculated. MSD is a measure of deviation of the position of a particle with respect to its initial position over time. It is commonly used to analyse motion dynamics of self-propelled particles and is calculated in 2D projection using the following equation:

$$MSD\ (t) = \langle(\vec{x}(t) - \vec{x}\ (0))^2\rangle, \tag{1}$$

where $\vec{x}(0)$ is the initial position of the coacervate, and $\vec{x}(t)$ is the position of the coacervate when time is *t*. One well-known solution of the MSD equation (1) is:

$$MSD = 4D_T\Delta t + V^2\Delta t^2, \tag{2a}$$

at shorter timescale ($\Delta t \ll \tau_R$), giving a curved MSD vs. Δt plot, and

$$MSD = (4D_T + V^2\tau_R)\Delta t\ =\ 4D_{eff}\Delta t, \tag{2b}$$

at longer timescale ($\Delta t \gg \tau_R$), which is similar to the case of Brownian motion but with the enhanced diffusion coefficient D_{eff}. $D_T = \frac{k_BT}{6\pi\eta R}$ is the translational diffusion coefficient, $D_R = \frac{k_BT}{8\pi\eta R^3}$ is the rotational diffusion coefficient of the coacervate, k_BT represents the thermal energy, η is the viscosity of the liquid suspending the particle and *R* is the radius of the coacervate. $\tau_R = D_R^{-1}$ and is the characteristic timescale that determines the transition from the ballistic regime at short timescales to the diffusive regime at long timescales.[31-32] The direction of self-propulsion randomizes over long timescales ($\Delta t \gg \tau_R$) because of the intrinsic rotation of the micro-sized coacervate motors, leading to crossover from propulsive behaviour to enhanced diffusion.

In the absence of fuel, both CAT- and UR-coacervates, with a diameter of 1.2 μm and medium density enzyme coverage (discussed in Section 3.4), exhibited typical Brownian motion, with linear MSD fitting profiles (**Figure 3-3D, E** and **Figure S3-1**). Upon addition of fuel, 10 mM H_2O_2 or 500 mM urea (final concentration) respectively, enhanced propulsion with significant increase in MSD profiles was observed for both CAT- and UR-coacervates (**Figure 3-3D, E**). Moreover, individual trajectories (**Figure 3-3B, C**) showed significant path expansion after fuel addition, confirming coacervate propulsion in the presence of fuel, without the need for deliberate structural or externally manipulated asymmetric features.

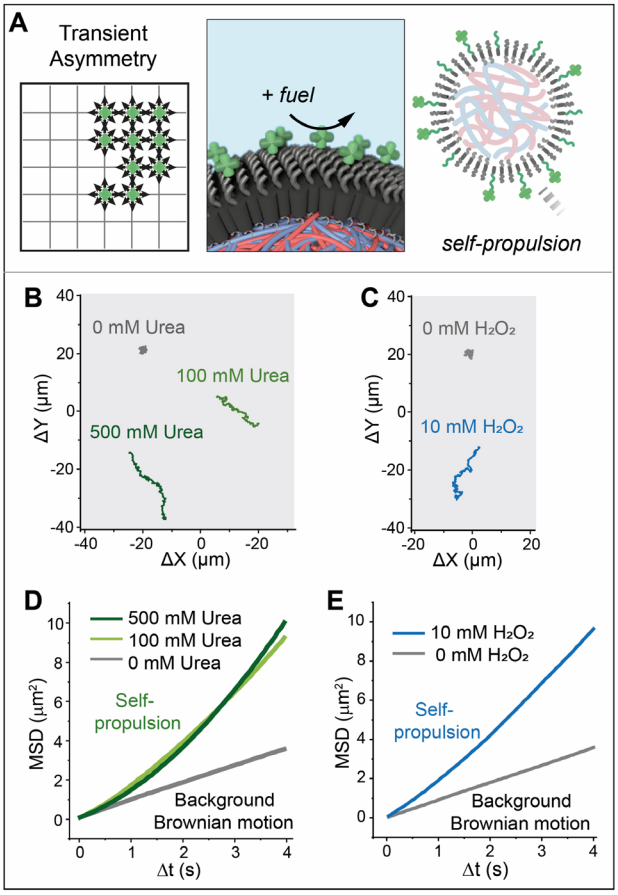

Figure 3-3 | Motility observed in enzyme-tethered coacervates: experimental data. **A.** Schematic illustration of transient asymmetry inducing enzyme-powered self-propulsion. **B.** Representative trajectories of UR-coacervates (diameter~1.2 μm) over 15 s with 500 mM, 100 mM and 0 mM urea respectively. **C.** Representative trajectories of CAT-coacervates (diameter~1.2 μm) with 10 mM and 0 mM H_2O_2 respectively. **D.** MSD curves of UR-coacervates with 500 mM, 100 mM and 0 mM urea. **E.** MSD curves of CAT-coacervates with 10 mM and 0 mM H_2O_2. MSD curves (D, E) with error bars (mean ± SEM) are available in **Figure S3-1**.

3.4 Tuning motion dynamics by varying enzyme density

An important parameter that influences the degree of asymmetry in the system, and hence the motile output, is the coverage of enzymes (proportional to number/density of enzymes) on the surface of the coacervates. We set out to test the impact of enzyme density on motility by fabricating both CAT- and UR-coacervates with three different surface enzyme densities - low, medium and high. For CAT-coacervates, low, medium and

high surface densities were formed by the addition of 4.6, 46, and 81 μg CAT to 300 μL coacervates (0.32 mg/mL in Q-Am) after coacervate formation. For UR-coacervates, these amounts were 5.4, 54, and108 μg UR respectively. After purification, unbound enzymes were removed. To quantify the actual enzyme density on the coacervate surface, we first calculated the number of coacervates at a given volume, and then determined, using Cy5-labeled enzymes, the total amount of attached enzymes via fluorescence spectroscopy. To estimate the coacervate number, we first measured the density of the interior coacervate phase. The coacervate phase was generated by mixing 6 mL of 3 mg/mL Q-Am and 3 mL of 3 mg/mL Cm-Am for 5 min (no stabilizing polymer was added). Subsequent centrifugation led to macroscopic phase separation, and supernatant was removed. 10 μL pellet (coacervate phase) weighed 10.5 μg, therefore the density of the coacervate phase was determined to be 1050 mg/mL. As the mass of Q-Am and Cm-Am and density of the coacervate phase are known, the total volume of all coacervates was calculated according to $V_{total} = \frac{m_{Q-Am}+m_{Cm-Am}}{density_{coacervate}}$. The average volume ($V_{avg}$) of one coacervate was calculated from the average diameter of the coacervate (obtained from confocal image analysis, see Chapter 2). By dividing V_{total} over V_{avg}, the number of coacervates was calculated. Results are listed in **Table 3-1**.

Table 3-1 | Number of Coacervates per mL with different sizes.

Diameter of coacervates (μm)	Number of coacervates / mL
10.3	800×10^3
3.6	29×10^6
1.2	510×10^6

The total amount of CAT or UR attached on the coacervates was estimated through Cy5 fluorescence emission (for enzyme modification, see Chapter 2). Enzyme-coacervates were centrifugated into a pellet, while unbound enzymes stayed in the supernatant. After removing the supernatant, the pellet was resuspended in PBS buffer. Cy5 fluorescence emission from the supernatant and resuspended pellet were measured by a plate reader (TECAN Spark 10M). The percentage of enzymes attached was calculated by $\frac{\text{Cy5 emission in pellet}}{\text{Cy5 emission in pellet + Cy5 emission in supernatant}}$. Then, this percentage and the total number of coacervates obtained above (**Table 3-1**) were used to calculate the average number of enzyme molecules attached to one coacervate. The enzyme coverage on the coacervate

surface was obtained using the previously reported diameters of catalase[33] and urease[34], which are 5 nm and 7 nm, respectively (**Table 3-2**).

Table 3-2 | Number density and surface area coverage of CAT/UR attached on one coacervate. Both CAT- and UR-coacervates have an average diameter of 1.2 ± 0.4 μm.

CAT-coacervate			**UR-coacervate**		
Enzyme density	*Number of CAT /coacervate*	*Coverage of enzyme*	*Enzyme density*	*Number of UR /coacervate*	*Coverage of enzyme*
Low	$6\times10^3 - 8\times10^3$	2 – 3 %	*Low*	$5\times10^3 - 7\times10^3$	2 – 3 %
Medium	$100\times10^3 - 120\times10^3$	43 – 52 %	*Medium*	$40\times10^3 - 50\times10^3$	17 – 22 %
High	$150\times10^3 - 200\times10^3$	65 – 87 %	*High*	$100\times10^3 - 120\times10^3$	43 – 52 %

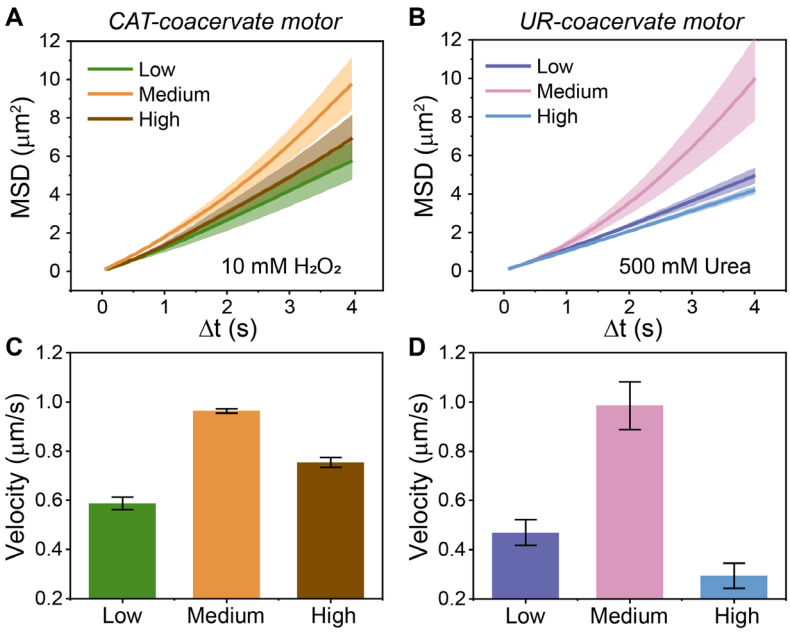

Figure 3-4 | Tuning transient asymmetry by enzyme density varies motion dynamics. **A, B.** MSD curves of CAT-coacervates and UR-coacervates (diameter~1.2 μm) with three different enzyme densities, namely low, medium, high (**Table 3-2**). Data are presented as mean ± SEM. **C, D.** The corresponding velocity derived from MSD curves fitting. 18 coacervates were analysed per condition for CAT-coacervates and 17 coacervates were analysed per condition for UR-coacervates.

Indeed, in presence of their respective fuels, 10 mM H_2O_2 and 500 mM urea, CAT and UR-coacervates, with different enzyme densities and same average size (diameter~1.2 μm), moved with different MSDs and velocities (**Figure 3-4**). Surprisingly, coacervates with

medium enzyme density moved faster than those with high and low densities, contrary to the monotonic increasing trend one would expect. In addition, the velocity (obtained from MSD curves fitted with Equation 2a) of coacervates with high enzyme density was close to those with low enzyme density (**Figure 3-4C, D**).

To investigate the mechanism behind the nonmonotonic trend of enzyme density and motility, we first ruled out local substrate depletion as the reason for high enzyme density coacervates yielding diminished propulsion. We estimated the relative rate of the enzymatic reaction versus substrate diffusion by calculating the Damköhler number:

$$\mathrm{Da} = \frac{\dot{r}\ R}{d\ c_{sub}} \tag{3}$$

where $\dot{r}$ is the reaction rate, R is the radius of the coacervate, d is the diffusion coefficient of the substrate and c_{sub} is the concentration of the substrate far from the coacervate. The reaction rate $\dot{r}$ can be estimated as the product of the maximum turnover rate k_{cat} of the enzyme multiplied by the surface density of the enzymes Γ_0: $\dot{r} \approx k_{cat}\Gamma_0$. We estimated surface density of the enzymes in the case of maximum packing (100% enzyme coverage):

$$\Gamma_0 \approx \frac{0.91}{\pi {r_{enz}}^2} \tag{4}$$

where r_{enz} is the characteristic size of the enzyme.

Da of 0.13 and $4.5{\cdot}10^{-4}$ were obtained for CAT- and UR-coacervates respectively (**Table 3-3**). In both cases, the Damköhler number is smaller than 1 even with the overestimated full coverage of the surface with enzymes (experimental enzyme coverage is up to 87%, see **Table 3-2**). This means that diffusion is faster than the reaction rate and substrate molecules can be resupplied as soon as they react, implying no local substrate depletion.

Table 3-3 | Parameters used for estimation of the Damköhler number.

	CAT-coacervate	UR-coacervate
R (μm)	0.60	0.60
Substrate	Hydrogen peroxide	Urea
d ($\times 10^{-9}$ m^2/s)	0.90*	1.30*
c_{sub} (mM)	10	100
c_{sub} (number of molecule/m^3)	6.022×10^{24}	6.022×10^{25}
r_{enz} (nm)	5*	7*
k_{cat} (s^{-1})	1.00×10^5	1.00×10^4
Da	0.13	0.00045

*Data sources: Diffusion coefficient of hydrogen peroxide and urea,[35] hydrodynamic radius of catalase[33] and urease.[34]

We therefore hypothesized that the maximal velocity was obtained as a balance between transient asymmetry and enzyme density. The number of enzymes on each coacervate is directly related to the potential of these enzymes to form asymmetric organizational states. For example, a coacervate with maximum enzyme loading will have a saturated, homogeneous distribution of enzymes (**Figure 3-5A**). Hence, in the presence of fuel, such coacervates with on average high symmetry (and thus very low probability of significant asymmetry) will have zero net propulsion. Although at low enzyme density the probability of asymmetric enzyme organization is higher than that at medium enzyme density, the net propulsion is still weaker as fewer enzymes are able to impart velocity, thus yielding a smaller drive capable of actively propelling the coacervate as a whole.[10] In the case of medium enzyme density, there is a favourable balance between the probability of transient asymmetry and the absolute number of enzymes contributing to propulsion, thus resulting in a larger net propulsion than for those with low and high enzyme density.

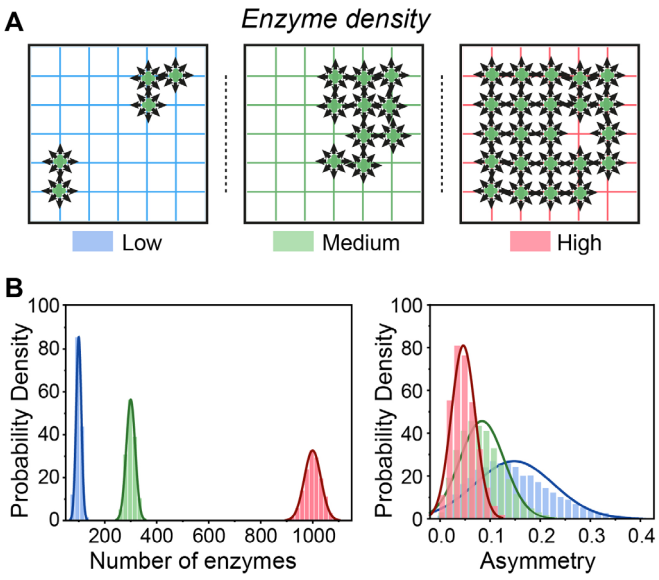

Figure 3-5 | **A.** Schematic illustration of coacervates with different enzyme densities (low, medium and high) leading to different organizational states. **B.** The distribution of the number of enzymes per coacervate is presented per density based on 100000 simulated functionalized particles of each density ($\lambda_{low} = 100$, $\lambda_{medium} = 300$, $\lambda_{high} = 1000$). The asymmetry was computed as the net propulsion in the (x, y)-plane divided by the number of enzymes (as $v_c = 1$ µm/s in these simulations) per coacervate.

To demonstrate the interplay of transient asymmetry and enzyme density, a model probability density plot of the degree of asymmetry with different enzyme numbers was derived (**Figure 3-5B**). The measure of asymmetry was defined by the net propulsion divided by the product of the enzyme number and v_c. Then two theoretical extremes were formulated: a uniform (equidistant) organization of enzymes results in 0% asymmetry, while 100% asymmetry is caused by all enzymes clustering at a single point. Sketching the relationship between enzyme density and net propulsion in a schematic illustration shows that the delicate interplay between the parameters is indeed logical (**Figure S3-2**), and in agreement with the probability density plot in **Figure 3-5B**.

3.5 Stochastic mechanism proven by modelling and simulation

To further substantiate our hypothesis of transient asymmetry-induced motility, in close collaboration with Dr. Marco de Corato we developed a stochastic mechanical model, which verified our findings from two aspects. First, we parameterized our stochastic model based on the Active Brownian Particle (ABP) model[31] to include the mobility and the fluctuations of the enzyme distributions along the surface. In this way, we were able to look at the ensemble effect of propulsive units imposed on overall coacervate motion in our system. Second, simulation (in close collaboration with Richard Post and Prof. Remco van der Hofstad) from the same stochastic model was used to verify the analytical expression and further allowed us to examine the system at the level of the individual enzyme.

In general, a stochastic process is a process where an object behaves in a random way. A well-known example is Brownian motion. In our setting, we have three stochastic processes of interest: the inherent translational (1) and rotational (2) diffusion of coacervates on microscale, as well as the lateral diffusivity (3) of the propulsive units (i.e. CAT or UR), which is unique to this system. The location of the propulsive units drives the coacervate in a particular direction, governed by the dynamic and asymmetrical distribution of the enzymes on the coacervate surface; the coacervates are reoriented during their motion as a result of the rotational diffusion.

We obtained our stochastic model by modifying the ABP model, which was originally developed to describe the motion of Janus particles.[31] In the ABP model, the catalytic hemisphere defines the direction along which the particle moves, while the rotational diffusion (τ_R) randomizes the orientation of the particle making its motion diffusive at long timescales ($\Delta t > \tau_R$).[31] In contrast, the coacervates described in this work do not display a

fixed preferential direction since the distribution of the enzyme propulsive units fluctuates with enzymes undergoing lateral diffusion. Our stochastic model assumes that the coacervate moves along the direction of the dipole of the surface distribution with a velocity proportional to its magnitude. The MSD after a time Δt was derived as

$$\mathrm{MSD}(\Delta t) = \frac{1}{2}\left(\frac{V}{D_{eff}}\right)^2 \left(e^{-2\Delta t D_{eff}} + 2\Delta t D_{eff} - 1\right) + 4D_T \Delta t, \quad (5)$$

where

$$D_{eff} = D_R + \left(1 + \frac{2}{\lambda}\right)\frac{D_L}{R^2}, \quad (6)$$

$D_T = \frac{k_B T}{6\pi\eta R}$ is the translational diffusion coefficient, D_L is the lateral diffusion coefficient of the enzymes, $D_R = \frac{k_B T}{8\pi\eta R^3}$ is the rotational diffusion coefficient of the coacervate, $k_B T$ represents the thermal energy, η is the viscosity of the liquid suspending the particle, R is the radius of the coacervate, λ is the number of enzymes on the coacervate, and V is the expected coacervate propelling velocity ($V = v_c\sqrt{\frac{2}{3}\lambda}$, where v_c is the propelling velocity of coacervate induced by one single enzyme).

This expression has limiting forms of $\mathrm{MSD}(\Delta t) = 4D_T\Delta t + V^2\Delta t^2$ for $\Delta t \ll \tau^*$ and $\mathrm{MSD}(\Delta t) = (4D_T + V^2\tau^*)\Delta t$ for $\Delta t \gg \tau^*$, where $\tau^* = D_{\mathrm{eff}}^{-1}$. The transition between the ballistic and diffusive regimes is determined by this new timescale τ^*, which thus depends on both the lateral diffusivity of the enzymes and on the rotational diffusion of the coacervate. It is important to note that enzyme lateral diffusivity contributes to the coacervate velocity and overall MSD in the stochastic model, while the ABP model did not take these two factors into account.[31]

In general, this stochastic model predicts a ballistic motion at short times and a diffusive motion at long times (**Figure 3-6A**) and this crossover from ballistic to diffusive regimes was indeed observed in the experimental data (**Figure 3-3**). In the case of rapid diffusion of surface-bound enzymes, the lifetime of asymmetry becomes short, which in turn leads to rapid velocity fluctuations. This results in a fast transition of MSD from the ballistic regime to the diffusive regime. Conversely, in the limit of diffusion-limited (static) enzymes, the polarization becomes permanent, leading to recovery of MSD, similar to those of Janus particles.[31] Similarly, motion scenarios predicted in numerical simulation have a good agreement with experimental results (**Figure 3-6B**) with the extra consideration of enzyme lateral diffusion. Brownian motion of each enzyme along the surface of the active particle was simulated. The velocity of the particle was calculated

from the diffusion of each individual enzyme, which confirmed the analytical theory presented here and explored cases where the number of enzymes is small, and fluctuations are large.

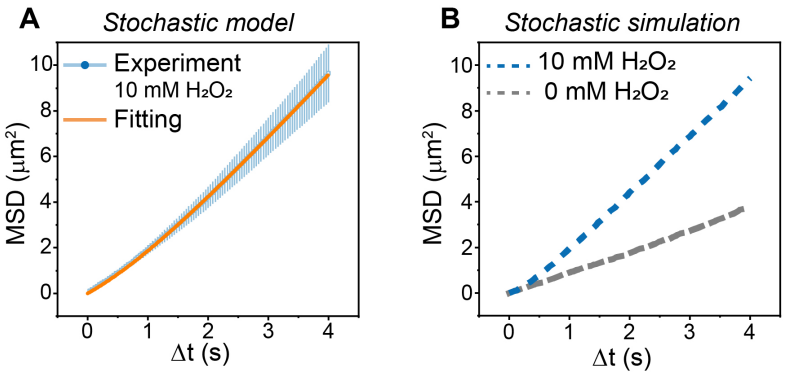

Figure 3-6 | **A.** Fitting of the MSD curve of CAT-coacervates in presence of 10 mM H_2O_2 with the stochastic model. **B.** The predicted MSD curves of CAT-coacervates in presence of 10 mM and 0 mM H_2O_2 with stochastic simulation.

3.6 Tuning motion dynamics by enzyme lateral diffusivity

The simulation identified lateral diffusivity of enzymes (D_L) as a key parameter that has a crucial impact on transient asymmetry, due to the speed at which enzyme clusters can form. Therefore, to further control the system with stochastically dominated parameters, we set out to examine the impact of lateral diffusion of enzymes on the motility by experiment and simulation. To this end, we tuned the diffusivity of surface-bound catalase experimentally by means of in-situ crosslinking of catalase using a chemical crosslinker; namely, glutaraldehyde (GA) (shown in Chapter 2, section 2.5, **Figure 3-7**). Coacervates with medium CAT density, the best performer from the enzyme density experiments, were chosen to test this diffusivity hypothesis. In order to avoid aggregation of catalase, crosslinking was carried out after extensive washing steps to remove any unbound catalase, as previously described in Chapter 2. FRAP measurements confirmed that enzyme diffusivity was drastically diminished after in-situ crosslinking of CAT-coacervates (**Figure 2-8**), as compared to that of no crosslinking.

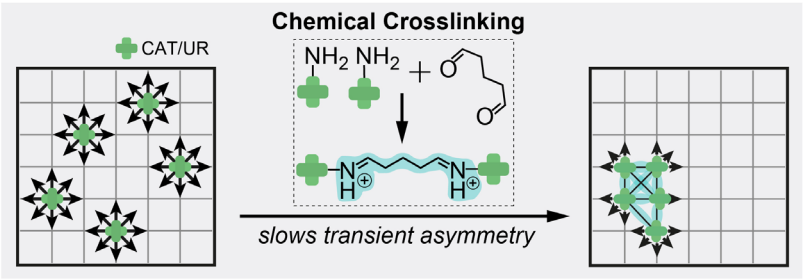

Figure 3-7 | Schematic illustration of transient asymmetry slowed down by crosslinking, leading to faster propulsion.

In order to amplify the motility output, and thus to observe any difference that might arise because of changing the lateral diffusion of enzymes, we aimed at capturing the ballistic regime of MSD curves (rather than the diffusive regime). In order to do so, CAT-coacervates with average diameter of 3.6 μm (see Chapter 2 for coacervate size tuning method) were chosen to perform motility testing, as their characteristic timescale satisfies $\tau^* >> \Delta t$, resulting in a more predominant influence of D_L on the coacervates' motion (Equation 6). After crosslinking, a clear difference was observed regarding motility: CAT-coacervates with crosslinked surface enzymes, with the same average size, exhibited increased MSDs and velocities when compared to their non-crosslinked counterparts (**Figure 3-8**). This propulsive motion can clearly be seen in the movement trajectories, where more stretched and expanded paths were observed for crosslinked ones (**Figure 3-8A**). Should the organizational state of enzymes in the non-crosslinked state be permanent and not changing with time, there would not have been a motion enhancement after fixating the enzymes. By tuning enzyme lateral diffusivity, we eventually imposed control over the lifetime of transient asymmetry, which was manifested in the motility output. The enhanced propulsion after crosslinking clearly confirmed the role of the fluidic membrane in imparting transient asymmetry and thus motility.

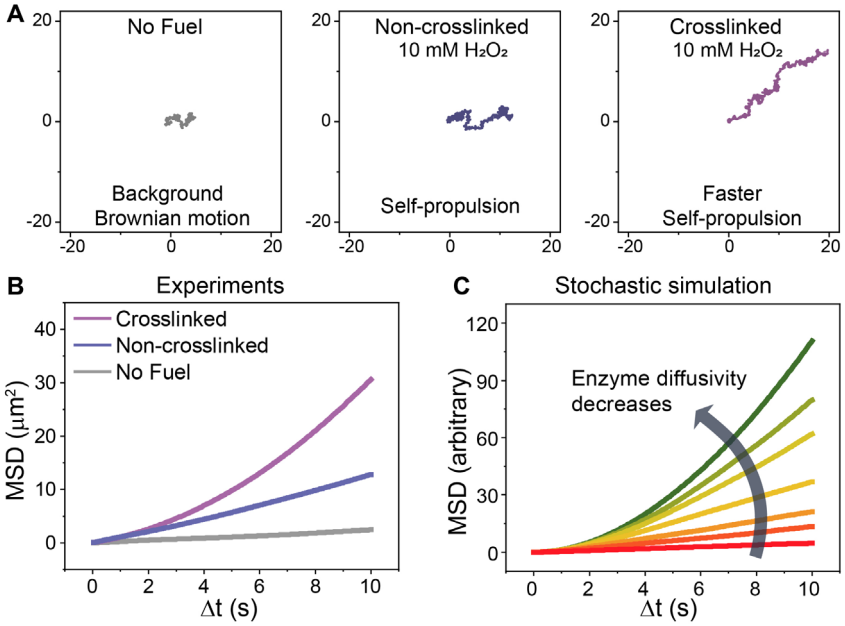

Figure 3-8 | **A, B.** Representative trajectories and MSD curves of non-crosslinked CAT-coacervates (diameter~3.6 μm) with no hydrogen peroxide (no fuel), 10 mM peroxide (non-crosslinked) and crosslinked CAT-coacervates with 10 mM hydrogen peroxide, respectively. MSD curves with error bars (mean ± SEM) are available in **Figure S3-3**. **C.** Stochastic simulation predicts that MSD increases with decreasing enzyme diffusivity.

We further tested the impact of lateral diffusion of enzymes on the motility by tuning D_L in the stochastic model. In the extreme case, where $D_L = 0$ (completely static motor arrangement), the MSD is at the maximum. While in the theoretical case where D_L is infinite, dynamic enzyme clustering and its resultant transient asymmetry fluctuate at a rate that is much faster than the measurement timeframe, the MSD profile is the same as that of Brownian motion. Overall, by decreasing D_L in the stochastic model, an increase in MSDs was predicted (**Figure 3-8C**). Moreover, by matching D_L in simulation with experimental values from FRAP, our prediction by stochastic simulation is in line with experimental results (**Figure S3-3B**). This agreement between theoretical predictions and experimental validation provides a valuable framework for the incorporation of stochastic mechanisms in synthetic systems.

In addition, an interesting phenomenon was observed that *ca.* 10% of such non-crosslinked coacervates exhibited anomalous type of motion, so-called run-and-tumble, hitherto only observed in bacteria (e.g., *Escherichia Coli* [36]). These non-linear run-and-

tumble movements can be characterized by remarkable consecutive alternations between diffusive motion and directional propulsion (**Figure 3-9**). Analysis of the instantaneous velocity confirmed our observation, with the experimentally observed 'run' regime exhibiting significantly higher velocities than predicted by the stochastic model. With our current theoretical settings, we could not simulate this run-and-tumble behaviour, indicating another degree of stochasticity/complexity in the system. As this behaviour was only observed with the catalase attached coacervates, we tentatively attribute this phenomenon to a possible explanation - the stochastic release of oxygen microbubbles, as previously reported by the group of Wang. [37] Nevertheless, a thorough investigation is needed to substantiate this explanation.

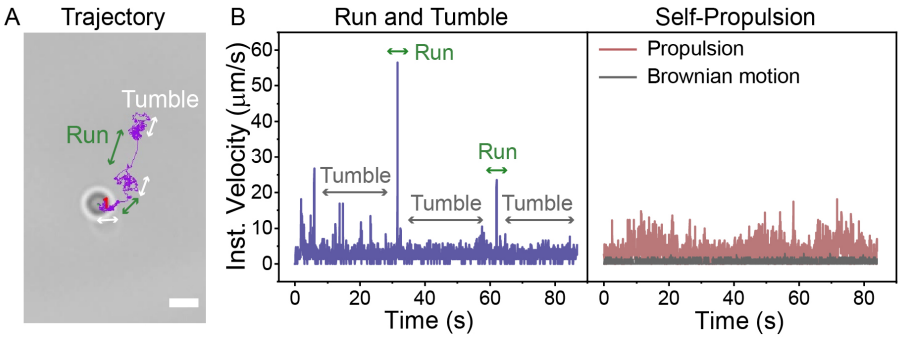

Figure 3-9 | A. Representative trajectory of a CAT-coacervate undergoing run-and-tumble in the presence of 10mM H_2O_2. Run and tumble regimes are indicated with green and white arrows, respectively. Scale bar represents 1 μm. **B.** Instantaneous velocity of run-and-tumble, self-propulsion (10 mM H_2O_2) and Brownian motion (0 mM H_2O_2). In the case of run-and-tumble, velocity suddenly increased during run phases (as depicted in B). Such sudden increase of velocity was not observed in the case of normal self-propulsion.

3.7 Conclusions

Stochasticity is abundant in nature and of great importance for the regulation of many biological processes. Although this has been well recognized, it has mainly been studied from a phenomenological point of view and its active exploitation is underexplored. This certainly accounts for artificial systems, where researchers have in some cases acknowledged stochasticity to play a key role in the behaviour of their systems but have not controlled, let alone designed-in, this phenomenon. In this chapter we have demonstrated an engineered motile system that is fully governed by stochasticity. By following a combined experimental and theoretical/simulation approach with our collaborators, we have been able not only to describe the motile process but also to

engineer the key parameters that determine stochastic behaviour. The great fit between theory and experiment demonstrates that we now have a high level of control over this process. We have added only one more level of stochasticity (lateral diffusion of enzyme) on two inherent stochastic processes (translational and rotational diffusion) present in motor systems. Although our results explain the majority of motile events, we have also observed a small fraction that shows an intriguing 'run-and-tumble' behaviour. These extreme cases cannot be described by our current theoretical model and most probably result from a combination of stochastic processes that we do not fully understand yet. It however demonstrates that exploring stochasticity can enable the creation of even more complex, non-linear behaviour. For example, research exploring the impact of confinement on such stochastic-induced motility will be discussed in the next chapter. Hopefully this study will inspire other researchers to recognize and apply stochasticity as a powerful method to design and engineer other adaptive systems based on fluctuating extrinsic and intrinsic conditions.

Experimental section

Materials

All materials were used as received unless otherwise stated. The preparation of the enzyme-labeled coacervates was described in Chapter 2. 30% hydrogen peroxide solution, urea and glutaraldehyde solution were obtained from Sigma-Aldrich. Hydrogen peroxide solutions used for motility experiments were prepared by sequential dilutions of 30% hydrogen peroxide solution.

Motility test for CAT-/UR-coacervates

Experimental chamber

A simple experimental chamber was designed and prepared to minimize side effects that could be mistaken as self-propulsion, such as drift or solution evaporation. This chamber was made from two glass microscopy slides spaced by two pieces of autoclave tape. Autoclave tape was first attached to a larger glass slide on two ends, followed by the addition of sample in the middle, and capping by a smaller glass slide.

Optical recording

The videos of coacervate motion were recorded using a camera (Hamamatsu Digital Camera C11440) on an inverted optical microscope (Leica DMi8). A 63× water immersion objective was used for this recording.

Stochastic simulation

The backbone of the stochastic simulation (as designed by our collaborators Richard Post and Prof. Remco van der Hofstad) is a result of the simulation of a Spherical Brownian Motion (SBM).[38] The motility of a coacervate with a dynamic membrane was simulated by the union of three independent stochastic processes: i) the translational diffusion of the coacervate was simulated as a realization of a three-dimensional Brownian motion depending on the diffusion speed D_T, ii) the rotational diffusion of the coacervate, causing the direction of the net velocity to change over time, was simulated by implementation of an SBM of one of the unit axes. This way we could implement rotation of the 3D coordinate system at a speed depending on D_R, and iii) the lateral diffusion of each single enzyme, causing the magnitude of the net velocity to change over time, was simulated as independent SBM at a speed depending on D_L.

Estimation of simulation parameters

In the stochastic simulation there were 6 parameters that influenced the motility of enzyme-tethered coacervates; namely, the propelling velocity of coacervates induced by one single enzyme v_c, coacervate radius R, translational diffusion coefficient D_T, rotational diffusion coefficient D_R, enzyme lateral diffusion coefficient D_L and enzyme number on the surface of coacervate λ. However, from Equation 5 it became clear that the impact of v_c and λ could be integrated in the expected coacervate velocity $V = v_c\sqrt{\frac{2}{3}\lambda}$ because the influence of λ on D_{eff} (stated in Equation 6) could be ignored for the order of λ (shown in **Table 3-2**). This thus reduces the number of relevant simulation parameters to 5.

R was obtained from the analysis of coacervate confocal images (Chapter 2). To obtain realistic parameter estimates, first $\frac{k_B T}{6\pi\eta}$ was estimated to equal 0.14 based on the experimental MSD curves of coacervates in the absence of fuel (**Figure S3-4**) and in turn used to estimate D_R and D_T according to the Stokes-Einstein equation. After substituting the estimates of D_R and D_T into Equation 5 and 6, this equation was fitted to the experimentally obtained MSD curves to estimate D_L and V for the conditions of interest. Besides, the estimate of V is within reasonable range of micromotors (see Table below) and comparable to other micromotor systems which used the same type of enzyme as propulsion unit.[39]

Parameter	Estimate used in simulation (μm/s)	Standard Error
$V_{1.8}$	0.576	0.002
$V_{0.6,low\text{-}CAT}$	0.587	0.025
$V_{0.6,med\text{-}CAT}$	0.964	0.009
$V_{0.6,high\text{-}CAT}$	0.754	0.020
$V_{0.6,low\text{-}UR}$	0.470	0.052
$V_{0.6,med\text{-}UR}$	0.985	0.098
$V_{0.6,high\text{-}UR}$	0.295	0.051

* $V_{0.6,low\text{-}CAT}$: V for CAT-coacervates (radius of ~0.6 μm) with low enzyme density.

Supporting Information

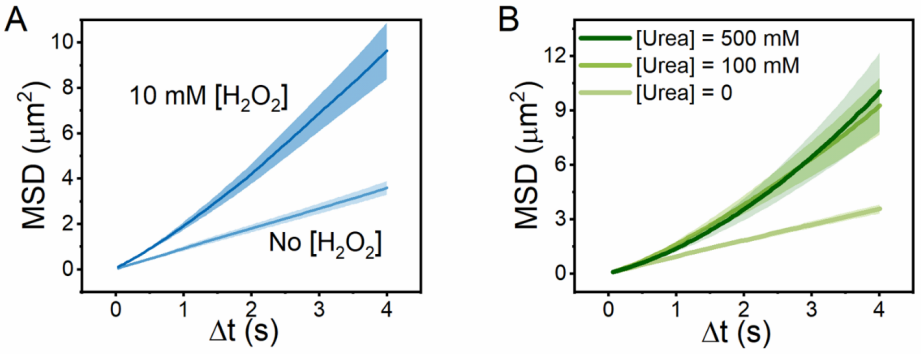

Figure S3-1 | MSD curves of CAT-coacervates (**A**) (n = 18, mean ± SEM) and UR-coacervates (**B**) (n = 17, mean ± SEM) in the absence / presence of their respective fuels.

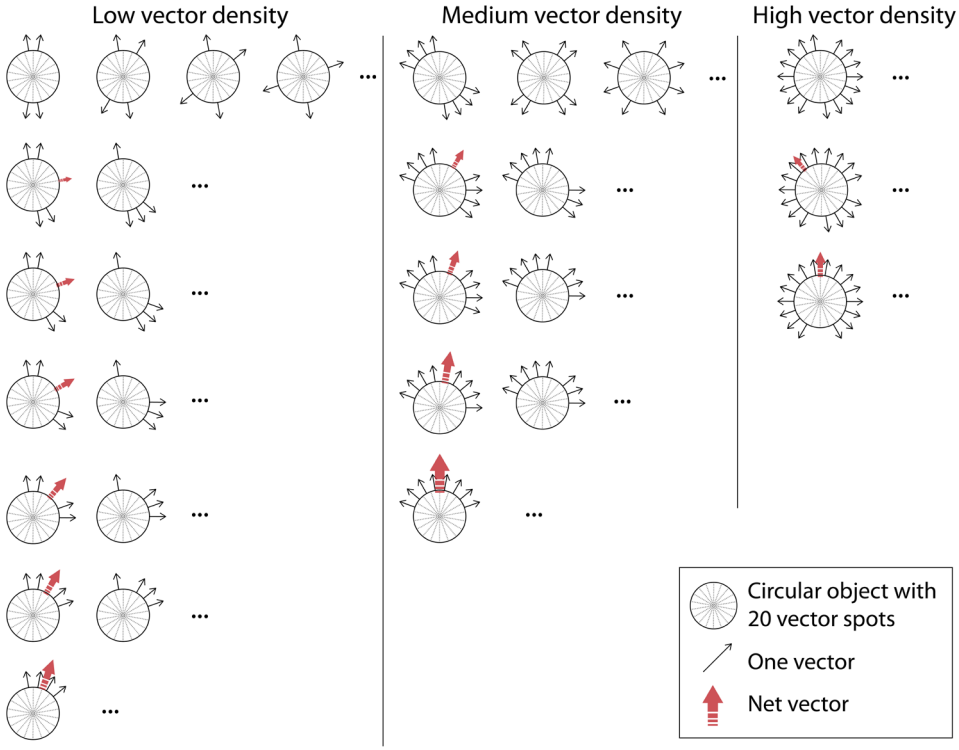

Figure S3-2 | Schematic illustration of relationship between vector density (enzyme density in 2D) and total generated propulsion. Please note: this figure is only for illustrating the idea of interplay, and it doesn't imply the moving direction of enzymes or coacervates.

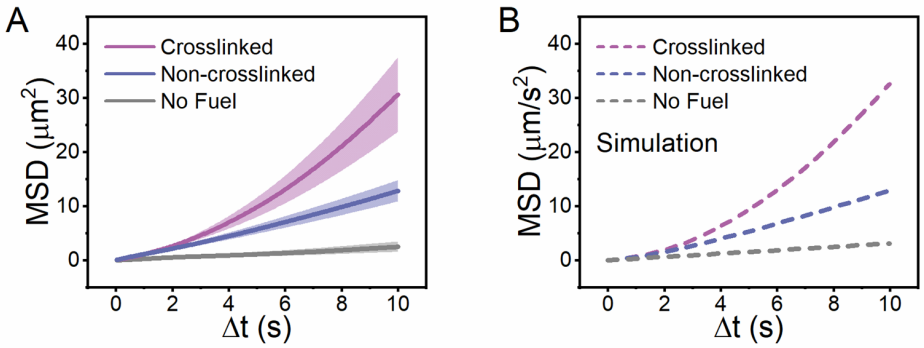

Figure S3-3 | **A.** MSD curves of non-crosslinked CAT-coacervates (diameter~3.6 μm) with no hydrogen peroxide (no fuel), 10 mM peroxide (non-crosslinked) and crosslinked CAT-coacervates with 10 mM peroxide. For all conditions, n = 18, and data are represented as mean ± SEM. **B.** MSD curves predicted by stochastic simulation.

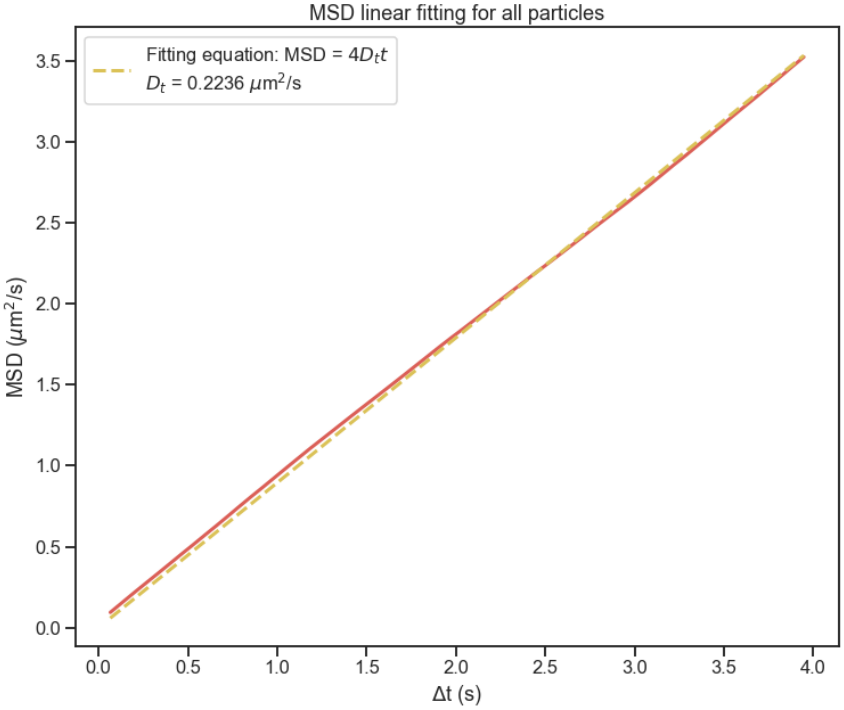

Figure S3-4 | Linear fitting of MSD curve of UR-coacervates ((diameter~1.2 μm, n = 17) in the absence of fuel. The fitting equation is derived from Equation 2a (V = 0 without fuel).

Acknowledgements

Richard Post and Prof. Remco van der Hofstad are thanked for stochastic simulations. Prof. Samuel Sanchez is thanked for his suggestions regarding the motor design and Python-based tracking script. Dr. Marco De Corato is thanked for stochastic modelling. Dr. Rafael Mestre is thanked for his Python-based Nano-micromotor Analysis Tool (NMAT) v.1. Xavier Arqué and Ana Hortelão are thanked for useful tips and discussion.

References

[1] Courgeon, M.; Desplan, C., Coordination between stochastic and deterministic specification in the Drosophila visual system. *Science* **2019,** *366* (6463).

[2] Duke, T.; Leibler, S., Motor protein mechanics: a stochastic model with minimal mechanochemical coupling. *Biophys. J.* **1996,** *71* (3), 1235-1247.

[3] van den Heuvel, M. G. L.; Dekker, C., Motor Proteins at Work for Nanotechnology. *Science* **2007,** *317* (5836), 333.

[4] Cooper, G. M., *The cell: a molecular approach 2nd Edition*. Sinauer Associates: Sunderland (MA), 2000.

[5] Arqué, X.; Romero-Rivera, A.; Feixas, F.; Patiño, T.; Osuna, S.; Sánchez, S., Intrinsic enzymatic properties modulate the self-propulsion of micromotors. *Nat. Commun.* **2019,** *10* (1), 2826.

[6] Kumar, B. V. V. S. P.; Patil, A. J.; Mann, S., Enzyme-powered motility in buoyant organoclay/DNA protocells. *Nat. Chem.* **2018,** *10* (11), 1154-1163.

[7] Pijpers, I. A. B.; Cao, S.; Llopis-Lorente, A.; Zhu, J.; Song, S.; Joosten, R. R. M.; Meng, F.; Friedrich, H.; Williams, D. S.; Sánchez, S.; van Hest, J. C. M.; Abdelmohsen, L. K. E. A., Hybrid Biodegradable Nanomotors through Compartmentalized Synthesis. *Nano Lett.* **2020,** *20* (6), 4472-4480.

[8] Kudernac, T.; Ruangsupapichat, N.; Parschau, M.; Maciá, B.; Katsonis, N.; Harutyunyan, S. R.; Ernst, K.-H.; Feringa, B. L., Electrically driven directional motion of a four-wheeled molecule on a metal surface. *Nature* **2011,** *479* (7372), 208-211.

[9] Ji, Y.; Lin, X.; Zhang, H.; Wu, Y.; Li, J.; He, Q., Thermoresponsive Polymer Brush Modulation on the Direction of Motion of Phoretically driven Janus Micromotors. *Angew. Chem., Int. Ed.* **2019,** *58* (13), 4184-4188.

[10] Patiño, T.; Feiner-Gracia, N.; Arqué, X.; Miguel-López, A.; Jannasch, A.; Stumpp, T.; Schäffer, E.; Albertazzi, L.; Sanchez, S., Influence of enzyme quantity and distribution on the self-propulsion of non-Janus urease powered micromotors. *J. Am. Chem. Soc.* **2018,** *140* (25), 7896-7903.

[11] Ghosh, S.; Mohajerani, F.; Son, S.; Velegol, D.; Butler, P. J.; Sen, A., Motility of Enzyme-Powered Vesicles. *Nano Lett.* **2019,** *19* (9), 6019-6026.

[12] Yewdall, N. A.; Buddingh, B. C.; Altenburg, W. J.; Timmermans, S.; Vervoort, D. F. M.; Abdelmohsen, L.; Mason, A. F.; van Hest, J. C. M., Physicochemical Characterization of Polymer-Stabilized Coacervate Protocells. *ChemBioChem* **2019,** *20* (20), 2643-2652.

[13] Delcroix, D.; Martín-Vaca, B.; Bourissou, D.; Navarro, C., Ring-opening polymerization of trimethylene carbonate catalyzed by methanesulfonic acid: activated monomer versus active chain end mechanisms. *Macromolecules* **2010,** *43* (21), 8828-8835.

[14] Golestanian, R.; Liverpool, T.; Ajdari, A., Designing phoretic micro-and nano-swimmers. *New J. Phys.* **2007,** *9* (5), 126.

[15] Illien, P.; Golestanian, R.; Sen, A., 'Fuelled'motion: phoretic motility and collective behaviour of active colloids. *Chem. Soc. Rev.* **2017,** *46* (18), 5508-5518.

[16] Ren, L.; Wang, W.; Mallouk, T. E., Two Forces Are Better than One: Combining Chemical and Acoustic Propulsion for Enhanced Micromotor Functionality. *Acc. Chem. Res.* **2018,** *51* (9), 1948-1956.

[17] Lee, T.-C.; Alarcón-Correa, M.; Miksch, C.; Hahn, K.; Gibbs, J. G.; Fischer, P., Self-propelling nanomotors in the presence of strong Brownian forces. *Nano Lett.* **2014,** *14* (5), 2407-2412.

[18] Pourrahimi, A. M.; Villa, K.; Manzanares Palenzuela, C. L.; Ying, Y.; Sofer, Z.; Pumera, M., Catalytic and Light-Driven ZnO/Pt Janus Nano/Micromotors: Switching of Motion Mechanism via Interface Roughness and Defect Tailoring at the Nanoscale. *Adv. Funct. Mater.* **2019,** *29* (22), 1808678.

[19] Schattling, P. S.; Ramos-Docampo, M. A.; Salgueiriño, V. n.; Städler, B., Double-fueled Janus swimmers with magnetotactic behavior. *ACS nano* **2017,** *11* (4), 3973-3983.

[20] Ebbens, S. J.; Gregory, D. A., Catalytic Janus Colloids: Controlling Trajectories of Chemical Microswimmers. *Acc. Chem. Res.* **2018,** *51* (9), 1931-1939.

[21] Schattling, P.; Thingholm, B.; Stadler, B., Enhanced diffusion of glucose-fueled Janus particles. *Chem. Mater.* **2015,** *27* (21), 7412-7418.

[22] Jin, C.; Krüger, C.; Maass, C. C., Chemotaxis and autochemotaxis of self-propelling droplet swimmers. *Proc. Natl. Acad. Sci. U. S. A.* **2017,** *114* (20), 5089.

[23] Izri, Z.; van der Linden, M. N.; Michelin, S.; Dauchot, O., Self-Propulsion of Pure Water Droplets by Spontaneous Marangoni-Stress-Driven Motion. *Phys. Rev. Lett.* **2014,** *113* (24), 248302.

[24] Maass, C. C.; Krüger, C.; Herminghaus, S.; Bahr, C., Swimming Droplets. *Annual Review of Condensed Matter Physics* **2016,** *7* (1), 171-193.

[25] van der Weijden, A.; Winkens, M.; Schoenmakers, S. M. C.; Huck, W. T. S.; Korevaar, P. A., Autonomous mesoscale positioning emerging from myelin filament self-organization and Marangoni flows. *Nat. Commun.* **2020,** *11* (1), 4800.

[26] Babu, D.; Scanes, R. J. H.; Plamont, R.; Ryabchun, A.; Lancia, F.; Kudernac, T.; Fletcher, S. P.; Katsonis, N., Acceleration of lipid reproduction by emergence of microscopic motion. *Nat. Commun.* **2021,** *12* (1), 2959.

[27] Manjare, M.; Yang, F.; Qiao, R.; Zhao, Y., Marangoni Flow Induced Collective Motion of Catalytic Micromotors. *J. Phys. Chem. C* **2015,** *119* (51), 28361-28367.

[28] Zhao, G.; Pumera, M., Marangoni self-propelled capsules in a maze: pollutants 'sense and act' in complex channel environments. *Lab Chip* **2014,** *14* (15), 2818-2823.

[29] Mestre, R.; Palacios, L. S.; Miguel-López, A.; Arqué, X.; Pagonabarraga, I.; Sánchez, S., Extraction of the propulsive speed of catalytic nano-and micro-motors under different motion dynamics. *arXiv preprint arXiv:2007.15316* **2020**.

[30] Mestre, R. Python-based Nano-micromotor Analysis Tool (NMAT) v.1. https://github.com/rafamestre/NMAT-nanomicromotor-analysis-tool.

[31] Howse, J. R.; Jones, R. A.; Ryan, A. J.; Gough, T.; Vafabakhsh, R.; Golestanian, R., Self-motile colloidal particles: from directed propulsion to random walk. *Phys. Rev. Lett.* **2007,** *99* (4), 048102.

[32] Dunderdale, G.; Ebbens, S.; Fairclough, P.; Howse, J., Importance of particle tracking and calculating the mean-squared displacement in distinguishing nanopropulsion from other processes. *Langmuir* **2012,** *28* (30), 10997-11006.

[33] Axelsson, I., Characterization of proteins and other macromolecules by agarose gel chromatography. *J. Chromatogr. A* **1978,** *152* (1), 21-32.

[34] Follmer, C.; Pereira, F. V.; Da Silveira, N. P.; Carlini, C. R., Jack bean urease (EC 3.5.1.5) aggregation monitored by dynamic and static light scattering. *Biophys. Chem.* **2004,** *111* (1), 79-87.

[35] Gosting, L. J.; Akeley, D. F., A Study of the Diffusion of Urea in Water at 25° with the Gouy Interference Method. *J. Am. Chem. Soc.* **1952,** *74* (8), 2058-2060.

[36] Popescu, M. N.; Uspal, W. E.; Bechinger, C.; Fischer, P., Chemotaxis of active Janus nanoparticles. *Nano Lett.* **2018,** *18* (9), 5345-5349.

[37] Nourhani, A.; Karshalev, E.; Soto, F.; Wang, J., Multigear Bubble Propulsion of Transient Micromotors. *Research* **2020,** *2020*, 9.

[38] Mijatović, A.; Mramor, V.; Bravo, G. U., A note on the exact simulation of spherical Brownian motion. *Stat. Probab. Lett.* **2020,** *165*, 108836.

[39] De Corato, M.; Arqué, X.; Patiño, T.; Arroyo, M.; Sánchez, S.; Pagonabarraga, I., Self-Propulsion of Active Colloids via Ion Release: Theory and Experiments. *Phys. Rev. Lett.* **2020,** *124* (10), 108001.

CHAPTER 4

Confined Motion: Motility of Active coacervate motors in Cell-Sized Lipid Vesicles

Abstract

Active materials can transduce external energy into kinetic energy at the nano and micron length scales. Traditionally, motility is studied as a function of internal features such as particle topology, while external parameters such as energy source are assessed mainly in bulk. However, in real-life applications, confinement plays a crucial role in determining the type of motion active particles can adapt. This feature has been however surprisingly underexplored experimentally. In this chapter, we showcase a tunable experimental platform to gain insight into the dynamics of active particles in environments with restricted 3D topology. Particularly, we examined the autonomous motion of coacervate micromotors confined in giant unilamellar vesicles (GUVs) spanning 10 to 40 μm size range, and varied parameters including fuel and micromotor concentration. We observed anomalous diffusion upon confinement, leading to decreased motility, which was more pronounced in smaller GUVs. The results indicate that the theoretically predicted hydrodynamic effect dominates the motion mechanism within this platform.

Shidong Song, Antoni Llopis-Lorente, et al., *Manuscript in preparation*

4.1 Introduction

Nano and micromotors are a class of materials able to harness free energy from their surroundings and transform it into kinetic energy.[1-11] This ability, as well as their wide application window, have incited a considerable interest in active materials to further explore their adaptability, versatility, and functionality. The vast majority of research has focused on controlling intrinsic parameters of the motor systems that govern their activity, such as size, shape and asymmetric placement of motile units.[12-17] External factors that have been studied mainly concern the application of different energy sources, which can vary from chemical fuels to light and magnetic field induced motion.[4-5, 18-20] With these external forces, it has proven to be possible to induce life-like behaviour, such as directed motion (e.g. chemo- and phototaxis)[21-24] and swarming behaviour,[25-29] when single motile particles are able to interact with each other in a concerted fashion. In all of these cases motile behaviour is regarded as a bulk property. One aspect that has however hardly been taken into account is that in living systems motion is often restricted by the confined space in which the motile objects operate. This feature is apparent when for example the motility of bacteria in biofilms and the restricted motion of blood cells in capillary veins is regarded. To get a better understanding of how motile particles move under real-life conditions, in a considerable number of cases confinement should therefore be taken into account.

Still, only a limited number of theoretical and even fewer experimental studies have investigated motion of microparticles near 2D surfaces or under microfluidic confinement.[30-38] In general, these studies focus on the influence of the motor architecture and composition, and the topology of the environment (e.g., dimensional space and surface pattern). Different types of motion including diffusion, sliding along the wall, and docking and unclogging, were observed experimentally for Janus-type micro swimmers as a result of varying the size of confinement.[33] For example, Liu et al.[36] investigated a self-propulsive bimetallic swimmer in linear and curved microfluidic channels - both experimentally and with numerical simulations. They observed enhanced motion upon confinement as a result of an increased self-generated electric field, which acted as the motors' driving force. They predicted a further increase in velocity upon decreasing the size of confinement. On the contrary, Khezri et al. reported an experimentally observed reduction in velocity of copper/platinum bimetallic swimmers upon confinement in microfluidic channels.[37] Moreover, decreasing the size of the channels resulted in a significant decrease in velocity. Besides bimetallic self-

electrophoretic motors (which move by the generation of a local electric gradient), diffusiophoretic motors (which move by the generation of a local gradient of decomposition products) have also been studied under confinement. However, two theoretical studies reported opposite results – one predicted an increase in velocity in spherical confinement,[35] and the other predicted a slowing-down when motors were near the confining boundaries.[34] Both studies attributed the changes in velocity to interaction between the boundaries and the chemical concentration gradients generated by the motors. It is clear from all these reports that a complex, yet poorly understood interplay exists between the confinement topology and the propulsion mechanism, which is responsible for dictating motion dynamics in confined spaces. There is thus a clear need for robust experimental systems that allow the validation of the theoretical models that have been proposed.

A probable cause for the lack of experimental data is the difficulty of establishing such a platform in which motile behaviour can be effectively studied in a 3D confined space. In this chapter, we report the experimental realization of compartmentalized micromotors in the interior of 3D, semi-permeable micron-sized vesicles, which enables us to systematically study their motile behaviour under confinement. In particular, we show the compartmentalization in giant unilamellar vesicles (GUVs) of active soft particles, composed of coacervates, surface-decorated with enzyme motile units. We demonstrate their restricted autonomous movement, when compared to unrestricted, bulk situations. By analysis of the motors' mean square displacements (MSD), we could identify that the motile systems attained anomalous diffusion coefficients, which meant that they show remarkable sub-diffusive behaviour in absence or presence of relatively low concentrations of chemical fuel; normal diffusivity was restored upon increasing the substrate concentration. These effects were systematically studied as a function of GUV size, motor density and fuel concentration. Based on these results, we can conclude 3D confinement leads to restricted motion of motor systems.

4.2 Assembly of GUV of light-driven coacervate micromotors.

The construction of our confined motile platform is depicted in **Figure 4-1**. As active particles, we employed our previously developed enzyme-functionalized coacervate microdroplets (diameter 1.2 ± 0.4 μm, see Chapter 2 and 3). In brief, coacervates were formed by self-assembly of two oppositely charged amyloses (carboxymethylated and ammonium quaternized, respectively), followed by addition of a mixture of N_3-

functionalized block polymer and non-functionalized terpolymer that together formed a stabilizing and fluidic membrane on the coacervate surface. Afterwards, dibenzocyclooctyne (DBCO) modified catalase enzymes (CAT) were attached to the coacervate membrane through a strain-promoted alkyne-azide cycloaddition (SPAAC) reaction. Thereafter we encapsulated the enzyme-functionalized coacervates in giant unilamellar vesicles (GUVs) employing an inverted emulsion technique (also known as droplet transfer method) to construct our compartmentalized motor system. First, we prepared a mixture of lipids in paraffin oil, to which an aqueous phase containing the coacervates was added. Upon emulsification, lipid-stabilized water-in-oil droplets were formed and the mixture was then layered on top of an aqueous phase for centrifugation (**Figure 4-1A**). The centrifugal force led to a transfer of droplets through the interface containing a single layer of lipid molecules, forming bilayered GUVs that sedimented at the bottom of the centrifugal tube, from where they could be harvested and purified. Both the lipid GUV bilayer and the coacervate particles were labelled with complementary markers (RhB-DOPC and Cy5-catalase, respectively), which allowed their visualization by fluorescence confocal microscopy. Importantly, the addition of coacervate particles did not compromise the assembly and integrity of the GUVs (**Figure S4-1**), and 3D confocal imaging confirmed the successful integration of coacervates inside the lipid micro-compartment (**Figure 4-1B**).

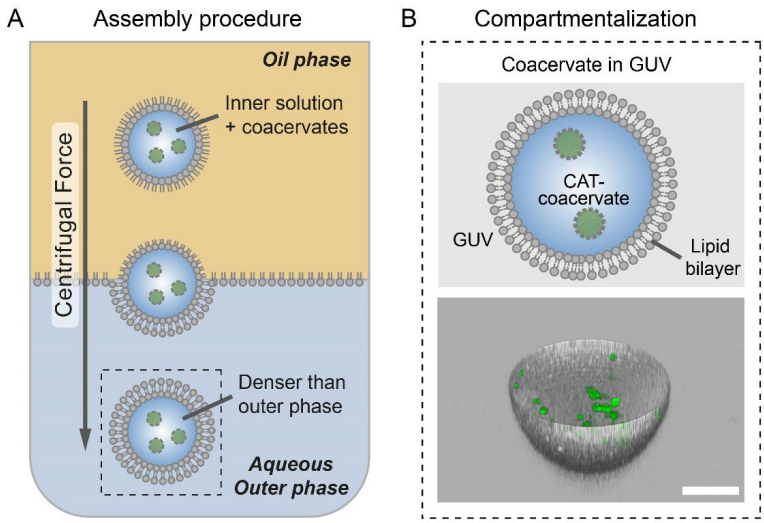

Figure 4-1 | Assembly of GUVs containing active coacervate particles. **A.** Schematic illustration of coacervate motors being encapsulated in GUVs via the droplet transfer method. **B.** Upper image shows a

cartoon of compartmentalized CAT-coacervates inside a GUV. Lower image displays a 3D confocal image reconstituted from confocal image stacks (Green: catalase which was modified with Cyanine 5, grey: RhB-DOPC as marker of the lipid membrane). Scale bar represents 10 µm.

4.3 Motion dynamics of coacervate motors under GUV confinement

Having confirmed the encapsulation of coacervates in GUVs, we first measured their autonomous motion under non-compartmentalizing conditions (i.e., in bulk as in Chapter 3). For this purpose we employed similar CAT-coacervates as used for the compartmentalization approach. Their motility was recorded in the presence or absence of their substrate, H_2O_2, by bright-field microscopy (5 frames per second). Thereafter, we analysed the X, Y trajectories and calculated the mean square displacement (MSD) of 40 coacervate particles, from multiple videos, by using a tailor-made Python script.[39-40] In the absence of fuel, typical Brownian motion with linear MSD fitting profiles (**Figure 4-2A**) was observed for the CAT-coacervates. Upon addition of H_2O_2 (0.034% v/v), CAT-coacervates displayed enhanced diffusion with expanded trajectories and significantly increased MSD profiles, leaning toward a parabolic curve (**Figure 4-2A**). This behaviour was in line with previous findings shown in Chapter 3. The mechanism of coacervate motion is regarded to be self-diffusiophoretic in nature (**Figure 4-2B**), i.e., by converting the fuel, the particles intrinsically create a product gradient surrounding their active patches (where catalase molecules cluster), which causes an osmotic imbalance and results in enhanced propulsion of the particles.

Next, we studied the motility of the CAT-coacervates within GUV confinement. First, coacervates-in-GUVs were diluted in an aqueous phase (either containing or not containing the enzymatic substrate as fuel, i.e., H_2O_2) and subsequently transferred to an experimental chamber (same as in Chapter 3). To record the coacervate trajectories, we examined their motion using bright field microscopy, as it allowed to combine the observation of both the GUV compartment and inner coacervate motors. In the absence of fuel, coacervates confined in GUVs underwent motion with relatively short paths, which translated into a flattened MSD profile (**Figure 4-2C**). In the presence of fuel, we observed enhanced propulsion as a result of catalase-mediated decomposition of H_2O_2, which translated into expanded trajectories and a significant increase in the MSD profile (**Figure 4-2C**). Remarkably, comparing the MSD profiles of non-compartmentalized *vs.* compartmentalized coacervates (**Figure 4-2A** and **C**), we found striking differences in their autonomous motion behaviours: not only did the compartmentalized coacervates

exhibit lower MSD values in the absence and presence of fuel, but the shape of the MSD curves in the presence of fuel changed from concave upward for the non-compartmentalized particles to nearly linear for the compartmentalized ones (indicative of restricted motion). To further confirm the effect of confinement on the motion dynamics and rule out effects of membrane-induced limited diffusion of substrate/products, we monitored the coacervates' motion in GUVs comprising a highly permeable membrane (i.e., with inserted α-hemolysin membrane pores, see Experimental section). The MSDs resulting from coacervate motion upon addition of H_2O_2 (0.034% v/v) (**Figure 4-2D**) showed a similar MSD curve shape as displayed in **Figure 4-2C**, thus indicating that the anomalous motion dynamics were not affected by substrate diffusion issues, but a result of the confinement effect.

The change in motion dynamics under confinement, when compared to unrestrained conditions, allowed us to probe different theories that describe confined motion. [34-35] For this purpose, we systematically investigated three parameters which we expected to have an effect on motility, namely fuel concentration, GUV confinement size and coacervate motor density.

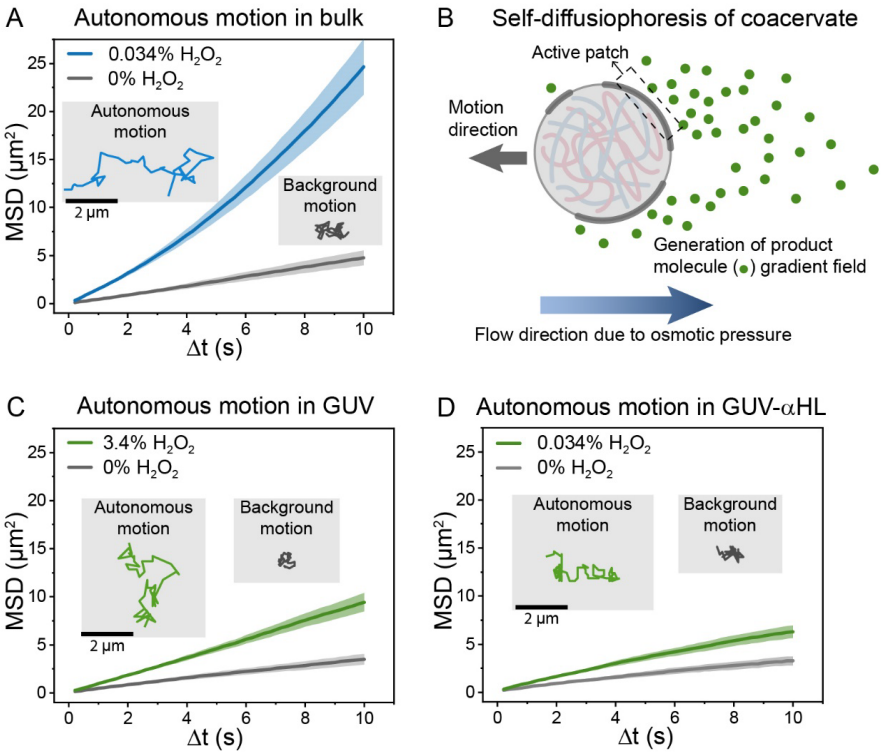

Figure 4-2 | Investigation of CAT-coacervates' motion dynamics under GUV confinement. **A.** Motility profile of CAT-coacervates in bulk solution. A parabolic increase in MSD curves was observed upon addition of fuel. **B.** Schematic illustration of self-diffusiophoresis of coacervates in solution. Active patches (catalase dynamic clusters) along the coacervate membrane release product molecules in the surrounding, leading to an asymmetric product molecule gradient field and therefore osmotic imbalance. Subsequent fluid flow induced by osmotic pressure eventually results in motion of coacervates. **C.** Motility profile of CAT-coacervate motors in GUVs. A significant increase in the MSD curve and an expansion in trajectory were observed upon addition of fuel. **D.** Motility profile of CAT-coacervate motors in GUVs with inserted α-hemolysin. Data of MSD curves (A, C, D) are represented as mean ± SEM.

4.4 Motion dynamics of coacervates in GUVs depending on fuel concentration

Having confirmed that GUV confinement altered motion regimes, we set out to investigate the extent of the confinement effect on motion dynamics by studying the crossover of different motion regimes in confinement. We therefore performed motility experiments of coacervates-in-GUVs at different fuel concentrations. A direct relationship between the MSD values and fuel concentrations was observed (**Figure 4-3A**), with higher H_2O_2 concentration leading to faster motion and more expanded trajectories (**Figure 4-3B**). Interestingly, in the presence of H_2O_2, MSD curves deviated from a straight line at higher time intervals (Δt >5s), resulting in a concave downward shape. Generally, when colloidal particles undergo Brownian motion, i.e. normal diffusion, they exhibit an MSD that is linear in time – a deviation from such trend is indicative of anomalous diffusion. Mathematically, anomalous diffusion is described as MSD $= K\Delta t^{\alpha}$.[41] Here α is the anomalous exponent that indicates how far the motion deviates from normal Brownian motion: (i) α = 1 indicates Brownian (or normal diffusive) motion, (ii) α > 1 is indicative of a super-diffusive process, and (iii) α < 1 is indicative of a sub-diffusive process. To gain further insight into the motile behaviour of the confined coacervates, MSD curves were fitted with MSD $= K\Delta t^{\alpha}$ to obtain the anomalous exponent α. The resulting α values at different fuel concentrations are summarized in **Figure 4-3C** and **Figure S4-2**. Noteworthy, there is a clear trend toward lower α at lower fuel concentration. In the absence of fuel, the α value for coacervates-in-GUVs was 0.85, indicating constrained motion (sub-diffusion); in comparison, fitting of MSD plots of coacervates in bulk solution, in absence of fuel (**Figure 4-2A**), resulted in an α of 1.00 (normal diffusion). This further confirmed that motion behaviour was altered by confinement imposed by the GUV membrane. When the hydrogen peroxide concentration increased, α values steadily

increased and reached 1.01 at 3.4% v/v H_2O_2 (**Figure 4-3C**). Such increase in α indicated a transition from sub-diffusion toward normal diffusion upon addition of fuel, which means that the autonomous motion of the particles was able to compensate for the confinement effect. In addition, the translational diffusion coefficient (D_T) was obtained by fitting MSD profiles with the equation $MSD = 4D_T\Delta t$. By applying this formula, we obtained a two-fold increase in D_T when the H_2O_2 concentration increased from 0% to 0.85% (**Figure 4-3D**). A further increase in D_T at higher fuel concentration reflects the enhanced self-propulsion of coacervates under confinement. Altogether, these results indicated an enhanced self-propulsion and crossover from sub-diffusive toward normal diffusion of active particles in GUV confinement when increasing the fuel concentration.

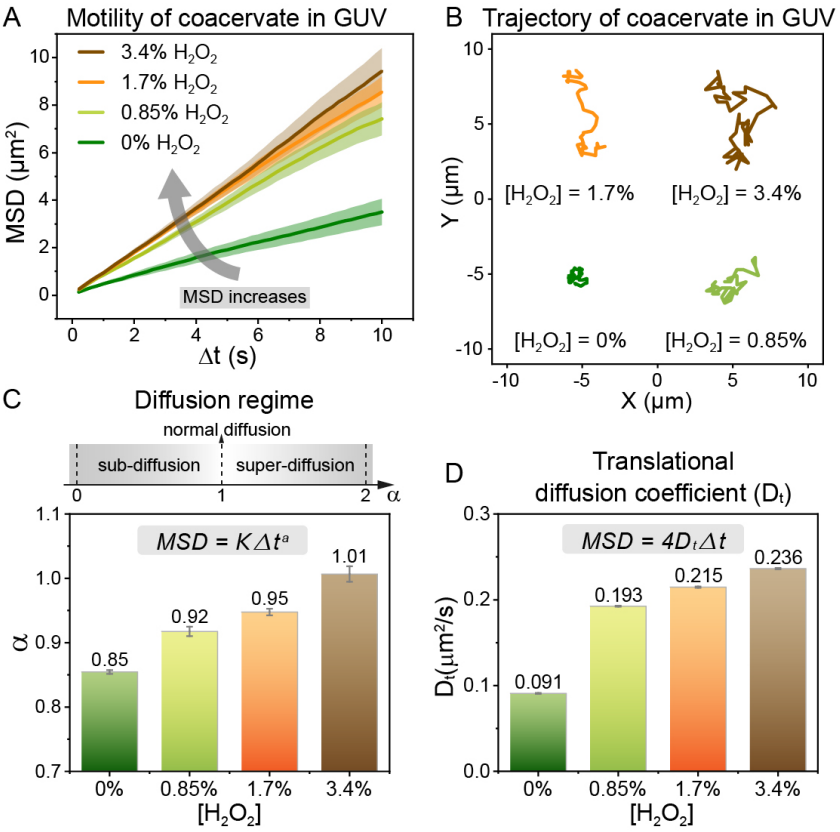

Figure 4-3 | Investigation of motion dynamics depending on fuel concentration. **A, B.** MSD profiles and trajectories of CAT-coacervates in GUVs with different hydrogen peroxide concentrations. Higher fuel concentration resulted in an increased MSD and expanded trajectory. **C.** Diffusion regime indicated by the anomalous exponent α. With $[H_2O_2]$ rising from 0% to 3.4%, α increased from 0.85 to 1.01, suggesting

a transition from sub-diffusion to normal diffusion. **D.** Translational diffusion coefficient values, at different fuel concentrations.

4.5 Motion dynamics of coacervates in GUVs depending on GUV size

Subsequently, we investigated the correlation between compartment size (i.e., GUV diameter) and motility of the confined active particles. Our hypothesis was that smaller GUVs would display a more pronounced confinement effect as the hydrodynamic interaction between coacervates and the membrane would be increased. GUVs assembled by the droplet transfer method show a relatively wide size distribution (**Figure S4-3**) – thus, we set out to analyse coacervate motion in GUVs categorized in three different diameter groups: small (14-24 µm), medium (25-34 µm) and large GUVs (>34 µm). We compared trajectories, the anomalous diffusion exponent (α) and diffusion coefficient (D_T) of the different size groups (**Figure 4-4** and **Figure S4-2**) at different fuel concentrations. Indeed, as depicted in representative trajectories in **Figure 4-4B**, coacervates in small GUVs were more prone to be in close proximity of the GUV membrane in their path, whereas coacervates in larger GUVs had more space to diffuse around, being less restrained in their movement. This observation correlated with the extracted α and D_T values (**Figure 4-4C, D**). At all fuel concentrations, a positive correlation between α and GUV size was observed, with a sub-diffusion regime in smaller GUVs and normal diffusion in larger GUVs at 3.4% v/v H_2O_2. A similar trend was observed for D_T, indicating a more effective propulsion of coacervates in larger GUVs. Noteworthy, for the small size group (14-24 µm), α and D_T increased when the concentration of H_2O_2 increased from 0% to 0.85% v/v; a further increase in fuel concentration did not alter both values. In contrast, for medium (25-34 µm) and large GUV (>34 µm) sizes, we observed a continuous increase in α and D_T from 0% to 3.4% v/v H_2O_2. Thus, under the investigated conditions, small GUVs (14-24 µm) severely restricted the motility of coacervates to the point that enhanced motion reached its limit and additional chemical energy could not be converted into additional motion. Altogether, these results indicate that a decrease in GUV compartment size correlates with a decrease in the motility of active particles.

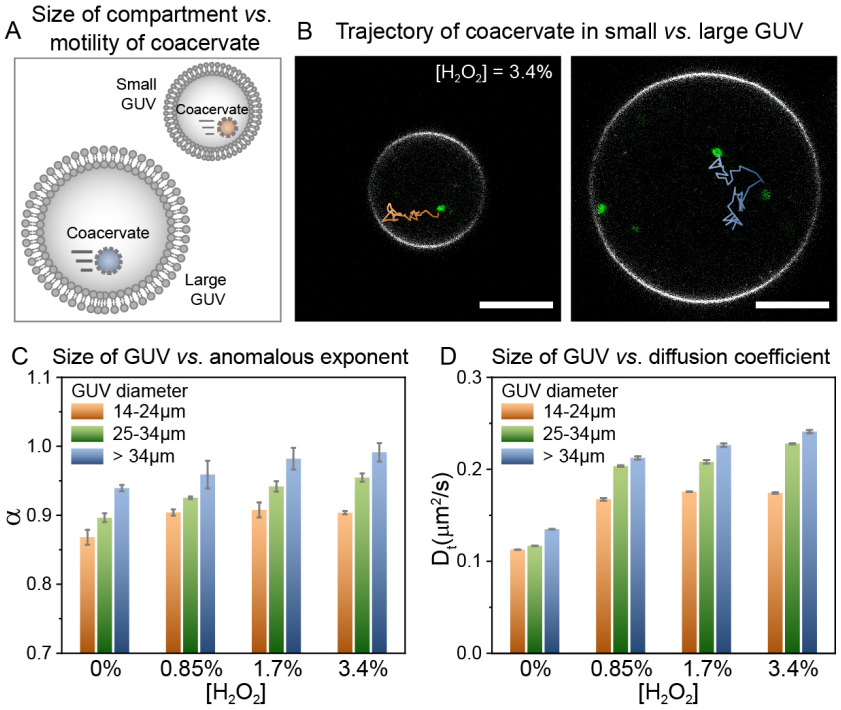

Figure 4-4 | Investigation of motion dynamics depending on the compartment size. **A.** Schematic illustration of coacervates in small and large GUVs. **B.** Trajectories of coacervates in small and large GUVs with $[H_2O_2]$ of 3.4%. Bright field tracking is overlaid on top of confocal images of coacervates in GUVs. Scale bars represent 10 μm. **C, D.** Anomalous exponent and diffusion coefficient depending on the GUV size, at different fuel concentrations. For each size group, 10 – 20 coacervates were analysed at each $[H_2O_2]$. Data in C and D are represented as mean ± SD.

4.6 Motion dynamics of coacervates in GUVs depending on coacervates concentration

Finally, we set out to investigate if differences in the relative concentration of coacervates per compartment could influence their motile properties. We hypothesized that the behaviour of active particles could be heavily affected by the presence of other active particles in their surroundings due to, for example, potential proximal particle-particle interactions. It would be of interest to experimentally validate this hypothesis to know if the concentration of active particles should be considered in future theoretical models. Therefore, we carried out experiments acquiring z-stacks of coacervates in GUVs (by confocal microscopy) prior to recording the motion of the compartmentalized particles (by bright field microscopy, upon addition of 0.85% as fuel). In all cases, 45

images along the z-axis were captured, revealing fluorescent signals of coacervates located at different planes. A circular ROI area (same size as the GUV) was selected for each frame, and grey value measurements (for fluorescence intensity) were performed for that ROI area of the whole confocal z stack (45 images). Then, the total fluorescence (sum of the 45 planes) of each GUV (N = 40) was used as an estimation of their relative coacervate concentration (**Figure 4-5**).

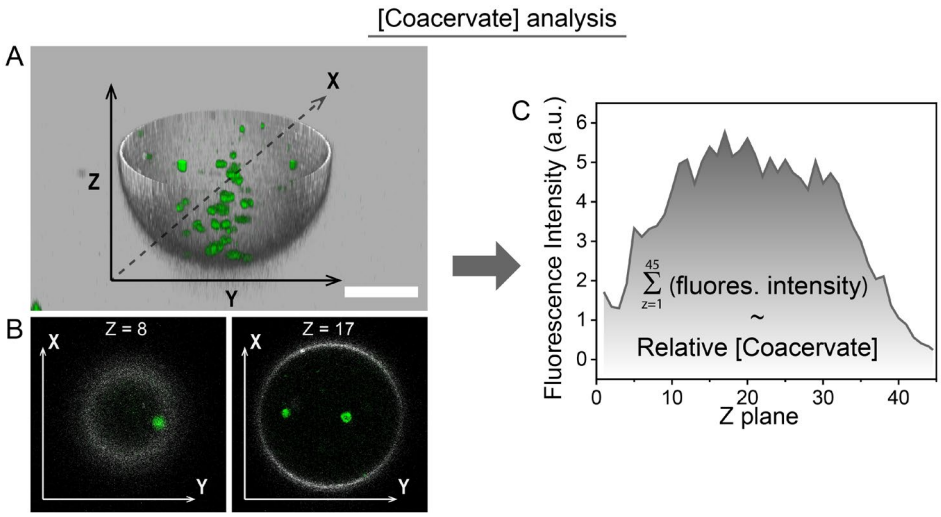

Figure 4-5 | Analysis procedure of the concentration of coacervates in GUVs. **A.** Reconstructed 3D image of coacervates (green fluorescence) in a GUV (grey fluorescence) from a confocal image stack along the z-axis. **B.** Representative confocal images used to estimate coacervate concentration with different z-position from one confocal image stack. **C.** Representative fluorescence intensity across z axis of coacervates in one GUV. Y axis stands for fluorescence intensity of coacervates obtained from one single image out of 45 z images in one confocal image stack. The total fluorescence (sum of 45 fluorescence intensity from 45 z planes) of each GUV (N = 40) was used as an estimation of their relative coacervate concentration, correlated to relative [Coacervate].

As depicted in **Figure 4-6B**, most GUVs had a relative coacervate concentration within a range of 100-175 arbitrary units (a.u.), yet we observed some heterogeneity with a fraction of GUVs located above (>175 a.u., high concentration) and below this range (<100 a.u., low concentration). Interestingly, when we extracted the motion of coacervates for each group, we found larger MSD values for confined coacervates of the low coacervate concentration group (at 10 s, MSD = 9.5 ± 1.0 μm^2), as compared to the medium (at 10 s, 8.3 ± 1.0 μm^2) and high concentration group (at 10 s, 5.6 ± 1.5 μm^2; significant difference with $p<0.05$ compared to the low conc. group) (**Figure 4-6C**). Accordingly, these data

suggests that active particle motion in confinement is affected by the overall particle concentration, in a way that relatively high concentrations result in decreased motion which could be attributed to a distortion of the product gradient field by surrounding particles.

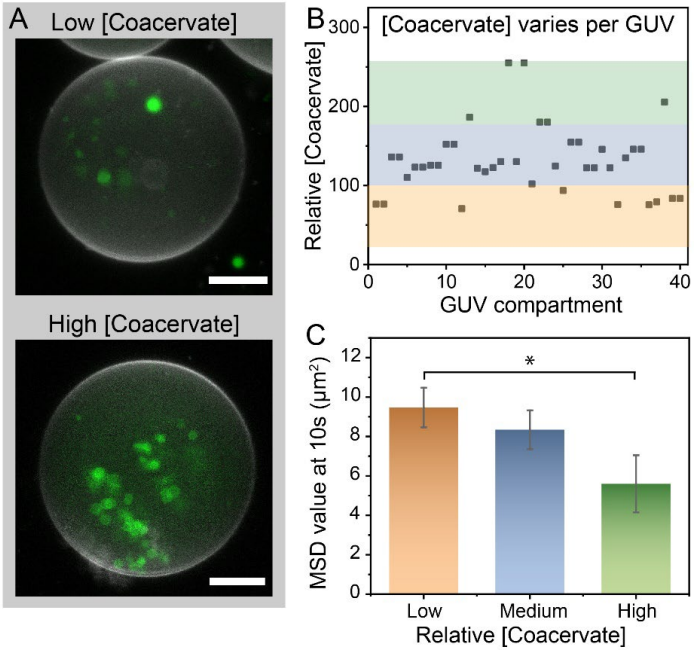

Figure 4-6 | Investigation of coacervate concentration and its effect on motion dynamics. **A.** Projection of confocal image stacks of 2 representative GUVs with high and low coacervate concentration. Scale bar represents 10 μm. **B.** 40 GUVs were analysed using confocal image stacking, to determine the relative [Coacervate]. The coacervate concentrations were (arbitrarily) grouped in three regions: the [Coacervate] lower than 100 a.u. was denoted as low, [Coacervate] between 100 and 175 a.u. was denoted as medium and [Coacervate] higher than 175 a.u. was denoted as high. **C.** With 0.85% hydrogen peroxide as fuel, MSD values of coacervate motors in a time frame of 10 seconds were categorized into the three [Coacervate] groups: low, medium and high. Statistical significance between conditions is indicated by the asterisk (*$p<0.05$).

4.7 Discussion

Our results reveal several interesting effects about the behaviour of active particles within 3D confinement. First, the motion of such compartmentalized particles is decreased as compared to the same particles free in solution. Furthermore, compartmentalized particles move in a sub-diffusion regime and the presence of fuel compensates for the confinement effect and enhances motility toward normal diffusion.

In contrast, the same non-compartmentalized particles move under Brownian motion in the absence and with (super diffusion) ballistic motion in the presence of fuel. Thirdly, the size of the compartment matters, with a stronger sub-diffusive effect (i.e., restricted motion) in smaller compartments. Finally, particles are influenced by the relative concentration of peers in their surroundings, with higher concentrations leading to a decreased motion.

It has been theoretically proposed[34-35] that there are two competing phenomena that influence the motion of swimmer particles in confinement: (i) the hydrodynamic effect: the velocity of fluid flow diminishes to zero toward the confinement wall (so called "no-slip condition", **Figure 4-7A**), which results in particles experiencing a viscous fluid drag and a diminished motion; and (ii) the phoretic effect: the confinement boundary affects the transport of product molecules, leading to a local increase of the product gradient field, resulting in increased motion. As mentioned above, our catalytically active particles move by self-diffusiophoresis, and the product molecule gradient is the key driving factor for self-propulsion. Among the two competing effects (hydrodynamic effect and phoretic effect), our findings suggest that the decelerating hydrodynamic effect is the dominating one for our chemically fueled swimmers, as we see an overall decrease in motion upon confinement. In fact, when there is no product gradient (i.e., in the absence of fuel and therefore the phoretic effect can be ruled out), the difference in motion of non-compartmentalized (Brownian) vs. compartmentalized particles (sub-diffusive) confirms that the hydrodynamic effect influences motion. Addition of fuel leads to the enhanced propulsion of the particles, which partially counteracts the hydrodynamic effect, yet motion is still partially restricted as compared to their non-compartmentalized counterparts. Additionally, our results also indicate that active particles in smaller compartments experience a larger hydrodynamic drag (i.e., more restricted motion). These findings are in agreement with other reports which describe a deceleration of particles near solid surfaces and in microfluidic channels.[31, 34] In contrast, Popescu and co-workers theoretically predicted an increase in velocity for a diffusiophoretic motor in a spherical (impermeable) compartment,[35] caused by the phoretic effect and despite the opposing hydrodynamic drag caused by the confinement boundaries. However, only impermeable confining walls were considered in their study, in which case the phoretic effect is more pronounced (by preventing the equilibration of the product gradient). Our phospholipid vesicles are highly permeable to oxygen and therefore the phoretic effect is expected to be mitigated in our system (**Figure 4-7**). The contradiction between their

theory and our experimental results can therefore be explained by the semi-permeability of the GUV membrane.

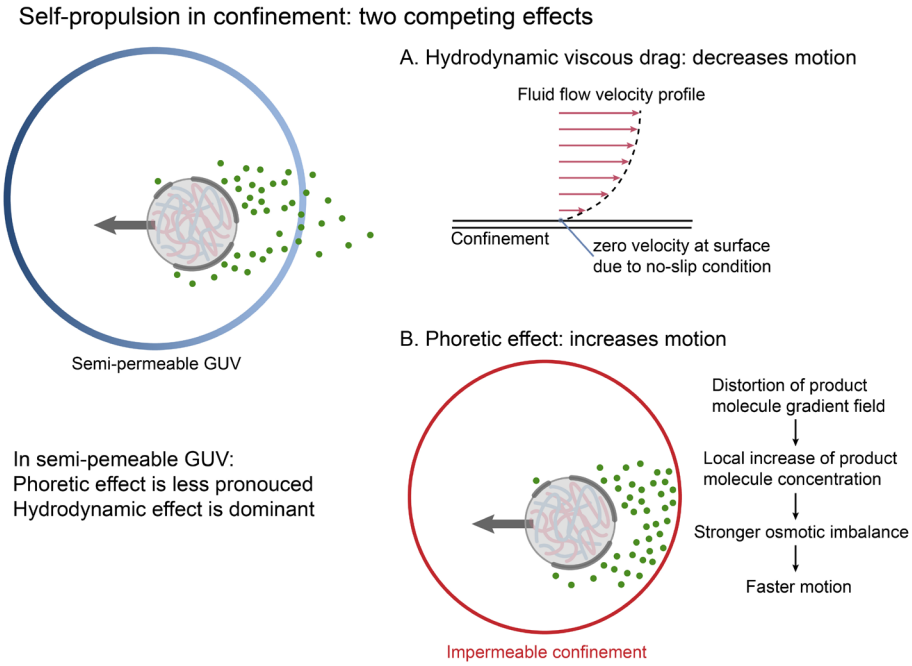

Figure 4-7 | Self-propulsion of self-diffusiophoretic coacervates in GUV confinement. **A.** No-slip condition of fluid at the confining boundary. The slowdown of fluid is transferred to active coacervates suspended in the fluid, leading to a decrease in motion. **B.** Impermeable confinement distorts the product molecule gradient field and increases local product concentration, leading to an increase in motion. However, semi-permeable GUVs alleviate the distortion of the product molecule gradient field, resulting in the decelerating hydrodynamic effect being the dominant force.

4.8 Conclusions

In conclusion, we have presented a study about the confined motion dynamics of catalytically active particles in cell-sized lipid vesicles. The fabrication methodology, based on the direct encapsulation of pre-formed particles during GUV formation, is versatile and could be extended to the study of other active particles (e.g., light-propelled motors). We observed that the confinement hinders the motion of coacervates and results in a sub-diffusion regime. Interestingly, addition of chemical fuel changes the behaviour of coacervates inside GUVs toward normal diffusion and counteracts the confinement effect. Furthermore, we determined that the confinement effect correlates with the

compartment size, with more restricted motion in smaller compartments. Finally, we observed that the overall internal coacervate concentration influences motion dynamics. These results all are in line with theoretical models that predict a leading role for the hydrodynamic effect in confined motion. Our study highlights the importance of considering the dynamics of active matter in confinement, such as in cell-like compartments, and provides a versatile platform to assess experimentally this feature of motile systems.

Experimental section

Materials

All materials were used as received unless otherwise stated. Catalase (from bovine liver), sulfo-dibenzocyclooctyne-NHS ester (DBCO-NHS) and 30% hydrogen peroxide solution were obtained from Sigma-Aldrich. Hydrogen peroxide solutions used for motility experiments were prepared by sequential dilutions of 30% hydrogen peroxide solution. Sulfo-Cyanine5 NHS ester was obtained from Lumiprobe. Lipids for GUV assembly: 1,2-dioleoyl-*sn*-glycero-3-phosphocholine (DOPC), 1-palmitoyl-2-oleoyl-glycero-3-phosphocholine (POPC), 1,2-distearoyl-*sn*-glycero-3-phosphoethanolamine-*N*-[biotinyl(polyethylene glycol)-2000] (DSPE-PEG), and 1,2-dioleoyl-*sn*-glycero-3-phosphoethanolamine-N-(lissamine rhodamine B sulfonyl) (ammonium salt) (DOPE-RhB) were provided by Avanti Polar Lipids. Paraffin oil (0.86 g/cm^3 at 20 °C) was from JT Baker. Cholesterol, glucose, sucrose, bovine serum albumin (BSA), and alpha-hemolysin (αHL) from *Staphylococcus aureus* were purchased from Sigma-Aldrich. Modified amyloses, polymers and modified catalase were prepared as described in Chapter 2.

Preparation of giant unilamellar vesicles (GUVs) with encapsulated coacervates

Our protocol for the preparation of GUVs is based on the droplet transfer method.[42] In close collaboration with Dr. Antoni Llopis-Lorente , lipid stock solutions were prepared in chloroform and stored at -20 °C until use. Lipid solution aliquots were taken and mixed with 200 µL of paraffin oil to obtain a lipid mixture containing DOPC, POPC and cholesterol in a molar ratio of 35/35/30 (10 mM total concentration). In addition, 1% of DSPE-PEG (to prevent GUV aggregation) and 0.06% of DOPE-RhB (for membrane labelling) were also incorporated. Firstly, the lipid mixture in paraffin was heated at 80 °C for 30 min and cooled on ice for 10 min. Next, 20 µL of inner phase solution (PBS 0.8X containing the as-made coacervates, 200 mM sucrose, pH 7.4) was emulsified in the 200 µL of lipid solution by strong vortexing for 25 s while turning the reaction tube to prevent sedimentation of the water droplet. Thereafter, the emulsion was incubated on ice for 10 min. Subsequently, the mixture was layered on top of 150 µL of pre-cooled outer phase (PBS 0.8X, 200 mM glucose, pH 7.4) solution in a 1.5 mL plastic tube and immediately centrifuged at 4 °C for 20 min at 3300 rcf. GUVs were harvested by puncturing the tube at the position of the GUV pellet and dripping the aqueous phase. To remove any non-encapsulated material, GUVs were pelleted by centrifugation at 1500 rcf for 2 min after which the supernatant was replaced with 40 µL fresh outer phase, which was repeated twice.

For alpha-hemolysin insertion, GUVs were incubated with 10 µg mL^{-1} of alpha-hemolysin for at least 15 min prior to motility studies.

Confocal imaging of coacervates in GUVs

Confocal laser scanning microscopy (Leica TCS SP8) was used to capture images of catalase-coacervates in GUVs with a 638 nm laser line (for Cy5) and a 552 nm laser line (for DOPE-RhB) using a 63×, 1.20 NA water immersion objective. The pinhole was set to 1 Airy Unit (156 µm). For confocal z stacks, 45 images per GUV per laser line were taken to reconstitute 3D images.

Motility experiments and data analysis

Experimental chamber:

A simple experimental chamber was designed and prepared to minimize side effects that could be mistaken as self-propulsion, such as drift or solution evaporation. This chamber was made from two glass microscopy slides spaced by two pieces of autoclave tape. Autoclave tape was first attached to a larger glass slide on two ends, followed by the addition of sample in the middle, and capping by a smaller glass slide.

Optical recording:

The videos of coacervate motion were recorded using a bright-field camera (DFC7000T) on a confocal laser scanning microscope (Leica TCS SP8). A 63× water immersion objective was used for this recording. The coacervates in GUV suspension and the enzyme substrate (hydrogen peroxide) were first mixed thoroughly and immediately added to the chamber. The recording (5 fps, > 60 s per recording) started shortly after. The highest hydrogen peroxide concentration after mixing was set to 3.4%. This concentration was chosen to avoid oxygen bubble generation that could disturb the liquid inside the chamber and mask self-propulsion. The sample in the experimental chamber was replaced at least every 5 min to maintain the same substrate concentration.

Data analysis of motion:

A tailor-made Python script (same as the one used in Chapter 3) was used to track the coacervates and obtain the mean square displacement (MSD). MSD is a measure of deviation of the position of a particle with respect to its initial position over time. It is commonly used to analyze the dynamics of self-propelled particles and is calculated as below in 2D projection:

$$MSD\ (t) = \langle (\vec{x}(t) - \vec{x}\ (0))^2 \rangle,$$

where $\vec{x}(0)$ is the initial position of the coacervate, and $\vec{x}(t)$ is the position of the coacervate when time is t. Then the obtained MSD was plotted against the time interval Δt.

Statistical analysis:

MSD curves were obtained by averaging data collected from 40 coacervates each condition, and are presented as mean ± SEM.

To obtain the anomalous exponent α and translational diffusion coefficient D_T, MSD curves were fitted with an exponential model MSD $= K\Delta t^{\alpha}$ and a linear model MSD $= 4D_T\Delta t$, respectively. Both exponential model and linear model fit the experimental data well with R^2 higher than 0.99. **Figure S4-4** shows the fitted curves. Data in histograms displaying α and D_T are represented as mean ± SD.

Supporting Information

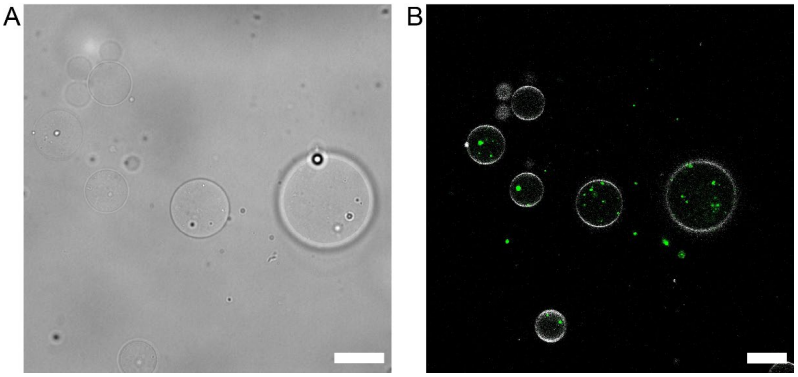

Figure S4-1 | CAT-coacervates were successfully encapsulated in GUVs without compromising GUV integrity. A) Bright-field image of coacervates-in-GUVs. B) Confocal image (Green: catalase which was modified with Cyanine 5, grey: RhB-DOPC as marker of the lipid membrane) of coacervates-in-GUVs. Scale bar represents 20 µm.

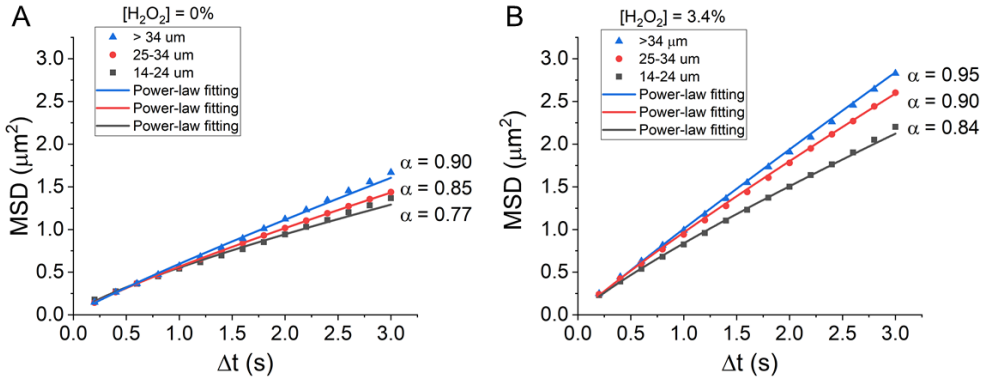

Figure S4-2 | Motility profile of CAT-coacervate motors in GUVs with $[H_2O_2]$ of 0% (A) and 3.4% (B) with different GUV compartment size. An increase in the MSD curve and α was observed in larger GUV compartments.

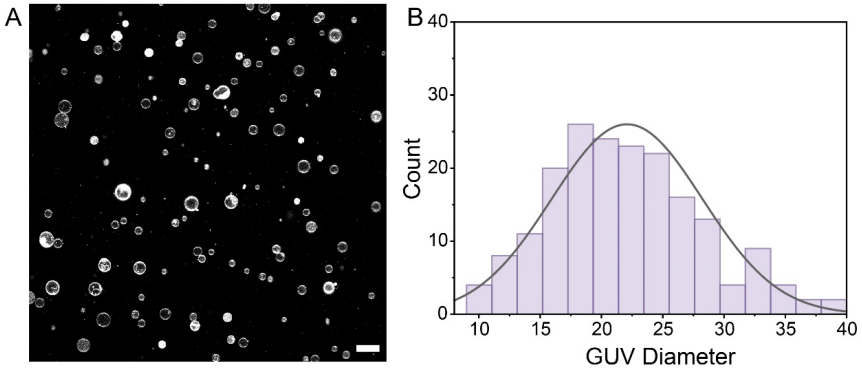

Figure S4-3 | GUV size distribution. A) Confocal image of GUVs (with RhB-DOPC as marker) (A). Scale bar represents 50 µm. B) Histogram analysis of confocal microscopy images of GUVs showing an average GUV diameter of 22.1 ± 6.2 µm.

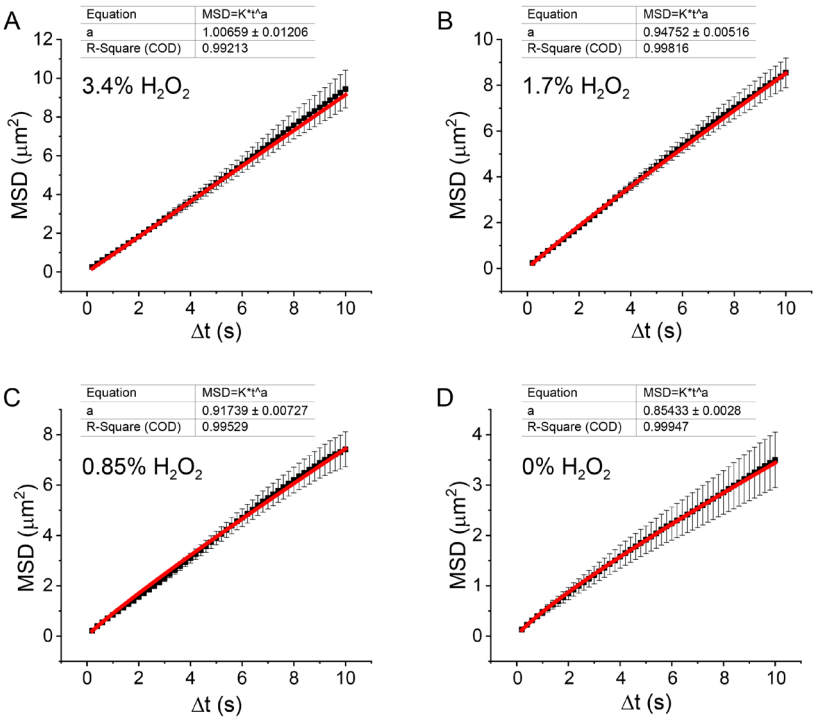

Figure S4-4 | Statistical analysis of anomalous exponent α by fitting MSD curves with equation MSD = $K\Delta t^{\alpha}$. Black curves with error bars represent experimental MSD curves (mean ± SEM, sample number = 40), and red curves represent fitted curves.

Acknowledgements

Dr. Antoni Llopis-Lorente is thanked for GUV preparation and insightful discussions.

References

[1] Sánchez, S.; Soler, L.; Katuri, J., Chemically powered micro - and nanomotors. *Angew. Chem., Int. Ed.* **2015,** *54* (5), 1414-1444.

[2] Robertson, B.; Huang, M.-J.; Chen, J.-X.; Kapral, R., Synthetic Nanomotors: Working Together through Chemistry. *Acc. Chem. Res.* **2018,** *51* (10), 2355-2364.

[3] Esteban-Fernández de Ávila, B.; Gao, W.; Karshalev, E.; Zhang, L.; Wang, J., Cell-Like Micromotors. *Acc. Chem. Res.* **2018,** *51* (9), 1901-1910.

[4] Ren, L.; Wang, W.; Mallouk, T. E., Two Forces Are Better than One: Combining Chemical and Acoustic Propulsion for Enhanced Micromotor Functionality. *Acc. Chem. Res.* **2018,** *51* (9), 1948-1956.

[5] Bartelt, S. M.; Steinkühler, J.; Dimova, R.; Wegner, S. V., Light guided motility of a minimal synthetic cell. *Nano Lett.* **2018**.

[6] Wang, S.; Wu, N., Selecting the swimming mechanisms of colloidal particles: bubble propulsion versus self-diffusiophoresis. *Langmuir* **2014,** *30* (12), 3477-3486.

[7] Shao, J.; Abdelghani, M.; Shen, G.; Cao, S.; Williams, D. S.; Van Hest, J. C., Erythrocyte membrane modified janus polymeric motors for thrombus therapy. *ACS nano* **2018,** *12* (5), 4877-4885.

[8] Kumar, B. V. V. S. P.; Patil, A. J.; Mann, S., Enzyme-powered motility in buoyant organoclay/DNA protocells. *Nat. Chem.* **2018,** *10* (11), 1154-1163.

[9] Dey, K. K.; Zhao, X.; Tansi, B. M.; Mendez-Ortiz, W. J.; Cordova-Figueroa, U. M.; Golestanian, R.; Sen, A., Micromotors Powered by Enzyme Catalysis. *Nano Lett.* **2015,** *15* (12), 8311-5.

[10] Sengupta, S.; Patra, D.; Ortiz-Rivera, I.; Agrawal, A.; Shklyaev, S.; Dey, K. K.; Cordova-Figueroa, U.; Mallouk, T. E.; Sen, A., Self-powered enzyme micropumps. *Nat. Chem.* **2014,** *6* (5), 415-22.

[11] Sengupta, S.; Dey, K. K.; Muddana, H. S.; Tabouillot, T.; Ibele, M. E.; Butler, P. J.; Sen, A., Enzyme Molecules as Nanomotors. *J. Am. Chem. Soc.* **2013,** *135* (4), 1406-1414.

[12] Paxton, W. F.; Kistler, K. C.; Olmeda, C. C.; Sen, A.; St. Angelo, S. K.; Cao, Y.; Mallouk, T. E.; Lammert, P. E.; Crespi, V. H., Catalytic Nanomotors: Autonomous Movement of Striped Nanorods. *J. Am. Chem. Soc.* **2004,** *126* (41), 13424-13431.

[13] Arqué, X.; Romero-Rivera, A.; Feixas, F.; Patiño, T.; Osuna, S.; Sánchez, S., Intrinsic enzymatic properties modulate the self-propulsion of micromotors. *Nat. Commun.* **2019,** *10* (1), 2826.

[14] Ghosh, S.; Mohajerani, F.; Son, S.; Velegol, D.; Butler, P. J.; Sen, A., Motility of Enzyme-Powered Vesicles. *Nano Lett.* **2019,** *19* (9), 6019-6026.

[15] Wang, L.; Lin, Y.; Zhou, Y.; Xie, H.; Song, J.; Li, M.; Huang, Y.; Huang, X.; Mann, S., Autonomic Behaviors in Lipase - Active Oil Droplets. *Angew. Chem.* **2019,** *131* (4), 1079-1083.

[16] Ma, X.; Jang, S.; Popescu, M. N.; Uspal, W. E.; Miguel-López, A.; Hahn, K.; Kim, D.-P.; Sánchez, S., Reversed janus micro/nanomotors with internal chemical engine. *ACS nano* **2016,** *10* (9), 8751-8759.

[17] Brooks, A. M.; Tasinkevych, M.; Sabrina, S.; Velegol, D.; Sen, A.; Bishop, K. J. M., Shape-directed rotation of homogeneous micromotors via catalytic self-electrophoresis. *Nat. Commun.* **2019,** *10* (1), 495.

[18] Kline, T. R.; Paxton, W. F.; Mallouk, T. E.; Sen, A., Catalytic nanomotors: remote - controlled autonomous movement of striped metallic nanorods. *Angew. Chem., Int. Ed.* **2005,** *44* (5), 744-746.

[19] Zhao, G.; Sanchez, S.; Schmidt, O. G.; Pumera, M., Micromotors with built-in compasses. *Chem. Commun.* **2012,** *48* (81), 10090-10092.

[20] Rikken, R. S.; Nolte, R. J.; Maan, J. C.; van Hest, J. C.; Wilson, D. A.; Christianen, P. C., Manipulation of micro-and nanostructure motion with magnetic fields. *Soft Matter* **2014,** *10* (9), 1295-1308.

[21] Yu, N.; Lou, X.; Chen, K.; Yang, M., Phototaxis of active colloids by self-thermophoresis. *Soft Matter* **2019,** *15* (3), 408-414.

[22] Somasundar, A.; Ghosh, S.; Mohajerani, F.; Massenburg, L. N.; Yang, T.; Cremer, P. S.; Velegol, D.; Sen, A., Positive and negative chemotaxis of enzyme-coated liposome motors. *Nat. Nanotechnol.* **2019,** *14* (12), 1129-1134.

[23] Ji, Y.; Lin, X.; Wu, Z.; Wu, Y.; Gao, W.; He, Q., Macroscale Chemotaxis from a Swarm of Bacteria - Mimicking Nanoswimmers. *Angew. Chem., Int. Ed.* **2019,** *58* (35), 12200-12205.

[24] Popescu, M. N.; Uspal, W. E.; Bechinger, C.; Fischer, P., Chemotaxis of active Janus nanoparticles. *Nano Lett.* **2018,** *18* (9), 5345-5349.

[25] Donaldson, J. G.; Schall, P.; Rossi, L., Magnetic Coupling in Colloidal Clusters for Hierarchical Self-Assembly. *ACS Nano* **2021**.

[26] Ji, F.; Jin, D.; Wang, B.; Zhang, L., Light-Driven Hovering of a Magnetic Microswarm in Fluid. *ACS Nano* **2020**.

[27] Ahmed, D.; Sukhov, A.; Hauri, D.; Rodrigue, D.; Maranta, G.; Harting, J.; Nelson, B. J., Bioinspired acousto-magnetic microswarm robots with upstream motility. *Nature Machine Intelligence* **2021,** *3* (2), 116-124.

[28] Vutukuri, H. R.; Lisicki, M.; Lauga, E.; Vermant, J., Light-switchable propulsion of active particles with reversible interactions. *Nat. Commun.* **2020,** *11* (1), 2628.

[29] Palacci, J.; Sacanna, S.; Steinberg, A. P.; Pine, D. J.; Chaikin, P. M., Living Crystals of Light-Activated Colloidal Surfers. *Science* **2013,** *339* (6122), 936.

[30] Ibrahim, Y.; Liverpool, T. B., The dynamics of a self-phoretic Janus swimmer near a wall. *EPL (Europhysics Letters)* **2015,** *111* (4), 48008.

[31] Xiao, Z.; Wei, M.; Wang, W., A Review of Micromotors in Confinements: Pores, Channels, Grooves, Steps, Interfaces, Chains, and Swimming in the Bulk. *ACS Appl. Mater. Interfaces* **2019,** *11* (7), 6667-6684.

[32] Das, S.; Garg, A.; Campbell, A. I.; Howse, J.; Sen, A.; Velegol, D.; Golestanian, R.; Ebbens, S. J., Boundaries can steer active Janus spheres. *Nat. Commun.* **2015,** *6*, 8999.

[33] Yu, H.; Kopach, A.; Misko, V. R.; Vasylenko, A. A.; Makarov, D.; Marchesoni, F.; Nori, F.; Baraban, L.; Cuniberti, G., Confined Catalytic Janus Swimmers in a Crowded Channel: Geometry-Driven Rectification Transients and Directional Locking. *Small* **2016,** *12* (42), 5882-5890.

[34] Yang, F.; Qian, S.; Zhao, Y.; Qiao, R., Self-Diffusiophoresis of Janus Catalytic Micromotors in Confined Geometries. *Langmuir* **2016,** *32* (22), 5580-5592.

[35] Popescu, M. N.; Dietrich, S.; Oshanin, G., Confinement effects on diffusiophoretic self-propellers. *The Journal of Chemical Physics* **2009,** *130* (19), 194702.

[36] Liu, C.; Zhou, C.; Wang, W.; Zhang, H. P., Bimetallic Microswimmers Speed Up in Confining Channels. *Phys. Rev. Lett.* **2016,** *117* (19), 198001.

[37] Khezri, B.; Novotný, F.; Moo, J. G. S.; Nasir, M. Z. M.; Pumera, M., Confined Bubble-Propelled Microswimmers in Capillaries: Wall Effect, Fuel Deprivation, and Exhaust Product Excess. *Small* **2020,** *n/a* (n/a), 2000413.

[38] Lozano, C.; ten Hagen, B.; Löwen, H.; Bechinger, C., Phototaxis of synthetic microswimmers in optical landscapes. *Nat. Commun.* **2016,** *7* (1), 12828.

[39] Mestre, R.; Palacios, L. S.; Miguel-López, A.; Arqué, X.; Pagonabarraga, I.; Sánchez, S., Extraction of the propulsive speed of catalytic nano-and micro-motors under different motion dynamics. *arXiv preprint arXiv:2007.15316* **2020**.

[40] Mestre, R. Python-based Nano-micromotor Analysis Tool (NMAT) v.1. https://github.com/rafamestre/NMAT-nanomicromotor-analysis-tool.

[41] Metzler, R.; Jeon, J.-H.; Cherstvy, A. G.; Barkai, E., Anomalous diffusion models and their properties: non-stationarity, non-ergodicity, and ageing at the centenary of single particle tracking. *Phys. Chem. Chem. Phys.* **2014,** *16* (44), 24128-24164.

[42] Buddingh', B. C.; Elzinga, J.; van Hest, J. C. M., Intercellular communication between artificial cells by allosteric amplification of a molecular signal. *Nat. Commun.* **2020,** *11* (1), 1652.

CHAPTER 5

Hierarchical coacervate motors driven by light-activated photothermal effect

Abstract

Micro- and nano-motors driven by external stimuli, such as electric and magnetic fields, and light, are another interesting class of active materials in addition to chemically-driven motors. Such motors are able to sense and respond to distant environmental signals (i.e., external fields) by converting energy associated with these sources to mechanical power. In this chapter, we present a hierarchical motor system where motion of our cell-sized coacervate system can be driven by the action of compartmentalized light-responsive nanomotors. We find that, surprisingly, such hierarchical motor system displays positive phototaxis (moving toward the light source), whereas the individual nanomotors move away from the source of light. We systematically rule out photothermal effects as the reason for driving the motion of the coacervates, confirming that the anisotropy of the photothermal gradient is key to such motion dynamics. Furthermore, the delicate interplay between the nanomotors and their environment is attributed to the observed reversal of tactic behaviour.

5.1 Introduction

Externally driven nano- and micro-motors are a class of active materials that are propelled by external stimuli (e.g. light, acoustic or magnetic fields). [1-8] They are able to sense and respond to distant environmental signals (i.e., external fields) by converting energy associated with these sources to mechanical power. The ability to do so is reminiscent of bacterial tactic behaviour, which allows their migration to more favourable environments.[9-10] Externally driven motors have a broadened application window in cases where relatively toxic chemical fuels (e.g., hydrogen peroxide) are not allowed.[11] For instance, the decomposition of hydrogen peroxide and the accumulation of reaction products could lead to oxygen bubble generation or changes in ion strength and pH, which could hamper motor performance in confined spaces and biological environments.[11] Additionally, external fields can be more easily manipulated, which facilitates, for example, remote on/off control and navigation.[11]

Among the available external physical stimuli, photo-induced motion has attracted special attention due to its versatility and potential in biomedical applications, such as photodynamic therapy.[12-13] Furthermore, self-phoretic light-driven motors do not sacrifice their ability of individual, autonomous motion. This is in contrast with many other externally driven motors, which move collectively in response to either electric or magnetic fields. For instance, swimmers driven by a rotating magnetic field align and move into the same direction; this type of motion is not autonomous.[14] Depending on the mechanism of their motion, two types of light-driven motors can be identified; these are either photochemical or photothermal. The former type of motors generally converts photon energy into chemical gradients through, for example, photocatalytic reactions, leading to propulsion via self-diffusiophoresis or self-electrophoresis.[15-19] Besides chemical gradients, light can induce local thermal gradients around the motors through, for example, the utility of light-absorbing materials such as gold (Au).[20-22] Such motors are driven by self-thermophoresis.[23-24] Structural asymmetry is an important design of motor systems; in case of photothermal motors Janus particles with a hemispherical gold coating are often applied, of which the gold layer generates heat under red/near infrared laser irradiation due to its unique plasmonic property.[5, 12, 23-25] Self-thermophoretic Janus motors have displayed a wide variety of behaviours, including rotation,[24] schooling and swarming[3, 19] and both positive and negative phototaxis have been observed.[23, 26-27] For example, a gold-coated Janus polymersome with a diameter of around 400 nm has been reported by our group to be self-propulsive and negatively phototactic.[26] Additionally,

photothermal propulsion has been used in combination with other external stimuli, such as electric and magnetic fields, for various applications.[12, 16, 28] However, using the cooperative action of self-thermophoretic swimmers as active elements to drive a larger system has been rarely reported.

In this chapter we have developed a hierarchical motor system where light-driven nanomotors are encapsulated inside a micron-sized coacervate, to provide the artificial cell mimic with internal means to drive motility. To be able to do so, two requirements have to be fulfilled in the design of such system. First of all, the kinetic energy of the nanoswimmers must be transferred to the larger compartment to enable motion of the entire system. Secondly, since multiple nanomotors will be incorporated in a single coacervate they must work in unison to achieve a net displacement. To this end, we have employed Janus gold-coated polymersome nanomotors, which were previously reported by our group,[12] and encapsulated them inside the micron-sized coacervate system reported in Chapter 2 and 3. We have coated the polymersomes with a negatively charged polymer shell via layer-by-layer assembly to enhance electrostatic interactions between the nanomotors and the positively charged coacervate interior, as this electrostatic interaction is thought to be key for kinetic energy transfer. After hierarchical assembly, we have studied the motile features of this system in detail, and observed a remarkable positive phototactic behaviour.

5.2 Fabrication of light-driven coacervate micromotors

We started with the fabrication of gold-coated polymersomes in close collaboration with Dr. Jingxin Shao. Polymersomes were assembled from the block polymer poly(ethylene glycol)$_{45}$-*b*-polystyrene$_{210}$ (PEG-PS) through a well-documented solvent switch method (**Figure 5-1**).[29-30] In brief, PEG-PS (10 g) was first dissolved in 1 mL mixture of tetrahydrofuran/dioxane (80:20 v/v), followed by a slow addition of 1 mL Milli-Q water (up of 50% v/v) via a syringe pump at a rate of 1 mL / h. The addition of water drove the assembly of hydrophobic segments to form polymersomes, leading to a cloudy suspension which was dialyzed against Milli-Q water and purified from organic solvents. To facilitate visualization under confocal microscopy, a dye, fluorescein isothiocyanate (FITC), was sequestered in the lumen of the polymersomes during assembly. Such polymersomes were slightly negatively charged near neutral pH due to the PEG segment (ζ potential = -3 mV).

To ensure efficient encapsulation of the polymersomes in the coacervates, the polymersomes' surface charge must be considered. The encapsulation of materials by complex coacervates is largely dependent on the electrostatic interaction between the material itself and the coacervate interior, as previously demonstrated by our group,[31] although other parameters, such as size and hydrophobicity, can also have an impact on the uptake.[31-32] Although the encapsulation of similar polymersomes (also with PEG segment) in coacervates has been reported before in our group,[32] it was demonstrated that the slight negative charge on the polymersomes was not sufficient for an efficient uptake in the positively charged coacervate interior. In fact, the encapsulation efficiency of the bare polymersomes was only 3%.[32] When polymersomes were loaded with negatively charged cargo, which also affected the overall net charge of the polymersomes, encapsulation efficiency went up to 9%.[32] To increase the negative surface charge, we used a layer-by-layer (LBL) assembly technique to apply a thin layer of charged polymers around the polymersomes, as we have previously performed in our group.[29] With this method, it is possible to modulate the surface charge without changing the chemical nature of the polymersomes directly. To this end, a cationic polyelectrolyte poly(allylamine hydrochloride) (PAH) was first assembled on the surface of PEG-PS polymersomes, followed by the assembly of a second layer comprising an anionic polyelectrolyte poly(styrene sulfonate) (PSS) (**Figure 5-1**). This LBL-on-polymersome approach was successful, with PAH-polymersomes displaying a slightly positive zeta-potential of 2 mV and the final LBL polymersomes (with PSS as the outermost layer) possessing a significant negative zeta-potential of -32 mV. The last step of the gold-coated Janus polymersome fabrication process was to install asymmetry and photo-responsiveness, by depositing a thin layer of gold onto one side of the LBL polymersomes through sputter coating.

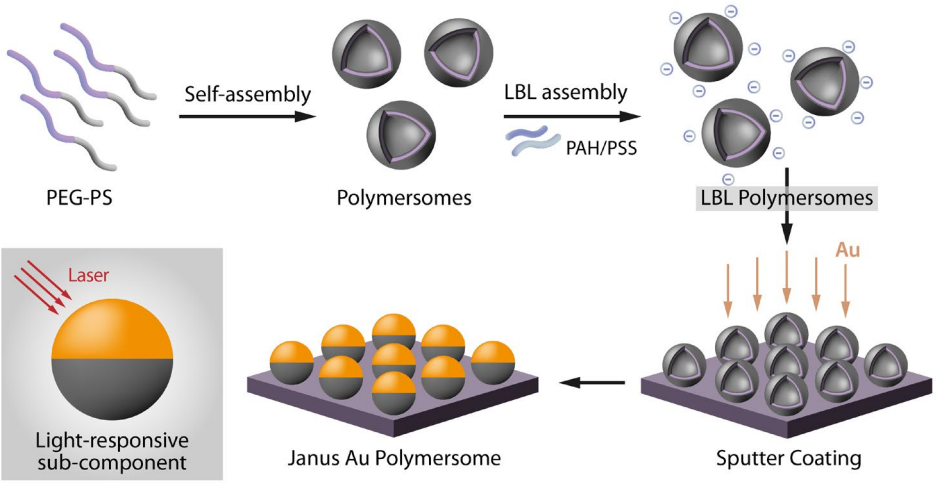

Figure 5-1 | Self-assembly of light-responsive Janus Au polymersomal sub-components. Polymersomes were assembled from PEG-PS through the solvent switch method, after which they were coated with a thin layer of charged polymers (PAH and PSS) by LBL assembly. Thereafter, a thin layer of gold was deposited on one side of the LBL polymersomes through sputter coating to generate Janus polymersomes.

The integrity and morphology of the polymersomes was confirmed by scanning electron microscopy (SEM), transmission electron microscopy (TEM) and dynamic light scattering (DLS) (**Figure 5-2**). The vesicular nature of polymersomes was clearly seen in both SEM and TEM images before and after sputter coating (**Figure 5-2A-D**), although there were several slight deformations because of the drying process during sample preparation before imaging. The size of the polymersomes remained similar (ca. 400 nm) in diameter before and after gold coating (**Figure 5-2E**) with relatively low dispersity, suggesting that sputter coating did not compromise the polymersomes' integrity. The actual presence of the gold shell and the Janus polymersome morphology were confirmed by SEM and TEM (**Figure 5-2B, D inset**), with the brighter side indicating the presence of gold by SEM and the darker side indicating gold by TEM.

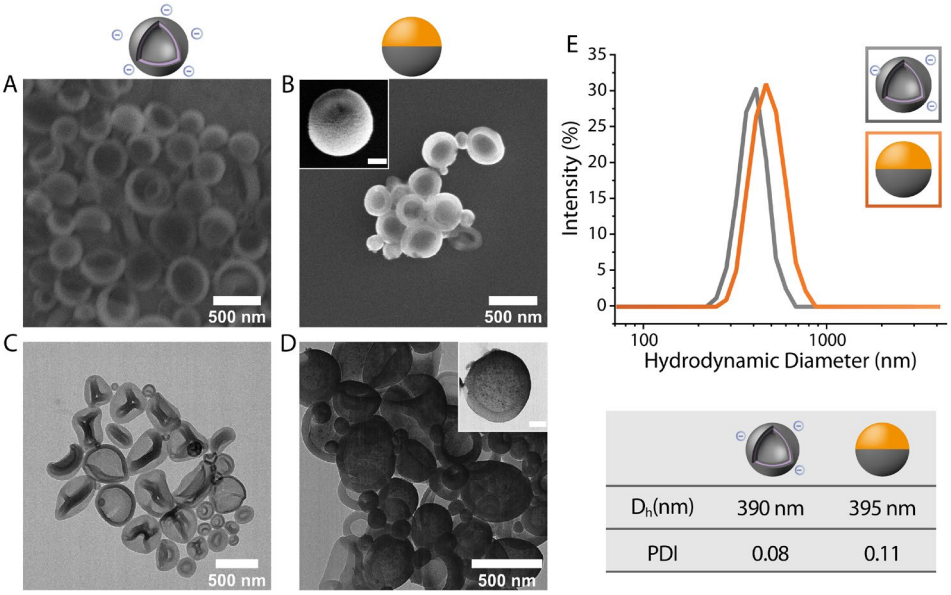

Figure 5-2 | Characterization of polymersomes. **A.** Scanning electron microscopy (SEM) image of uniform LBL polymersomes. **B.** SEM image of Janus Au polymersomes. Brighter side of the polymersome shown in the inset indicates the Au shell. (Scale bar inset: 100 nm). **C.** Transmission electron microscope (TEM) image of LBL polymersomes. **D.** TEM image of Janus Au polymersomes. Darker side of the polymersome shown in the inset indicates the Au shell (Scale bar inset: 100 nm). **E.** Polymersome size distribution by dynamic light scattering (DLS) before and after gold coating.

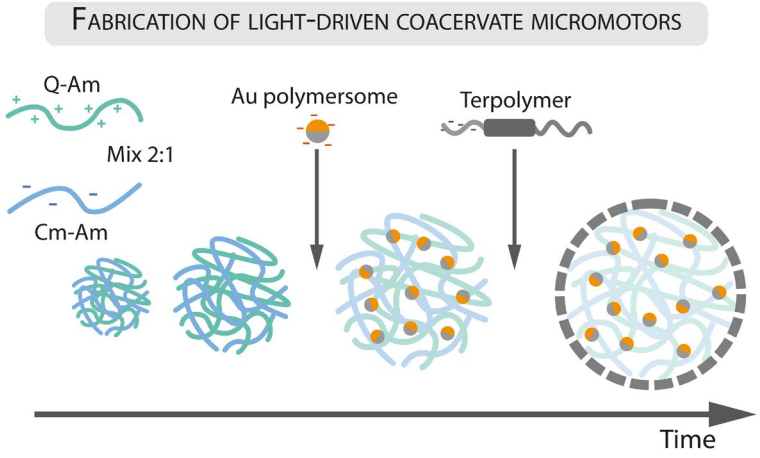

Figure 5-3 | Schematic illustration of assembly and fabrication of light-driven coacervate micromotors. Light-responsive Janus gold-coated polymersomes (Au polymersomes) were added prior to terpolymer stabilization to ensure effective encapsulation.

Having confirmed the structural integrity of the Janus gold-coated polymersomes (Au polymersomes), we set out to investigate their encapsulation in the coacervates' interior. The assembly process of the coacervates was performed in a similar way to that discussed in the previous chapters, where two oppositely charged amlyose derivatives were mixed to induce coacervation, followed by the addition of Au polymersomes before terpolymer stabilization (**Figure 5-3**). As mentioned earlier, bare PEG-PS polymersomes don't possess sufficient negative charge to be efficiently taken up by the positively charged coacervate interior, which was also confirmed by a confocal image (**Figure 5-4A**) with bare polymersomes mostly located at the periphery of the coacervates. More negatively charged LBL polymersomes were observed to be encapsulated in the interior of the coacervates (**Figure 5-4B-D**). However, some coacervates were deformed into a peanut-like shape after the addition of charged LBL polymersomes (**Figure 5-4B**). When we decreased the added volume from 20 µL to 10 µL of the LBL polymersome dispersion (2 mg/mL) to 300 µL coacervates, more coacervates retained a spherical shape (**Figure 5-4C**). When only 5 µL LBL polymersome dispersion was used, the spherical shape of coacervates was completely restored (**Figure 5-4D**). The sequestration efficiency was determined to be 15.9 ± 0.9, 14.9 ± 1.6 and 27.2 ± 3.0 % (Experimental section) for 20 µL, 10 µL and 5 µL added LBL polymersome dispersions, respectively. These sequestration efficiencies for LBL polymersomes were significantly higher than for bare polymersomes, which had a sequestration efficiency of 9.0 ±1.2 %. From these results, we determined the condition of 5 µL 2 mg/mL added LBL polymersome dispersion to be the most optimal, as the highest sequestration efficiency was achieved, and no coacervate deformation was observed, evident by the bright cyan fluorescence confirming the coacervate morphology and integrity (**Figure 5-4D**).

The deformation effect of encapsulated cargos on coacervate shape has not been observed in previous investigations where several cargos, such as proteins, DNA strands, dyes and dextran, were encapsulated.[31] Proteins can be encapsulated in coacervates with a much higher sequestration efficiency, likely due to their small size compared to polymersomes. For example, succinylated bovine serum albumin was loaded in coacervates with a sequestration efficiency of 88 ± 7%, and coacervates still retained a spherical shape (**Figure S5-2**). As such, this deformation effect could be attributed to the exclusion volume effect due to the much larger size of polymersomes (diameter = ca. 400 nm) compared to other cargos, suggesting a larger volume inside coacervate was needed

to accommodate polymersomes. This hypothesis is also in line with the observation that coacervates restored to spherical shapes with less polymersomes encapsulated.

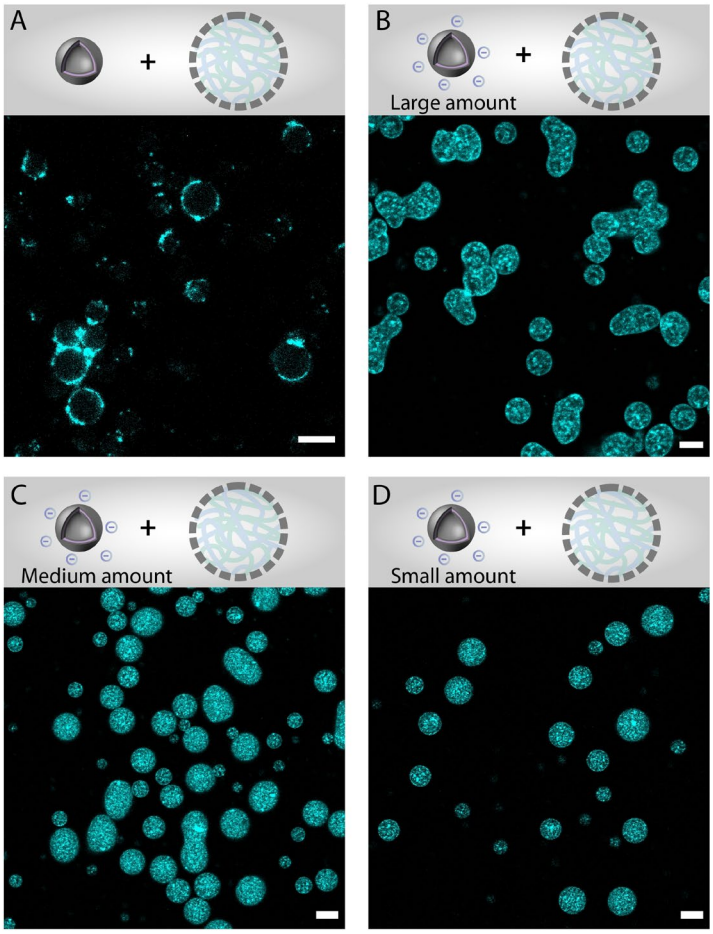

Figure 5-4 | Coacervate micromotors with encapsulated polymersomes. **A.** Coacervates with 10 µL, 2 mg/mL added bare PEG-PS polymersome dispersion. **B.** Coacervates with 20 µL, 2 mg/mL added LBL polymersome dispersion. **C.** Coacervates with 10 µL, 2 mg/mL added LBL polymersome dispersion. **D.** Coacervates with 5 µL, 2 mg/mL added LBL polymersome dispersion. Cyan: FITC in the lumen of polymersomes. Scale bars represent 10 µm.

5.3 Motility of light-activated hierarchical coacervate micromotors

With Au polymersomes effectively sequestered inside the coacervates (**Figure S5-1**), we set out to study the motion dynamics of such hierarchical coacervate motors upon irradiation with red laser light. Janus Au polymersomes have already been shown to

undergo photo-induced motility and directional movement (i.e. negative phototaxis) under the irradiation of a red or near-infrared laser due to asymmetric plasmonic heating.[12, 24] Motion of the hierarchical coacervate motors was recorded in the presence and absence of laser irradiation by bright-field microscopy. Coacervates with a diameter of 3.6 ± 1.6 μm were chosen for the motility experiments because of two reasons: firstly, larger coacervates tend to sediment quickly and a response time is needed to build self-generated thermal gradients to drive the motion, secondly, smaller coacervates used in Chapter 3 and 4 (d ~ 1.2 μm) might not be able to encapsulate enough polymersomes that can drive their motion.

To test light-driven motility of the hierarchical coacervate motors, a red laser (660nm DPSS Red Diode Laser, BeamQ) was placed on the left side of the microscope and experimental chamber. After addition of the hierarchical coacervate suspension in the chamber, the irradiation was started at the left side (**Figure 5-5C**) and the recording was initiated shortly after. For each condition, 20 – 30 coacervate motors were analysed. Upon laser irradiation (660 nm, 0.5 W/cm^{-2}) for 3 min, the hierarchical coacervate motors (with Janus Au polymersomes) underwent enhanced diffusion as compared to Brownian motion without irradiation. Mean square displacement (MSD) of the hierarchical coacervate motors increased two-fold with laser irradiation at a time interval of 20s (**Figure 5-5A**). Analysis of the trajectories also suggested a transition from Brownian motion to enhanced motion upon laser irradiation, as movement trajectories became more directional (**Figure 5-5B**). To distinguish propulsion from enhanced diffusion, first a characteristic timescale τ_R was calculated as:

$$\tau_R^{-1} = \frac{k_B T}{8\pi\eta R^3} \quad (1)$$

where $k_B T$ represents the thermal energy, η is the viscosity of the liquid suspending the particle, and R is the radius of the coacervate. For coacervates with a diameter of 3.6 μm, τ_R was calculated to be 35s. For any particle, when $\Delta t > \tau_R$, the moving direction of the particle is randomized due to the intrinsic rotational diffusion and the MSD curve should be linear.[33] However, when $\Delta t < \tau_R$, ballistic particles should display a parabolic MSD curve while diffusive particles should demonstrate a linear curve. It is evident from **Figure 5-5A** that both MSD curves were linear in time, suggesting diffusive behaviour. However, the MSD curve upon irradiation had a much larger slope, indicating enhanced diffusion. By fitting the MSD curves with:

$$MSD = 4D_{eff}\Delta t \quad (2)$$

an effective diffusion coefficient D_{eff} of the hierarchical coacervate motors upon laser irradiation was obtained to be 0.229 μm²/s, which is almost 2-fold higher than non-irradiated coacervates (D_{eff} = 0.118 μm²/s). Additionally, the experimentally obtained D_{eff} of 0.118 μm²/s is in line with the theoretical value of 0.125 μm²/s, which was calculated by:

$$D_T = \frac{k_B T}{6\pi\eta R} \quad (3)$$

confirming that the high D_{eff} of irradiated coacervates is due to their motion and not noise.

Further examination of the particle trajectories revealed that the hierarchical coacervate motors (in response to the red laser) moved towards the light source, a phenomenon known as positive phototaxis (**Figure 5-5D**). Interestingly, Janus Au polymersomes by themselves displayed negative phototaxis upon exposure to light.[12] We speculate that this disparity arises from the drastically different particle-solvent interactions when Au polymersomes are immersed in a crowded and highly-charged environment (coacervate phase). It has been previously demonstrated that thermophoresis is a material-dependent property, and significantly influenced by the interfacial properties of particle and solvent.[20-21] One study revealed that the addition of poly(ethylene glycol) to the particle solution led to a reversal of thermophoretic direction of isotropic polystyrene (PS) nanobeads.[21] In a temperature gradient, PS nanobeads migrated toward the low temperature region in water, however, upon addition of PEG, PS nanobeads reversed their direction and moved toward the high temperature region due to an altered particle-solvent interaction.[21] Similarly, such reversal of moving direction has been found in 1 μm Au-silica Janus swimmers upon addition of the surfactant Triton-X.[24] Therefore, it is plausible to hypothesize that also the coacervate phase composed of macromolecules has a great impact on polymersome/solvent interactions and on the self-thermophoretic direction of Janus Au polymersomes. Such effect is likely to contribute to the positive phototaxis of the hierarchical coacervate motors.

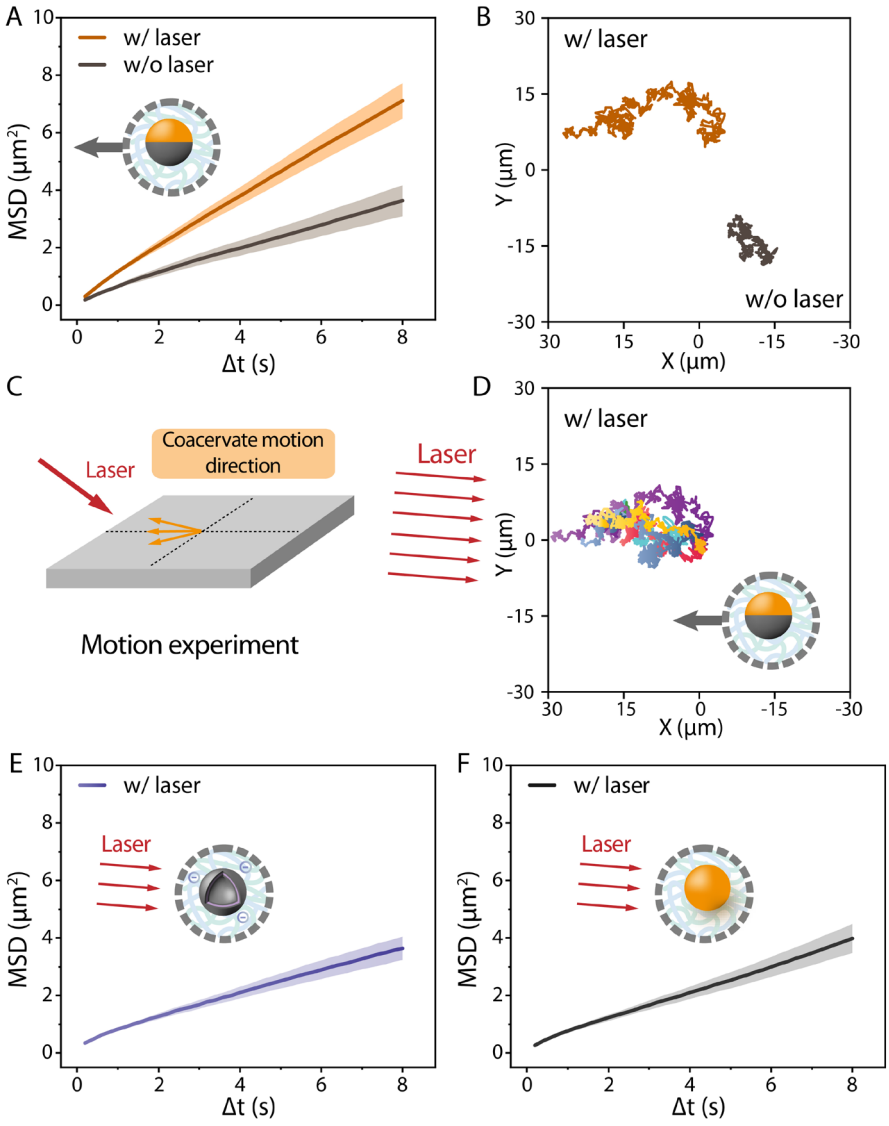

Figure 5-5 | Motility and phototaxis of hierarchical coacervate motors **A, B.** MSD curves and representative trajectories of hierarchical coacervate motors in the presence and absence of laser irradiation (660 nm, 0.5 W/cm^{-2}). **C.** Experimental setup to measure directional movement of hierarchical coacervate motors. **D.** Directional trajectories of hierarchical coacervate motors under laser radiation from the left side. **E.** MSD curve of LBL polymersome loaded coacervate motors upon irradiation (660 nm, 0.5 W/cm^{-2}). **F.** MSD curve of AuNPs loaded coacervate motors upon irradiation (660 nm, 0.5 W/cm^{-2}). MSD curves are represented as mean ± SEM.

To ensure that bulk photothermal heating was not responsible for the observed motion dynamics, symmetric PEG-PS polymersomes (5 µL, 2 mg/mL) and gold nanoparticles (AuNPs, 10 µL, d ~200 nm) were encapsulated in coacervates and motion experiments were performed upon laser irradiation (660 nm, 0.5 W/cm^{-2}) for 3 min. From our results, it is evident that both coacervate systems displayed Brownian motion (**Figure 5-5E, F**). Coacervate motors loaded with symmetric PEG-PS polymersomes or AuNPs were calculated to have a D_{eff} of 0.122 $\mu m^2/s$, and a D_{eff} of 0.127 $\mu m^2/s$, respectively. Both values were close to the Brownian diffusion coefficient of coacervates (0.118 $\mu m^2/s$). Therefore, coacervate motility is a result of the Janus Au polymersomes, which transfer their combined motile force via non-covalent interactions to the integrated system.

5.4 Conclusions

In summary, we have demonstrated the ability to design and generate hierarchical coacervate micromotors with light-activated Janus polymersomal subcomponents. We have presented the charge-mediated uptake of Janus gold-coated nanoparticles into the coacervate phase, which was proven to be the key to enhanced motion of the coacervate. Such hierarchical coacervate micromotors displayed enhanced diffusion with positive phototaxis upon irradiation with red laser light. This suggests a successful transfer of motility / phoretic drive from the nanosized engine polymersomes to the micron-sized coacervates through non-covalent interactions. Remarkably, Au polymersomes displayed negative phototaxis in bulk aqueous solution, whereas the coacervate motors demonstrated positive phototaxis. This is attentively attributed to the crowded and charged environment inside the coacervate phase, leading to different particle-solvent interactions as compared to Au polymersomes in bulk. A further step to cross-validate this hypothesis experimentally would be to load Au polymersomes in bulk coacervate solution and in a vesicular system (i.e., lipid vesicles) in which the aqueous environment is the same as in bulk, and examine the light-driven motility in these two environments. This research demonstrates that an engineering approach to complex compartmentalized systems can lead to unexpected motile behaviour. Our coacervate platform could thus facilitate a more thorough systematic investigation to further our knowledge on which aspects determine motility in micro-environments.

Experimental section

Materials

For poly(ethylene glycol)$_{45}$-b-polystyrene$_{210}$ (PEG-PS) synthesis: Poly(ethylene glycol) methyl ether was purchased from Rapp Polymers. Poly(ethylene glycol) (M_n: 2 kg/mol), bromoisobutyryl bromide (99%), trimethylamine (98%), styrene (98%) N,N,N′,N″,N″-pentamethyl-diethylenetriamine (PMDETA) (99%) and copper (I) bromide (CuBr, 99.99%) were purchased from Sigma-Aldrich. The materials used for the coacervates assembly are the same as stated in Chapter 2. Poly(allylamine hydrochloride) (PAH, M_W: 50,000), poly(styrene sulfonate) (PSS, M_W:~70,000), NaCl powder, 1,4-dioxane and tetrahydrofuran (THF), fluorescein isothiocyanate (FITC) and gold nanoparticles (200 nm) were purchased from Sigma-Aldrich.

Layer-by-layer assembly of polymersomes

Poly(ethylene glycol)$_{45}$-b-polystyrene$_{210}$ (PEG-PS) was synthesized by Dr. Jingxin Shao via atom transfer radical polymerization (ATRP), following a procedure previously reported by our group.[34] Bare PEG-PS polymersomes were assembled from this block polymer at a concentration of 2 mg/mL. Poly(allylamine hydrochloride) (PAH) and poly(styrene sulfonate) (PSS) solutions were prepared at a concentration of 1 mg/mL using 0.1 M NaCl. First, 1 mL PAH solution was added to the PEG-PS polymersome templates (ca. 2 mg/mL), and the mixture was shaken for 10 min at room temperature. Then, 0.1 M NaCl was used to wash the polymersomes and remove excess PAH before addition of 1 mL PSS solution. The mixture was shaken for another 10 min at room temperature, followed by centrifugation at 10,000 rpm for 5 min to remove all the supernatant after which the samples was washed with Milli-Q water three times.

Preparation of Janus Au polymersomes

In order to apply a gold coating, a droplet of the LBL polymersome solution (2 mg / ml) was dropped on a hydrophilic silica slide to form a monolayer of nanoparticles. After evaporation in air, a turbo sputter coater (Quorum Technologies, K575X) was used to coat one side of the polymeric particles with a thin gold layer (65 mV, 30 s). Ultrasound treatment was used to re-disperse the Janus polymeric particles into aqueous solution. The size and morphology of Janus Au nanomotors were characterized using dynamic light scatting, scanning electron microscopy and transmission electron microscopy.

Characterization of polymersomes

Zeta (ζ) potential measurements and DLS measurements were performed on a Malvern instrument Zetasizer (model Nano ZSP). Zetasizer software was used to process and analyse the data. SEM images of both polymersomes and Janus structures were obtained with a FEI Quanta 200 3D FEG. TEM images were recorded on a FEI Tecnai 20 (type Sphera) at 200 kV. Measurements were performed by dropping 10 µL samples in MilliQ onto a carbon-coated copper grid. After removing the excess solution by blotting paper, the samples were dried at ambient conditions. For staining, a drop of phosphotungstic acid (2 %) solution was placed on the grid for 30 s.

Encapsulation of Janus Au polymersomes in coacervates

The assembly of the coacervates was similar to that discussed in the previous chapters. To 200 µL of 0.5 mg/mL quaternized amylose (Q-Am) solution in an Eppendorf tube, a 100 µL 0.5 mg/mL carboxymethyl amylose (Cm-Am) solution was added to induce coacervation. 5 µL of 2 mg/mL Au polymersomes was

immediately added to the amylose mixture. The mixture was placed in an Eppendorf shaker (ThermoMixer) at 1500 rpm for 1 minute to allow the coacervate growth, followed by addition of 12 µL of 50 mg/mL terpolymer in PEG 350 to generate a polymeric membrane and stabilize the coacervate core. The final concentration of coacervate suspension was 0.32 mg/mL in Q-Am.

Determining sequestration efficiency of LBL polymersomes in coacervates

The sequestration efficiency was determined by analysing confocal images. The average fluorescence intensity of polymersomes (FITC in the lumen) was measured inside a number of coacervates, and compared to the same area outside the coacervates. As polymersomes were concentrated in the coacervates, the concentration difference between the inside and outside of the coacervates was corrected by a factor of 100. This value of 100 was obtained by measuring the volume of the coacervate-rich phase (~1 µL, obtained by centrifugation) compared to the total suspension volume (100 µL) of a coacervate sample formed in the same way. The sequestration efficiency was thus calculated as:

$$SE\% = \frac{Avg.\,Fluorescence\ inside}{Avg.\,Fluorescence\ inside + Avg.\,Fluorescence\ outside \times 100} \times 100$$

Motility test for hierarchical coacervate motors

Experimental chamber

A motility experimental chamber was made from two glass microscopy slides spaced by two pieces of autoclave tape. The autoclave tape was first attached to a larger glass slide on two ends, followed by the addition of sample in the middle, and capping by a smaller glass slide.

Optical recording

The red laser (660 nm, BeamQ) was placed on the left side of the microscope. Prior to recording, the red laser was turned on with a distance of 1 cm away from the experimental chamber. The red laser irradiated the coacervate sample for 3 min before the recording was started. The videos of coacervate motion were recorded using a bright-field camera (DFC7000T) on a confocal laser scanning microscope (Leica TCS SP8). A 63× water immersion objective was used for this recording.

The motility of coacervates was analysed using a tailor-made Python script,[35-36] where X and Y trajectory data were extracted and MSD was calculated. It is commonly calculated in 2D projection using the following equation:

$$MSD\ (t) = \langle (\vec{x}(t) - \vec{x}\ (0))^2 \rangle$$

where $\vec{x}(0)$ is the initial position of the coacervate, and $\vec{x}(t)$ is the position of the coacervate when time is *t*. One well-known solution is $MSD = 4D_{eff}\Delta t$, and the effective diffusion coefficient D_{eff} was obtained by fitting MSD curves with this equation (**Figure S5-3, S5-4**)

Supporting Information

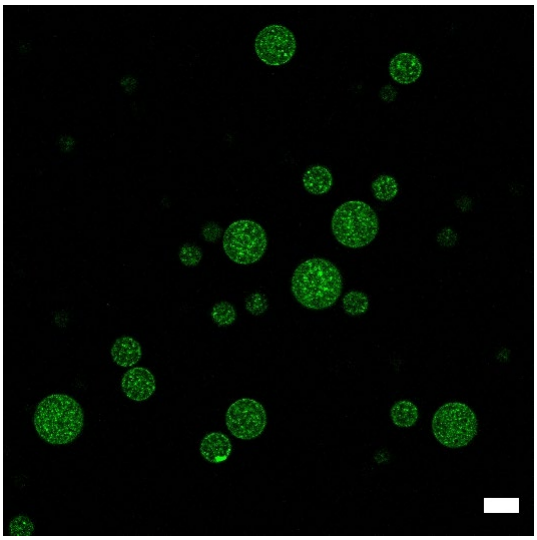

Figure S5-1 | Janus Au polymersomes encapsulated in the coacervate system. 5 µL 2 mg/mL Au polymersomes was added to 300 µL 0.32 mg/mL coacervate suspension. Scale bar represents 10 µm.

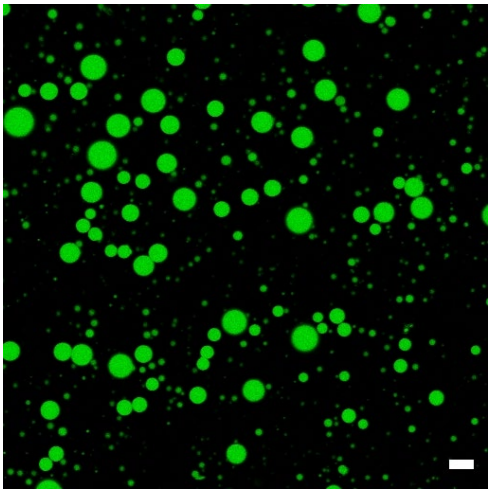

Figure S5-2 | Succinylated bovine serum albumin (BSA labelled with dye Atto 488) encapsulated in the coacervate system. 1.5 µL 1.2 mg/mL BSA was added to 300 µL 0.32 mg/mL coacervate suspension. Scale bar represents 15 µm.

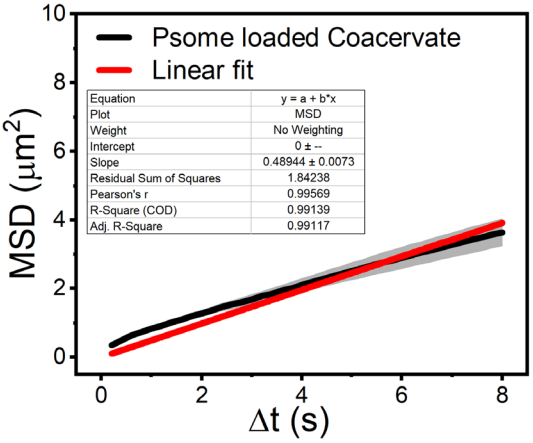

Figure S5-3 | MSD curve and linear fitting of coacervate motors loaded with symmetric PEG-PS polymersomes treated with laser irradiation.

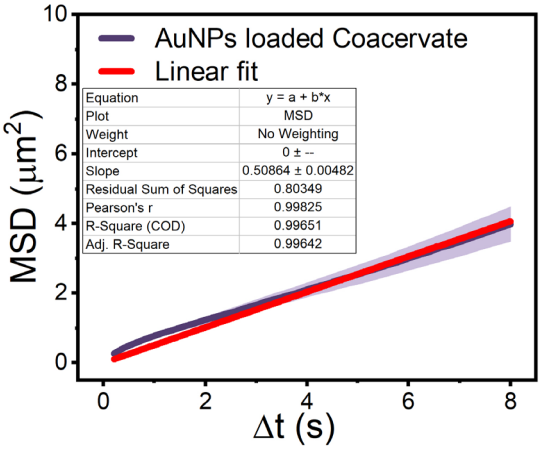

Figure S5-4 | MSD curve and linear fitting of coacervate motors loaded with AuNPs treated with laser irradiation.

Acknowledgements

Dr. Jingxin Shao is thanked for providing and analyzing polymersomes. She is also thanked for insightful discussions.

References

[1] Illien, P.; Golestanian, R.; Sen, A., 'Fuelled'motion: phoretic motility and collective behaviour of active colloids. *Chem. Soc. Rev.* **2017,** *46* (18), 5508-5518.

[2] Ren, L.; Wang, W.; Mallouk, T. E., Two Forces Are Better than One: Combining Chemical and Acoustic Propulsion for Enhanced Micromotor Functionality. *Acc. Chem. Res.* **2018,** *51* (9), 1948-1956.

[3] Vutukuri, H. R.; Lisicki, M.; Lauga, E.; Vermant, J., Light-switchable propulsion of active particles with reversible interactions. *Nat. Commun.* **2020,** *11* (1), 2628.

[4] Šípová-Jungová, H.; Andrén, D.; Jones, S.; Käll, M., Nanoscale Inorganic Motors Driven by Light: Principles, Realizations, and Opportunities. *Chem. Rev.* **2020,** *120* (1), 269-287.

[5] Xuan, M.; Wu, Z.; Shao, J.; Dai, L.; Si, T.; He, Q., Near Infrared Light-Powered Janus Mesoporous Silica Nanoparticle Motors. *J. Am. Chem. Soc.* **2016,** *138* (20), 6492-6497.

[6] Ahmed, D.; Sukhov, A.; Hauri, D.; Rodrigue, D.; Maranta, G.; Harting, J.; Nelson, B. J., Bioinspired acousto-magnetic microswarm robots with upstream motility. *Nature Machine Intelligence* **2021,** *3* (2), 116-124.

[7] Ahmed, D.; Baasch, T.; Blondel, N.; Läubli, N.; Dual, J.; Nelson, B. J., Neutrophil-inspired propulsion in a combined acoustic and magnetic field. *Nat. Commun.* **2017,** *8* (1), 770.

[8] Wang, W.; Duan, W.; Zhang, Z.; Sun, M.; Sen, A.; Mallouk, T. E., A tale of two forces: simultaneous chemical and acoustic propulsion of bimetallic micromotors. *Chem. Commun.* **2015,** *51* (6), 1020-3.

[9] Andrew, N.; Insall, R. H., Chemotaxis in shallow gradients is mediated independently of PtdIns 3-kinase by biased choices between random protrusions. *Nature Cell Biology* **2007,** *9* (2), 193-200.

[10] Eisenbach, M., Bacterial Chemotaxis. In *Encyclopedia of Life Sciences*, 2001.

[11] Fernández-Medina, M.; Ramos-Docampo, M. A.; Hovorka, O.; Salgueiriño, V.; Städler, B., Recent Advances in Nano- and Micromotors. *Adv. Funct. Mater.* **2020,** *n/a* (n/a), 1908283.

[12] Cao, S.; Shao, J.; Wu, H.; Song, S.; De Martino, M. T.; Pijpers, I. A. B.; Friedrich, H.; Abdelmohsen, L. K. E. A.; Williams, D. S.; van Hest, J. C. M., Photoactivated nanomotors via aggregation induced emission for enhanced phototherapy. *Nat. Commun.* **2021,** *12* (1), 2077.

[13] Shao, J.; Cao, S.; Williams, D. S.; Abdelmohsen, L. K. E. A.; van Hest, J. C. M., Photoactivated Polymersome Nanomotors: Traversing Biological Barriers. *Angew. Chem., Int. Ed.* **2020,** *59* (39), 16918-16925.

[14] Tierno, P.; Golestanian, R.; Pagonabarraga, I.; Sagués, F., Magnetically Actuated Colloidal Microswimmers. *The Journal of Physical Chemistry B* **2008,** *112* (51), 16525-16528.

[15] Lin, Z.; Si, T.; Wu, Z.; Gao, C.; Lin, X.; He, Q., Light-Activated Active Colloid Ribbons. *Angew. Chem., Int. Ed.* **2017,** *56* (43), 13517-13520.

[16] Chaturvedi, N.; Hong, Y.; Sen, A.; Velegol, D., Magnetic Enhancement of Phototaxing Catalytic Motors. *Langmuir* **2010,** *26* (9), 6308-6313.

[17] Ye, Z.; Sun, Y.; Zhang, H.; Song, B.; Dong, B., A phototactic micromotor based on platinum nanoparticle decorated carbon nitride. *Nanoscale* **2017,** *9* (46), 18516-18522.

[18] Dai, B.; Wang, J.; Xiong, Z.; Zhan, X.; Dai, W.; Li, C.-C.; Feng, S.-P.; Tang, J., Programmable artificial phototactic microswimmer. *Nat. Nanotechnol.* **2016,** *11* (12), 1087-1092.

[19] Palacci, J.; Sacanna, S.; Steinberg, A. P.; Pine, D. J.; Chaikin, P. M., Living Crystals of Light-Activated Colloidal Surfers. *Science* **2013,** *339* (6122), 936.

[20] Braibanti, M.; Vigolo, D.; Piazza, R., Does Thermophoretic Mobility Depend on Particle Size? *Phys. Rev. Lett.* **2008,** *100* (10), 108303.

[21] Jiang, H.-R.; Wada, H.; Yoshinaga, N.; Sano, M., Manipulation of Colloids by a Nonequilibrium Depletion Force in a Temperature Gradient. *Phys. Rev. Lett.* **2009,** *102* (20), 208301.

[22] Wang, W.; Wu, Z.; Lin, X.; Si, T.; He, Q., Gold-Nanoshell-Functionalized Polymer Nanoswimmer for Photomechanical Poration of Single-Cell Membrane. *J. Am. Chem. Soc.* **2019,** *141* (16), 6601-6608.

[23] Yu, N.; Lou, X.; Chen, K.; Yang, M., Phototaxis of active colloids by self-thermophoresis. *Soft Matter* **2019,** *15* (3), 408-414.

[24] Jiang, H.-R.; Yoshinaga, N.; Sano, M., Active Motion of a Janus Particle by Self-Thermophoresis in a Defocused Laser Beam. *Phys. Rev. Lett.* **2010,** *105* (26), 268302.

[25] Xuan, M.; Shao, J.; Gao, C.; Wang, W.; Dai, L.; He, Q., Self-Propelled Nanomotors for Thermomechanically Percolating Cell Membranes. *Angew. Chem., Int. Ed.* **2018,** *57* (38), 12463-12467.

[26] Zhang, D.; Sun, Y.; Li, M.; Zhang, H.; Song, B.; Dong, B., A phototactic liquid micromotor. *Journal of Materials Chemistry C* **2018,** *6* (45), 12234-12239.
[27] Lozano, C.; ten Hagen, B.; Löwen, H.; Bechinger, C., Phototaxis of synthetic microswimmers in optical landscapes. *Nat. Commun.* **2016,** *7* (1), 12828.
[28] Chen, Y.-L.; Yang, C.-X.; Jiang, H.-R., Electrically Enhanced Self-Thermophoresis of Laser-Heated Janus Particles under a Rotating Electric Field. *Scientific Reports* **2018,** *8* (1), 5945.
[29] Cao, S.; Wu, H.; Pijpers, I. A. B.; Shao, J.; Abdelmohsen, L. K. E. A.; Williams, D. S.; van Hest, J. C. M., Cucurbit-Like Polymersomes with Aggregation-Induced Emission Properties Show Enzyme-Mediated Motility. *ACS Nano* **2021,** *15* (11), 18270-18278.
[30] Pijpers, I. A. B.; Cao, S.; Llopis-Lorente, A.; Zhu, J.; Song, S.; Joosten, R. R. M.; Meng, F.; Friedrich, H.; Williams, D. S.; Sánchez, S.; van Hest, J. C. M.; Abdelmohsen, L. K. E. A., Hybrid Biodegradable Nanomotors through Compartmentalized Synthesis. *Nano Lett.* **2020,** *20* (6), 4472-4480.
[31] Yewdall, N. A.; Buddingh, B. C.; Altenburg, W. J.; Timmermans, S.; Vervoort, D. F. M.; Abdelmohsen, L.; Mason, A. F.; van Hest, J. C. M., Physicochemical Characterization of Polymer-Stabilized Coacervate Protocells. *ChemBioChem* **2019,** *20* (20), 2643-2652.
[32] Mason, A. F.; Yewdall, N. A.; Welzen, P. L.; Shao, J.; van Stevendaal, M.; van Hest, J. C.; Williams, D. S.; Abdelmohsen, L. K., Mimicking Cellular Compartmentalization in a Hierarchical Protocell through Spontaneous Spatial Organization. *ACS Cent. Sci.* **2019**.
[33] Golestanian, R., Anomalous diffusion of symmetric and asymmetric active colloids. *Phys. Rev. Lett.* **2009,** *102* (18), 188305.
[34] Che, H.; Zhu, J.; Song, S.; Mason, A. F.; Cao, S.; Pijpers, I. A.; Abdelmohsen, L. K.; van Hest, J. C., ATP - Mediated Transient Behavior of Stomatocyte Nanosystems. *Angew. Chem., Int. Ed.* **2019,** *58* (37), 13113-13118.
[35] Mestre, R.; Palacios, L. S.; Miguel-López, A.; Arqué, X.; Pagonabarraga, I.; Sánchez, S., Extraction of the propulsive speed of catalytic nano-and micro-motors under different motion dynamics. *arXiv preprint arXiv:2007.15316* **2020**.
[36] Mestre, R. Python-based Nano-micromotor Analysis Tool (NMAT) v.1. https://github.com/rafamestre/NMAT-nanomicromotor-analysis-tool.

CHAPTER 6

Epilogue

6.1 Introduction

Over the past decade, the construction of a fully autonomous artificial cell has been one of the most important outstanding challenges of science. As we have a fair understanding of biological processes that happen in cells, great progress has been made in the field of synthetic biology. Various life-like functionalities and biomimetic processes, ranging from *in vitro* transcription-translation to cell budding and division, have been incorporated into synthetic cells. Adaptivity, as a pivotal feature for the survival of living beings, has been explored and incorporated in protocell models only recently, such as imitating cellular motility and sensing the environment.

6.2 Concluding marks of this thesis

Until now, imitating cellular motility remains a very challenging task. In part, this is due to the lack of structural similarity between natural and synthetic systems, and the difficulty of integrating motion mechanisms in cell-mimetic systems. In addition to the remarkable individual dynamics of motile systems, it is worth exploring interactions between motors and their environments as natural cells live in a very dynamic and ever-changing environment. In the work presented in this thesis, we have investigated the complexity of motile behaviour exploiting a soft membrane-bound out-of-equilibrium compartment. In particular, we have explored a mechanism that takes advantage of ubiquitous and oftentimes troubling stochasticity (i.e., random fluctuations) to direct motile behavior. Furthermore, we have studied the complex interplay between such compartments' motility and their external environment.

Chapter 2 demonstrates the bottom-up engineering of motile coacervate-based synthetic cells that are equipped with a fluidic polymeric membrane and surface-attached laterally diffusive enzymes. This coacervate system is robust and able to change its properties while retaining its integrity. The lateral diffusion of enzymes, the key to self-propulsion, leads to dynamic asymmetry of enzyme distribution, which is applied to induce motility in presence of fuel. **Chapter 3** demonstrates an engineered motile system that is fully governed by stochasticity. When enzymes are confined to the fluidic polymer membrane of coacervates, they are distributed stochastically in time and space. This results in a transient, asymmetric configuration of propulsive units, which imparts motility to such coacervates in presence of fuel. Such motile process is described by a combined experimental and theoretical/simulation approach and key parameters that determine

stochastic behaviour are identified and utilized to modulate the motion output. Importantly, this is the first time that membrane dynamicity together with stochastic positioning of propulsive units is knowingly treated as a design element for a motility concept.

In most cases motile behaviour is regarded as a bulk property. Despite our understanding toward individual motion dynamics has improved much, we are still in the early stages of investigating the complex interplay between motile compartments and their dynamic environment. One aspect that has however rarely been taken into account is that in living systems motion is often restricted by the confined space in which the motile objects operate. While the confinement effect on inorganic motors has been studied theoretically, only a limited number of experimental studies have investigated such effect. A probable cause for the lack of experimental data is the difficulty of establishing a synthetic soft compartment whose motile behaviour can be effectively studied in a 3D confined space. **Chapter 4** reports the experimental realization of compartmentalized micromotors in the interior of 3D, semi-permeable giant unilamellar vesicles (GUVs), which enables us to systematically study their motile behaviour under confinement. The confined active particles are composed of coacervates, surface-decorated with enzyme motile units, as described in Chapters 2 and 3. Based on the results, we can conclude that a 3D confinement leads to restricted/diminished motion of motor systems. Furthermore, the confinement effect correlates with the compartment size and coacervate motor population density.

Chapter 5 further explores the dynamics of coacervates internally functionalized with another motor system, namely, self-propulsive Janus polymersomes. We wanted to investigate if and how an internalized smaller motor system can transfer its phoretic motion to a larger compartment through non-covalent interactions. In Chapter 5, nanoscale self-thermophoretic polymersomes are compartmentalized in our coacervates through electrostatic interactions to generate a hierarchical coacervate motor system, which can be activated using light. Interestingly, enhanced collective directional movement toward the side of laser irradiation is observed, which is opposite to the movement direction of the individual Janus polymersomes, demonstrating the complex interplay between motor systems and their environment.

6.3 Perspective and future challenges

It is clear from this thesis that mimicking one single function, i.e. motility, of living systems is a grand challenge itself, and the journey to explore it often encounters the need to utilize knowledge and technologies outside the field of synthetic biology. It is therefore important that we make a joint effort from different disciplines and from both experimentalists and theorists to achieve the ultimate goal – design of a fully autonomous artificial cell. Although a significant step forward has been taken in the field, some challenges remain in the pursuit of such synthetic cell. It has been proposed in the chemoton model that five hallmarks must be achieved in one single system to be considered as a living being, which are compartmentalization, information processing (e.g. DNA to store genetical information), growth and division, energy transduction (i.e., metabolism) and adaptivity (e.g. motility). Each individual hallmark has been reconstructed in a variety of artificial cell platforms; more importantly, a tandem of two criteria (such as compartmentalization and inter-communication) has also been fulfilled in several exemplary systems.

In regard to adaptivity, synthetic systems can not rival their natural counterparts in terms of complexity, ability to sense and respond to environmental cues and collective behaviours. Because of low Reynolds numbers at the microscale inertia does not exist and frictional force dominates, which leads to the situation that micromotors only move when force is exerted on them and stop immediately if such force disappears. Additionally, highly viscous and complex biological environments filled with ions, cofactors and biomacromolecules render it more difficult for sufficient motion capability. This requires synthetic systems to have a constant energy input and robust chemical pathways. Different propulsion mechanisms can also be explored to adjust the systems to deal with various environments. Temperature is another common environmental parameter that might influence micromotors, especially enzyme-powered systems. For example, high temperature tends to denature enzymes and leads to subunit dissociation. Compartmentalization is commonly used to accommodate and protect propulsive units, however, fuel accessibility and waste accumulation remain challenging due to poor permeability control and the lack of selective influx and efflux in most compartments. Thermal stability and integrity of the motile systems can also be obtained by enzyme immobilization or generation of a protective layer of temperature-responsive polymer around enzymes, which could effectively retain the conformation of enzymes. Furthermore, most motile systems move upon external addition of fuel and lack the

capability to store energy for a prolonged usage. A rudimentary form of metabolism (with six different enzymes) has been realized by our group, driving the motion of stomatocytes. A next step would be to design a biochemical pathway to store energy in another population of synthetic cells if it is difficult to incorporate energy storage and metabolism-driven motility in a single population of compartments. Such design would also advance developments regarding inter-system communication and sensing of environmental changes.

The complex dynamics of motile systems at their individual level, in combination with interactions with each other and their surroundings, will enable motile systems to display many surprising collective behaviours. For example, phoretic motors have shown dynamic clustering behaviour without any build-in attraction mechanism and complex pattern formation. Another important factor of living beings is the randomness and unpredictability of their behaviours. The debate over whether such randomness is simply noise or an active mechanism by living systems to evolve and develop has been going on for centuries. However, recent decades have witnessed more and more discoveries of living systems harnessing stochasticity to benefit themselves. For example, immune system is able to very quickly develop a new antibody in response to a new antigen by increasing the mutation rate of DNA related to immunoglobulins. Chemotaxis of many eukaryotic cells is considered as a type of directional random walk. It has been proposed that such stochasticity in their motions is beneficial in a dynamic and fluctuating environment to deal with complex and even conflicting signals, which can not be achieved by deterministic motion. This type of response to environmental signals can be considered as a raw form of intelligent decision-making, which is desirable in the design of smart responsive systems. Taken together, it is possible to build a smart synthetic motile system capable of sensing, memorizing, responding to signals, making a decision and altering their behaviours accordingly. An accurate description of their dynamics and environmental impact will provide an interesting platform to study fundamental processes and develop higher-order functionalities and such investigations will pave the way for further developments at the interface of active matter and synthetic biology.

Summary

Microscale engineering of active systems: exploiting dynamicity to induce motility

Biological systems, such as cells, are highly adaptive, governed by complex processes that permit their ability to function efficiently under fluctuating conditions. Scientists from various disciplines seek to replicate and imitate such complex processes to introduce life-like functionalities in manmade systems such as artificial cells. Various life-like functionalities and biomimetic processes, ranging from *in vitro* transcription-translation (IVTT) to cell budding and division, have been incorporated into synthetic cells. One highly interesting form of complex biomimetic behaviour is autonomous motion. Nevertheless, imitating cellular motility has been much less explored. In part, this is due to the lack of structural similarity between natural and synthetic systems, and the difficulty of integrating motion mechanisms in cell-mimetic systems. In this thesis, we are aiming at developing artificial platforms, able to embody biomimetic processes and mechanisms that can lead to autonomous motion. Our aim requires a synthetic cell platform, made of robust components with high degree of dynamicity, whilst being able to sense molecular fuel, and efficiently convert it into kinetic energy. This research and results thereof are described in five chapters.

Chapter 1 provides an overview of recent literature demonstrating developments toward mimicry of cellular motility utilizing soft compartments. In this regard, we discuss important biological features; namely, compartmentalization, biological reactions for energy production and, finally, motility of different types of biomimetic platforms.

The bottom-up construction and engineering of a synthetic cell based active system, which demonstrates dynamic behaviour that can lead to motion is the objective of the research performed in **Chapter 2**. Utilizing the polymer-stabilized coacervate system that was previously described by our group, we demonstrate control over size and (chemical) topology of such coacervate. The polymer membrane is endowed with chemical versatility, which allows surface modification with catalytic species to drive autonomous motion. We investigate the properties of the polymer membrane, and demonstrate that its fluidity and dynamicity can be regarded as an effective way toward biomimetic modulation of motion dynamics.

Random molecular fluctuations are inherent to all complex molecular systems. Nature has evolved mechanisms to control such random stochastic events to achieve the desired biological output. Inspired by this, **Chapter 3** presents the coacervate platform developed in Chapter 2 in a way that exploits stochastic processes and, in consequence, direct motile behaviour. We find that enzymes (i.e. catalase and urease), when confined to the fluidic polymer membrane of a core-shell coacervate, are distributed stochastically in time and space. This results in a transient, asymmetric configuration of propulsive units, which imparts motility to such coacervates in presence of the enzymes' substrates. This mechanism is confirmed by stochastic modelling and simulations in silico. Furthermore, we show that a deeper understanding of the mechanism of stochasticity can be utilized to modulate the motion output.

Motility is commonly studied as an individual functional element, while external parameters such as energy source are assessed mainly in bulk. Interaction between motors and their surroundings has important implications in the design of higher-order functionalities such as collective behaviour and inter-system communication. In real-life applications, confinement plays a crucial role in determining the type of motion active particles can adapt. **Chapter 4** demonstrates a tunable experimental platform to gain insight into the dynamics of active particles in environments with restricted 3D topology. Self-propulsive soft micromotors are examined inside a larger soft lipid vesicle where we observe anomalous diffusion upon confinement, leading to decreased motility, which is more pronounced in smaller lipid confinement. The results indicate that the theoretically predicted hydrodynamic effect dominates the motion mechanism within this platform.

Chapter 5 presents a hierarchical motile system where propulsive nanoscale swimmers act as powering engine of a microscale soft compartment. As motile units, self-thermophoretic and light-responsive Janus swimmers (polymersomes half-coated with a gold layer) recently reported by our group are employed. We encapsulate such Janus polymersomes inside coacervates to examine the transfer of phoretic motion from individual nanoswimmers to the coacervate they reside in. Surprisingly, such hierarchical motor system displays positive phototaxis (i.e., ability to move toward the light source), whereas the individual nanomotors move away from the source of light. A photothermal effect is systematically ruled out as the reason for driving the motion of the coacervates, confirming that the anisotropy of the photothermal gradient is key to such motion dynamics.

This thesis provides various approaches to the physiochemical construction and engineering of active motile systems, and demonstrates motile output controlled by stochastic processes for the first time. Finally, **Chapter 6** summarizes the main findings of this thesis and looks forward to further developments.

Curriculum Vitae

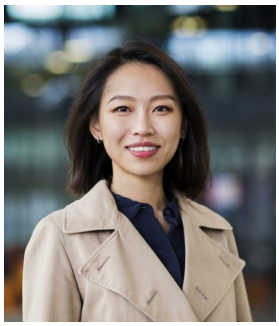

Shidong Song was born on February 1993 in Changchun, Jilin Province, China. After finishing her high school education in Jilin Provincial Experimental School, she started her undergraduate education at Xiamen university, China in 2011. In her bachelor graduation project, she developed an economical substrate used for surface-enhanced Raman spectroscopy (SERS), which could collect and detect residual pesticide fast and easy in the group of Prof. Chen Xi (陈曦). During her undergraduate education, she also completed two research internships to investigate food safety using GC-MS and performance of advanced formic acid fuel cells, respectively. After receiving her Bachelor's degree in Chemistry in 2015, Shidong started her new journey in Eindhoven University of Technology (TU/e) as a master student. During her master project, she worked on self-assembly and characterization of sequence-controlled polyurethane under supervision of Prof. Ilja Voets, which gave her a background of physical and colloidal chemistry. As part of her master's programme, she finished a 5-month internship on synthesis and modification of lysine mediated silica nanoparticles for anti-reflective and anti-fouling coating (for solar cell panels) in DSM, The Netherlands. As of November 2017, she started in van Hest group as a PhD student in TU/e. Her doctoral research focused on the construction and engineering of active motile systems, and the most important results are presented in this thesis.

List of publications

1. **Song, S.**; Llopis-Lorente, A.; Mason, A. F.; Abdelmohsen, L. K. E. A.; van Hest, J. C. M., Confined Motion: Motility of Active Microparticles in Cell-Sized Lipid Vesicles. Manuscript submitted.
2. **Song, S.**; Mason, A. F.; Post, R. A. J.; De Corato, M.; Mestre, R.; Yewdall, N. A.; Cao, S.; van der Hofstad, R. W.; Sanchez, S.; Abdelmohsen, L. K. E. A.; van Hest, J. C. M., Engineering transient dynamics of artificial cells by stochastic distribution of enzymes. *Nat. Commun.* **2021,** *12* (1), 6897.
3. Mason, A. F.; Altenburg, W. J.; **Song, S.**; van Stevendaal, M.; van Hest, J. C. M., Chapter Three - Terpolymer-stabilized complex coacervates: A robust and versatile synthetic cell platform. In *Methods in Enzymology*, Keating, C. D., Ed. Academic Press: **2021**; Vol. 646, pp 51-82.
4. Cao, S.; Shao, J.; Wu, H.; **Song, S.**; De Martino, M. T.; Pijpers, I. A. B.; Friedrich, H.; Abdelmohsen, L. K. E. A.; Williams, D. S.; van Hest, J. C. M., Photoactivated nanomotors via aggregation induced emission for enhanced phototherapy. *Nat. Commun.* **2021,** *12* (1), 2077.
5. Wang, L.*; **Song, S.***; van Hest, J.; Abdelmohsen, L. K. E. A.; Huang, X.; Sánchez, S., Biomimicry of Cellular Motility and Communication Based on Synthetic Soft-Architectures. *Small* **2020,** *16* (27), 1907680. (Equal contribution)
6. Pijpers, I. A. B.; Cao, S.; Llopis-Lorente, A.; Zhu, J.; **Song, S.**; Joosten, R. R. M.; Meng, F.; Friedrich, H.; Williams, D. S.; Sánchez, S.; van Hest, J. C. M.; Abdelmohsen, L. K. E. A., Hybrid Biodegradable Nanomotors through Compartmentalized Synthesis. *Nano Lett.* **2020,** *20* (6), 4472-4480.
7. Che, H.; Zhu, J.; **Song, S.**; Mason, A. F.; Cao, S.; Pijpers, I. A.; Abdelmohsen, L. K.; van Hest, J. C., ATP-Mediated Transient Behavior of Stomatocyte Nanosystems. *Angew. Chem., Int. Ed.* **2019,** *58* (37), 13113-13118.
8. González García, Á.; Timmers, E. M.; Romijn, N.; **Song, S.**; Sahebali, S.; Tuinier, R.; Voets, I. K., Micellization of a weakly charged surfactant in aqueous salt solution: Self-consistent field theory and experiments. *Colloids and Surfaces A: Physicochemical and Engineering Aspects* **2019,** *561*, 201-208.

Acknowledgements

Four years of PhD have flown by even more quickly than I feel. The completion of this thesis is only possible with support from so many people. I want to express my gratitude to these wonderful colleagues, friends and family in this last part.

To my first promotor Jan, you're absolutely remarkable, and I am always in awe of your wisdom. You're an amazing supervisor, I feel enlightened every time I had a meeting with you. You always notice what your students are capable of even when themselves don't realize. You keep the whole group prosperous by seeing our potentials and guiding us towards the right direction. You always give the right amount of freedom, guidance and support, shaping me into this independent researcher with critical thinking. Your dedication to science and style of leadership will inspire me my whole life.

To my co-promotor Loai, the first time I met you was my application interview to the group. I just finished my application presentation and was really nervous about how it had gone. The interview/lunch with you (and Alex) put me at ease as you're so friendly and down-to-earth. Thank you for being a cheerleader type of mentor, always encouraging me. You taught me some skills that will potentially benefit my whole career, number one is writing. I remember when I wrote my first review together with Lei, time was really tight, and you gave me tremendous help and guidance, and that was my light bulb moment for scientific writing. You're also a mentor close to your students, parties after conferences, group outings, drinks on Fridays and chats about our favourite whiskey were really nice memories that I will keep in mind in the future.

Next, I'd like to thank Samuel. My short stay in your group in IBEC was crucial for this thesis. I learnt a lot about motors in the summer of 2019. And I also learnt a lot from you. As a scientist, you're absolutely inspiring, and as a mentor, you give critical comments and ask thought-provoking questions which I greatly benefited from for our collaborative article and review. You also have a fun side – during our group outing to IBEC in 2019, you showed your excellent skill at go-karting, and you also enjoyed partying with us. It's great to know you and learn from you during my PhD.

Bert and Tom, being in the same MST group with you is very educational – I learnt a lot from your lectures, talks and questions to other people. I am very grateful that you're part of my PhD. And thank you for agreeing to be on my committee.

Then I'd like to thank the external members of my committee. Daniela, your talks (at CHAINS and other conferences) were always so great and instructive and thank you for

your insightful feedback! Janne-Mieke, thank you very much for being on my committee and evaluating my thesis.

Rint, I first know you from the course physical organic chemistry. It was a really tough one, but your patience and knowledge help me pass it. Thank you for chairing my defense!

Among others, my collaborators contribute greatly to the completion of this thesis. During the summer stay in IBEC in 2019, I spent a lot of time together with wonderful officemates and lab mates in Samuel's group. Rafa, Xavi and Ana, thanks for being such nice office mates. Rafa, you're smart and patient, and taught me how to use these complicated softwares from 101. I wish you a happy stay in Southampton. Xavi and Ana, thanks for the coffee breaks and chats and enduring my endless questions about motors and Barcelona. Lei, you were the only Chinese in the group, and we had an immediate connection. It was great that we collaborated on the review and wish you all the best in Harbin. Hope you could have a sabbatical in the Netherlands after covid. Tania, the period I stayed was not exactly the time you were in the group, but people definitely adore you and mention you a lot, so great that now you are in the van Hest group! Thanks to Paul, Maria, Joaquim and everyone in the group, I had a wonderful time there.

And to Remco, Richard and Marco, without you the two most important chapters in my thesis would not be possible. Remco and Richard, you're so smart and bright, and able to explain very advanced math concepts in a way that's easy for layman as me to understand. Richard, it's really nice to know you and have you as co-author, we had countless meetings together and so happy it turned out great. Marco, you're an amazing physicist, and you answered me so many motor questions that had puzzled me a lot. Hope you and your family all the best in Zaragoza!

A special thank you goes to people who support. Marjo, thank you so much for taking care of administration, you're a great secretary and full of energy. Wish you a joyful retirement! Joost, Ralf, Jolanda and Peggy (biolab mother!), thank you very much for all the help and support! Lou, 楼长，你是全楼中国人的主心骨！Yan, thank you for all your knowledge on FPLC.

The four years I spent in van Hest group was full of joyful and unforgettable moments. My paranymph, Jingxin, you're a great friend and collaborator and like a big sister to me. 我一开始来组里经常慌里慌张跑到你办公室求助，你一直很耐心地帮我指导我，现在我毕业了，又有新的小崽子们找你求助了！你是个贴心又好笑的人(你的好笑都不是故意的我怀疑你有时候自己都没意识到)，跟你聊天说话讲什么都很开心！Jingxin, you're excellent at teaching and helping

new students, without you, many of us would have panicked in the first year. You're also an amazing researcher and ready to help out, my collaboration with you was fantastic.

To the Chinese gang in the group, Hailong, Jianzhi, Shoupeng, 你们都比我更早入组，面试的时候看到你们我就放心多了！你们都帮助了我很多，我也跟你们学了很多。海龙祝你在学校一切顺利，文章发发发学生顺心！守鹏祝你在德国万事如意，顺利找到理想的教职，咱们有空再聚！建志，你超搞笑的又爱说大实话，我最爱听你聊八卦的。祝你在国内事业节节高，欢朋满座！Bingbing, 活泼的冰冰，还记得你刚来组里说自己还没男朋友，到现在已经结婚，时间过得好快！祝你一切顺利天天开心！Yuechi, 月池你身上非常有一个东北妹子的特质，可爱又直率。以及和你同时来组里的建洪 (Jianhong)和昱东 (Yudong), 你们都很能干，而且现在都已经是学长学姐啦，祝你们博士期间一切顺利。Hanglong，杭隆你是最棒的 TEM 专家，咱老板都折服在你的石榴裤下了。祝你在 MIT 事事顺利！最新来组里的淑坤和英桐，祝你们在组里顺心顺意！

A big thanks to the members of coacervate cluster: Alex Mason, Amy, Bastiaan, Wiggert, Marleen, Sebastian, Thijs, Alex Cook. Alex, Amy, Bastiaan, Wiggert and Marleen, it was great to share loads of conference party memories and fun drunk moments with you guys. Alex, we know each other from day 1, and I learnt all about coacervate, a lot of polymer synthesis and NMR skills from you from the beginning of my PhD. You're always ready to help out with your not-so-easy-to-understand Aussie accent. Wish you and your family all the best in Australia! Amy, you have such a bubbly and bright personality and it's always so nice to talk to you. You're an expert in protein engineering and I wouldn't be able to produce these modified proteins without your help and knowledge! Let's keep in touch and go top rope! Bastiaan, you have a broad knowledge on artificial cells, and I am amazed by your good ideas every time I discussed some papers with you. Wish you and you girl friend all the best in Paris! Wiggert and Marleen, we joined the group around the same time and all studied coacervates. It was wonderful to have you two from the beginning, as we experienced these similar struggles together, and now, our projects all turned out great. Wish you guys a smooth and pain-free writing! Marleen, it was so nice to organize the group outing together with you. It was a lot of work I have to say, but it was a perfect one. We made such a great team! Sebastian, you're the second chemist (after Alex) in charge of terpolymer, and thank you a lot for your excellent polymer expertise! Hope you can enjoy Oktoberfest this year!

Toni, I wanted to collaborate with you since you joined the group, and it's great that it happened! The outcome is great and let's hope for the best. I am really happy for you that

you got a position that you deserve back in Spain, and I wish you all the best! There are many more to thank, Chiara (always looking for snacks after loooong experiments!), Suzanne (so nice we're finishing together, go green and enjoy pilates!), Jan Pille (thanks for answering my stupid column questions), Ilia (I enjoyed the unicorn card and superheroes!), Teresa (dance & party!), Annelise (you're vibrant!), Roy (nice joint birthday cakes on third floor coffee corner!), Gilad, Pascal and Imke (the most funny couple), Yigit (you and your wife are absolutely adorable!), Duc, Fusi (PR expert), Wouters, Eduardo, Luciano (you will do great at your job!).

I spent a large portion of these 4 years in my office, and I'd like to thank my wonderful office mates for such fun and warm environment. Rens, you're the tech savvy person in the office who always save our asses. And your Friday music show was contagious, and I miss our office festival, our plank challenge and your huge green plant a lot! Daan, it's so nice to have you as my office mate. I enjoyed all our chats. You're a good dancer and wish you happy and healthy! Daan & Rens, the sand ball throwing game was really fun, and I will keep my notes that are filled with ~~dirty~~ Dutch slangs and might use them to surprise my future officemates. Daan I hope you can remember the Chinese sentence that made Danjing blush so much! Peggy, our soprano, you're always the one who told me that the Dutch slang Rens/Daan/Wiggert taught me was way too rude to use. Thank you for keeping me from being beaten up on the street! Enjoy your newly decorated house and more holidays (free time without kids)! Special thanks to Rens and Daan and Peggy for lending me your office keys in the first half of my PhD. Harm, our newest member in the office, hope you will enjoy this office as I do and all the best!

Microscopy is an important part of my project, and I spent lots of days and nights in the Ceres lab. First, thanks to Alex Mason, Bastiaan and Wiggert for helping me get familiar with confocal and for great discussions and microscope tricks. Alex J and Shuo, we shared confocal a lot and you're absolutely hard working. Thanks for all the chats and help next to confocal. Ardjan, your microfluidic device was just next to confocal. It was nice to chat with you and learn something about bikes. Patrick, thanks for taking care of confocal and it's a little troublemaker! Natalie and Laura, thanks for teaching me how to use STORM. It's a really cool instrument and you girls know everything about it.

MST third floor has an absolutely great vibe, thanks to all the people from groups of Luc, Maarten, Tom, Patricia and Willem: Ni Yan, Simone, Lenne, Maaike, Eline, Eva, Glenn, Danjing, Johnick, Boris, Robby, Guido, Ewelina, Roy, David, Bente, Emira, Eva, Peter, Iris, Pim, Bas and more.

To my friends on fourth floor and outside of MST, you make my PhD journey full of joys. First, to SHEAP group, Elisabeth, Annelore and Patri, I cherish your friendship and the fourth floor without you will feel very different. Elisabeth, you're smart and strong and I enjoy a lot our dinners and long chats. I am looking forward to visiting you in Germany. Annelore, you're so considerate and kind and colourful, and hope to visit your rabbits and alpaca (hopefully!) in your new house! Patri, you're so sweet and lively. You will do great at your career, and you deserve it! Ghislaine, you're always so nice and energetic, I like our chats on all sort of random topics. Muhabbat and Souma, you guys are adorable and absolutely obsessed with chemistry. It was really great to occasionally join your office coffee breaks and talk about all the fun stuff, also with Diederik. Souma, would be great if you learn how to tell a diamond from a chemist point of view in the future! Jie, you're a sweet boy and wish you all the best! There are many more to thank who make me happy: Jingyi, Yunfei, Linlin, Marco, Gilles, Eveline, Davey…Wish you all the best and happiness!

To my old friends, Emma, Dylan, Hande (and Eric and Pamuk) and Sheen, you have my heart! Emma and Hande, you're my support system and my family, I miss you so much!! I am so grateful that I picked the right master project and know you girls. Now I only hope covid will pass really quick and I can visit you and Dylan soon! Dylan, mate, I just want to have some beers or whiskey with you again. Sheen, you're the fun mentor everyone wants to have, and I learnt so much from you, you're inspiring & so kind and I am really looking forward to our meet-up!!

我的中国朋友们：嘟嘟我很想念你以及我们的度假，祝我们以后有钱有闲天天假期。鹭烟我们从大学认识到现在竟然也有十年了！感谢你的陪伴期待我们下次见面！李博，我硕果仅存的中学朋友，希望我能快点回国放假和你吃吃喝喝。发财团：七老师，小羊，六六六，从六年前你们就是我在这边最亲近的朋友了，对你们熟悉到像兄弟姐妹了，给你们么么哒。老李老叶，很开心通过 monk 认识你们！喜欢你们！还有可爱的安小琪老隋，希望和你们在未来一起开开心心去野攀。麻爽大哥和大兄弟，感谢你们的友谊，祝你们事业生活一切顺利！云吞阔少风筝，喜欢每次和你们的聚会，期待下一次见面，祝你们开心顺利！迟梦大芳，你们是可爱的小伙伴！咱们经常聚！希望咱们下次别喝到见酒想吐。Lily，喜欢每次和你一起过年过节大吃大喝，以后每年都安排上！马鹿山和推迪，可爱的网友们，每次看到你们的群聊就觉得很开心很好玩儿。莲姐感谢你的红包们嘻嘻，写论文的好吃好喝全靠这个了！祝你身体健康发发发！

阿灰(hui), 你做我傧相这件事其实蛮有趣的! You're amazingly witty, intelligent and funny! Thank you for being who you are and being the most important people in my life. I am grateful to have you with me on this journey, and I hope we continue our journey together forever.

我的家人们，我走到现在全靠你们从小对我的爱和培养。爷爷奶奶，姥姥姥爷，我从小就是跟在你们身边长大的，你们对我有非常重要的影响。因为疫情好几年没见你们了，很想念，祝你们无论在哪里，一切都好！也感谢大爷老姑，二姨大舅，还有一起长大，小时候一起疯玩的张韵魏雨初宋凡穷，以及小不点琦琦，祝你们一切顺心如意，平安开心！最后我的老爸老妈，没有你们的爱和支持，就没有今天的我。感谢你们一直以来坚信我是个聪明的小孩！希望和你们一起游遍欧洲，我爱你们！